Coherent spectroscopy of InGaAs quantum dots

vorgelegt von

Master of Science
Stefan Maximilian Strauß
geb. in Minden

von der Fakultät II-Mathematik und Naturwissenschaften
der Technischen Universität Berlin
zur Erlangung des akademischen Grades
Doktor der Naturwissenschaften
Dr. rer. nat.

genehmigte Dissertation

Promotionsausschuss:

Vorsitzende: Prof. Dr. Kathy Lüdge

Gutachter: Prof. Dr. Stephan Reitzenstein

Gutachter: Prof. Dr. Mete Atatüre

Tag der wissenschaftlichen Aussprache: 29. Juni 2018

Berlin 2018

Kurzdarstellung

Exzitonen in Halbleiterquantenpunkten stellen außergewöhnlich gute Zweiniveausysteme mit einem großen optischen Übergangsdipolmoment dar. Obgleich ihr Hauptpotential sicherlich in der Funktion als Einzelphotonenquelle zu sehen ist, werden sie insbesondere wegen ihres großen optischen Übergangdipolmoments auch zunehmend interessant für die experimentelle Grundlagenforschung. Die vorliegende Arbeit präsentiert Studien, die mittels kohärenter Spektroskopiemethoden grundlegende Phänomene in Quantenpunkten erforschen.

Im ersten Ergebnisteil werden zunächst die optischen Eigenschaften von vorpositionierten Quantenpunkten untersucht, die mittels vergrabener Stressoren gewachsen wurden. Abgeschlossen wird dieser Teil durch resonante Photostromspektroskopie an Quantenpunkten, die in elektrisch kontaktierten Mikrosäulenresonatoren eingebettet sind.

Der zweite Teil beginnt mit der Untersuchung der durch einen einzelnen Quantenpunkt induzierten Wigner- Zeitverzögerung, und wir zeigen, dass diese länger ist als seine Dekohärenzzeit T_2, welche das theoretische Limit für den kohärent gestreuten Anteil darstellt. Anschließend zeigen wir, dass die Photonenstatistik des anregenden Lichtfelds maßgeblich die Antwort eines resonant getriebenen Zweiniveausystems, in unserem Fall ein Exziton in einem Halbleiterquantenpunkt, bestimmt. Augenfällig ist ist hierbei zum Beispiel, dass das Mollow-Triplett, welches wir unter kohärenter Anregung beobachten, unter thermischer Anregung verschwindet.

Der dritte Teil widmet sich dann der Erforschung der resonant getriebenen Biexzitonenkaskade mittels Zweiphotonenanregung. Durch die kohärente Wechselwirkung zwischen Lichtfeld und Exzitonen ergibt sich ein komplexes Fünfniveausystem. Erstmals zeigen wir hier optische Zweiphotonen-Rabioszillationen in der Zeitdomäne. Darüber hinaus untersuchen wir die Korrelationen zwischen den unterschiedlichen Übergängen und zeigen, dass man die Zeitordnung der emittierten Photonen zum Beispiel durch die Leistung des eingestrahlten Lasers manipulieren kann.

All diesen Untersuchungen gemeinsam ist die resonante Anregung, die eine kohärente Manipulation der Quantenpunktzustände ermöglicht und somit typische Phänomene der Resonanzfluoreszenz wie Rabioszillationen und das Mollow-Triplett zugänglich macht. Des Weiteren stellen namentlich die Untersuchungen zur Photonenstatistikanregungsspektroskopie und die Versuche an der bekleideten Biexzitonenkaskade unter Beweis, dass grundlegende Effekte der Quantenoptik mit Hilfe von Quantenpunkten in einem skalierbaren und anwendungsnahen Umfeld erforscht werden können.

Abstract

Excitons in quantum dots represent a remarkably good two-level system with a large optical dipole transition moment. Although most research currently focuses on enhancing their already outstanding properties as single photon emitters they become also increasingly interesting for experimental fundamental research due to their large dipole transition moment. This thesis presents studies which explore fundamental phenomena in quantum dots using coherent spectrocopy methods.

First, we will first examine the optical properties of site-controlled quantum dots which were grown using a buried stressor via resonance fluorescence. Subsequently, we will show results that were obtained using photocurrent spectroscopy to study single quantum dots that are embedded in micropillar resonators.

This is followed by a study of the Wigner time delay induced by a single quantum dot and which shows that the maximum delay is larger than its dephasing time T_2 which is the theoretical limit for coherently scattered fraction. The next section demonstrates that the response of a resonantly driven two-level system which in our case is represented by an exciton in a seminconductor quantum dot depends significantly on the photon statistics of the exciting light field. Most strikingly, the Mollow triplet which we observe under coherent excitation vanishes under thermal excitation.

The second part presents results concerned with the resonantly driven biexciton cascade via two-photon excitation. The coherent interaction between light field and excitons gives rise to a complex five-level system. Here, we show for the first time two-photon Rabi oscillations in the temporal domain. Furthermore, we examine the correlations between the different transitions. The measurements show that we can manipulate the time-ordering of the emitted photons by changing for example the laser power.

All these studies share the resonant excitation scheme which allows for a coherent manipulation of the states of the quantum dot and grants access to phenomena typical for resonance fluorescence such as the Mollow triplet and Rabi oscillations. In particular the experiments on photon excitation spectroscopy and the studies on the dressed biexciton cascade show that fundamental effects of quantum optics can be explored in a scalable and application oriented setting using quantum dots.

Contents

1 Introduction 1

2 Theoretical aspects 5
- 2.1 Quantisation of the electromagnetic field 5
- 2.2 Photon correlations and higher order coherence 7
- 2.3 Light fields 8
- 2.4 Two-level systems 11
- 2.5 Three-level systems 19
- 2.6 Solid-state quantum emitters 23

3 Experimental techniques 27
- 3.1 Optical microscopy 27
- 3.2 Light sources 31
- 3.3 Detection of light 32
- 3.4 Sample fabrication 34

4 Resonant spectroscopy of site-controlled quantum dots & photocurrent spectroscopy 37
- 4.1 Resonance fluorescence from site-controlled quantum dots 37
- 4.2 Photocurrent spectroscopy of quantum dot micropillars 47
- 4.3 Summary of chapter 4 53

5 Wigner time delay & photon-statistics excitation spectroscopy 55
- 5.1 Wigner time delay induced by a single quantum dot 55
- 5.2 Exciting a quantum dot with thermal light 60
- 5.3 Summary of chapter 5 70

6 Coherent excitation of the biexciton: a cascaded cascade 73
- 6.1 Characterisation of the biexciton cascade 74
- 6.2 The two-photon dressed cascade 76
- 6.3 Summary of chapter 6 90

7 Conclusion & outlook 93

Bibliography 95

Appendix 109
- 1 Numerical simulations of the correlation functions in the dressed cascade 109
- 2 Sample structures 111

List of abbreviations

AFM	atomic force microscope
APD	avalanche photo diode
CCD	charge coupled device
CPT	coherent population trapping
cQED	cavity quantum electrodynamics
EIT	electromagnetically induced transparency
EOM	electro-optic modulator
FPI	Fabry-Perot interferometer
FSS	finestructure splitting
FWHM	full width at half maximum
HBT	Hanbury-Brown and Twiss
IRF	instrument response function
LA phonons	longitudinal acoustic phonons
MBE	molecular beam epitaxy
MOVPE	metalorganic chemical vapour phase epitaxy
NA	numerical aperture
PBS	polarising beam splitter
PL	photoluminescence
pm	polarisation maintaining
PS	photocurrent spectroscopy
QD	quantum dot
QKD	quantum key distribution
QTS	quasi-thermal light source
RF	resonance fluorescence
SCQD	site-controlled quantum dot
SEM	scanning electron microscope
SI	système international

SIL	solid immersion lens
SK	Stranski-Krastanow
SPCM	single-photon counting module
SPDC	spontaneous parametric down conversion
SQUID	superconducting quantum interference device
SSPD	superconducting single-photon detector
TCSPC	time-correlated single photon counting
TES	transition edge sensor
TLS	two-level system
ULCA	ultrastable low-noise current amplifier

A photon is what a photodetector detects.

Roy Glauber

1 Introduction

Since the beginning of its formulation almost a century ago, quantum physics and the ensuing technologies have transformed not only science itself but many aspects of the human existence in such fundamental ways that its influence can hardly be overestimated. Most of these technologies and devices such as laser systems, transistors and other semiconductor devices of this nowadays called first quantum revolution are now so ubiquitous that most scientists won't even consider them to be "quantum". Their working and design relies however crucially on quantum mechanics and would have been inconceivable to a physicist just a hundred years ago.

Continuous improvement of these 1.0 quantum devices has led to such spectacular advances in solid-state, optical and atomic physics that scientists around the world are now routinely able to create, manipulate and read-out single (or very few) particle states of light and matter. This is termed the second quantum revolution. This revolution is well under way and the experimental techniques have even already reached such a degree of maturity that quantum computers able to perform simple quantum algorithms were made available to the public [1]. The ground breaking success of the first quantum revolution has fueled hopes that its successor might be just as successful. This has lead many governments around the world to initiate major research programs [1] reflecting modern societies belief in science as the source of all salvation.

Epitaxially grown self- assembled semiconductor quantum dots (QDs) are a good example of the aforementioned development. Ever increasing mastery in the growth and processing techniques of semiconductors led to their discovery in 1985 [2] and continues to improve their odds in playing a role in the second quantum revolution. Excitons in QDs represent a remarkably good two-level system (TLS) with a large optical dipole transition moment. Such two-level system are capable of emitting single, indistinguishable photons on demand which are the indispensable building blocks for many schemes in quantum communication or photonic quantum computing.

So far, most experiments requiring highly indistinguishable single photons rely on a spontaneous parametric down conversion (SPDC) process. However, as this technology reaches its physical limits, QDs are likely to surpass them in the near future. This evolution in the field of quantum optics using quantum dots was largely rendered possible by the development of resonance fluorescence techniques. These techniques allow one to coherently generate and control excitons in QDs giving access to a

[1] In 2016, IBM launched the IBM Quantum Experience, a web page where anyone could fiddle around with their 5 qubit quantum computer. Since November 2017 a 20 qubit processor is also available to the interested user.

wealth of quantum optical phenomena. In principle, QDs are also more than viable candidates for the generation of entangled photon pairs where the lead of SPDC on QDs is however still considerably larger.

This thesis aims to show that while QDs are poised to become the single-photon emitter par excellence they are also increasingly attractive for fundamental research on coherently driven two- and multi-level systems.

In **chapter 2** we outline the basic theoretical underpinning for the experiments conducted during this thesis. First, we quickly recap the quantisation of the free electromagnetic field and then discuss its consequences especially in terms of photon statistics and correlation functions. We then treat the theory of two- and multi-level systems with a focus on resonance fluorescence before we discuss semiconductor QDs which are the central subject of this thesis.

Chapter 3 introduces the setup that was built to perform the resonance fluorescence and photocurrent experiments. Furthermore, the experimental methods and devices which were used during experiments are presented.

Equipped with the knowledge from these two chapters we can then proceed to present results obtained during my PhD studies at the Technische Universität Berlin. In **chapter 4** we will discuss experiments conducted with excitons in QDs, i.e. single two-level systems. First, we will show that QDs grown at predefined positions, so called site-controlled QDs, can be used for resonance fluorescence experiments and show promise for applications as single-photon emitters. The final section of the chapter is devoted to photocurrent spectroscopy which represents an alternative to resonance fluorescence to study coherent light-matter interaction in QDs.

In **Chapter 5** we present studies that explore phenomena that are a little more general to the physics of a two-level system interacting with a resonant light field. In the first section, we measure the Wigner time delay induced by a single quantum dot. We show that due to pure dephasing the measured time delay exceeds the decoherence time of the QD which is the theoretically achievable time delay for the coherently scattered photons in our system. The second and larger part of the chapter explores the response of a TLS to thermal photon statistics. Confirming theoretical predictions, our experiments show that a TLS can act as a sensitive probe to the fluctuations present in a light field.

Chapter 6 explores coherent light-matter interaction in the biexciton cascade. Conservation of angular momentum requires a two-photon excitation process to coherently drive the cascade. We evidence the coherent interaction in the temporal domain by observing two-photon Rabi oscillations as a function of time. In the spectral domain the coherent interaction leads to the emergence of a dressed cascade. By performing correlation experiments, we show that depending on the selection of the spectral window the photon pair emission in this dressed cascade can be either time-ordered or -unordered.

State of the art in quantum optics with quantum dots

Since the first demonstration of single-photon emission from a single QD in 2000 [3, 4], the fabrication and spectroscopy of QD devices has greatly advanced and diversified. Widely different aspects and phenomena have been studied in QD devices ranging from thermometry, spin-photon entanglement to injection locking in QD micropillar lasers [5–7]. Currently they certainly hold greatest promise as single-photon emitters. Their outstanding properties as single-photon emitters have also recently been used for boson sampling experiments with unprecedented sampling rates [8–10]. Single-photon purity, indistinguishability and brightness are all approaching values which render them in principle practical

candidates for quantum key distribution (QKD) schemes [11–14]. For mere short range communication, however, decoy-state protocols working with attenuated laser pulses offer hard-to-beat scalability and low costs.

Another possible future avenue is the creation of entangled photon pairs on-demand from the biexciton cascade [15, 16] for long range quantum networks based on the quantum repeater concept. Here, the experimental and technological requirements are even more challenging. In addition to the aforementioned criteria for single-photon emission, the two excitonic states need to be degenerate, which is usually the case for around for only 0.1 % of all QDs[2]. Triggered generation of polarisation-entangled photon pairs from the biexciton cascade has been demonstrated several times [16, 19–21] but entanglement swapping which is a central ingredient of the quantum repeater scheme has remained elusive so far. Additionally, it is widely acknowledged nowadays that most probably not one single kind of platform is capable of fulfilling the widely different requirements of a quantum repeater network. Thus hybrid systems consisting e.g. of QDs as photon sources and atomic clouds as quantum memory are currently explored [22–24].

Regarding experimental verification of fundamental quantum optical predictions, atoms and ions have naturally lead the way since the 1960's. The development of superconducting quantum interference devices (SQUIDs) has proven serious competition in the past 10 years [25, 26]. QDs have become nevertheless increasingly visible in this domain [27]. Most notably, the prediction that a TLS emits quadrature squeezed photons was first experimentally verified utilising QDs [28].

[2]Recently, it has been shown that this criterion is sufficient but not necessary to obtain maximally entangled states. Temporal post-selection allows one to extract maximally entangled photon pairs even in the presence of a finestructure splitting [17, 18]

Wenn mir Einstein ein Radiotelegramm schickt, er habe nun die Teilchennatur des Lichtes endgültig bewiesen, so kommt das Telegramm nur an, weil das Licht eine Welle ist.

Niels Bohr

2

Theoretical aspects

The following chapter aims to present a concise theoretical treatment of the central the phenomena studied in the experiments presented in the chapters 5 and 6. First, we introduce the (heuristic) quantisation of the electromagnetic field which leads to the notion of photons. The developed formalism then allows one to treat the detection of photons and consecutively the photon statistics of light fields. Following this brief detour into quantum electrodynamics we turn to the two-level system and its interaction with electromagnetic radiation. This topic is treated in somewhat greater detail as it is central to the experiments presented in chapter 5. We extend this topic a little further into the direction of the two-photon excitation of a three-level ladder system as it is pertinent to the experiments presented in chapter 6. Finally, we will discuss some aspects of semiconductor QDs, the core subject of this thesis. They represent the physical realisation of a two- and three-level system. All formulas are written in the units defined by the International System of Units (SI) .

2.1 Quantisation of the electromagnetic field

Most of classical electrodynamics is contained in Maxwell's equations. They connect the electric $\mathbf{E}(\mathbf{r},t)$ and magnetic field $\mathbf{B}(\mathbf{r},t)$ to the charge and current densities ρ and $\mathbf{j}$, respectively. In differential form, they are given by

$$\nabla\mathbf{E} = \frac{\rho}{\epsilon_0}\,, \qquad \nabla\times\mathbf{E} = -\frac{\partial\mathbf{B}}{\partial t}\,, \tag{2.1a}$$

$$\nabla\mathbf{B} = 0\,, \qquad \nabla\times\mathbf{B} = \mu_0\big(\mathbf{j} + \epsilon_0\frac{\partial\mathbf{E}}{\partial t}\big)\,, \tag{2.1b}$$

where ϵ_0 and μ_0 are the electric permittivity and magnetic permeability of the vacuum, respectively [29]. The two vector fields $\mathbf{E}$ and $\mathbf{B}$ are connected via the vector potential $\mathbf{A}(\mathbf{r},t)$ and the scalar field $\phi(\mathbf{r},t)$:

$$\mathbf{B} = \nabla\times\mathbf{A}\,, \qquad \mathbf{E} = -\nabla\phi - \frac{\partial\mathbf{A}}{\partial t}\,. \tag{2.2}$$

Upon short inspection, it can be seen that equations 2.2 are invariant under the so called gauge transformations

$$\mathbf{A}'(\mathbf{r},t) = \mathbf{A}(\mathbf{r},t) + \nabla F(\mathbf{r},t)\,, \tag{2.3a}$$

$$\phi'(\mathbf{r},t) = \phi(\mathbf{r},t) - \frac{\partial}{\partial t}F(\mathbf{r},t)\,, \tag{2.3b}$$

where F is an arbitrary function of $\mathbf{r}$ and t. One important gauge is the so called Coulomb gauge which fixes this redundancy by setting

$$\nabla\mathbf{A} = 0\,. \tag{2.4}$$

In free space, i.e. $\rho = 0$ and $j = 0$, the wave equation

$$\Delta\mathbf{A} - \frac{1}{c^2}\frac{\partial^2\mathbf{A}}{\partial t^2} = 0 \tag{2.5}$$

can be derived from equations 2.1. One important class of solutions of this equation are plane waves. If we now consider a field contained in a cubic box of volume $V = L^3$ with periodic boundary conditions we can expand $\mathbf{A}(\mathbf{r},t)$ in a Fourier series as

$$\mathbf{A}(\mathbf{r},t) = \frac{1}{\sqrt{V}}\sum_{\mathbf{l}} c_l \mathbf{u}_\mathbf{l}(t) e^{i\mathbf{k}_\mathbf{l}\mathbf{r}}\,, \tag{2.6}$$

where $\mathbf{k}_\mathbf{l}$ obeys

$$(\mathbf{k}_\mathbf{l})_{x,y,z} = \frac{2\pi}{L} n_{x,y,z}\,. \tag{2.7}$$

We can separate the field $\mathbf{A}(\mathbf{r},t)$ into two components

$$\mathbf{A}(\mathbf{r},t) = \mathbf{A}(\mathbf{r},t)^{(+)} + \mathbf{A}(\mathbf{r},t)^{(-)} \tag{2.8}$$

$$= \frac{1}{\sqrt{V}}\sum_{\mathbf{l}} c_l \tilde{\mathbf{u}}_\mathbf{l} e^{-i\omega_l t} e^{i\mathbf{k}_\mathbf{l}\mathbf{r}} + c_l^* \tilde{\mathbf{u}}_\mathbf{l}^* e^{i\omega_l t} e^{-i\mathbf{k}_\mathbf{l}\mathbf{r}}\,, \tag{2.9}$$

where we introduced $\mathbf{u}_l(t) = \tilde{\mathbf{u}}_l e^{-i\omega t}$. Furthermore it should be noted that the Coulomb gauge (cf. equation 2.4) imposes a transversality condition, i.e. $\mathbf{k}_\mathbf{l}\mathbf{u}_\mathbf{l} = 0$ which can be satisfied by

$$\tilde{\mathbf{u}}_{l,\mu} = u_{l,\mu}\epsilon_{\mathbf{l},\mu}\,, \tag{2.10}$$

where $\epsilon_{l,\mu}$ is the unit polarisation vector and $\mu = 1, 2$ is the polarisation index.

By substituting the coefficients $u_{l,\mu}$ ($u^*_{l,\mu}$) by the bosonic operators $\hat{a}_{l,\mu}$ ($\hat{a}^\dagger_{l,\mu}$) which obey the usual bosonic commutation relations we arrive at the quantised form of the vector fields $\mathbf{A}$ and $\mathbf{E}$

$$\mathbf{E}(\mathbf{r},t) = \mathbf{E}^{(+)} + \mathbf{E}^{(-)} = \sum_{l,\mu}\sqrt{\frac{\hbar\omega_l}{2\epsilon_0 V}}\epsilon_{l,\mu}\left(\hat{a}_{l,\mu}e^{i(\mathbf{k}_l\mathbf{r}-\omega_l t)} + \hat{a}^\dagger_{l,\mu}e^{-i(\mathbf{k}_l\mathbf{r}-\omega_l t)}\right), \tag{2.11a}$$

$$\mathbf{A}(\mathbf{r},t) = -i\sum_{l,\mu}\sqrt{\frac{\hbar}{2\omega_l\epsilon_0 V}}\epsilon_{l,\mu}\left(\hat{a}_{l,\mu}e^{-i(\omega_l t-\mathbf{k}_l\mathbf{r})} + \hat{a}^\dagger_{l,\mu}e^{i(\omega_l t-\mathbf{k}_l\mathbf{r})}\right). \tag{2.11b}$$

The Hamiltonian of the radiation field is thus given by [30]

$$\hat{H} = \sum_{l,\mu} \hat{H}_{l,\mu} = \sum_{l,\mu} \hbar\omega_l (\hat{a}^\dagger_{l,\mu}\hat{a}_{l,\mu} + \frac{1}{2}) = \sum_{l,\mu} \hbar\omega_l (\hat{n}_{l,\mu} + \frac{1}{2}) \,. \tag{2.12}$$

The evolution of the field is therefore described by a superposition of quantised harmonic oscillators. The excitations $\hat{n}$ of this field are referred to as photons.

2.2 Photon correlations and higher order coherence

The quantisation of the electromagnetic field led to the formalisation of the concept of a photon. It settled and reconciled the century old dispute whether light is of corpuscular or wave like nature.

While Einstein had already postulated the existence of *Lichtquanten* in 1905 [31], it took more than 70 years to directly evidence the quantisation of the electromagnetic field experimentally [32]. This was enabled by the revolutionary experiments by Hanbury-Brown and Twiss in 1956 [33] who were the first to investigate higher order correlations functions in optics. Since then, the concept of correlation functions (of arbitrary order) has become central to the field of optics as they grant experimentally an easy access to the statistical properties of a light field.

2.2.1 Correlation functions

First, we consider an ideal photon detector which absorbs a photon with unity probability. The detection rate $I(\mathbf{r}, t)$ can then be given as

$$I(\mathbf{r}, t) = Tr\{\hat{\rho} E^{(-)}(\mathbf{r}, t) E^{(+)}(\mathbf{r}, t)\} \,, \tag{2.13}$$

where $\hat{\rho}$ is the density operator of the light beam. Bearing in mind equation 2.11b the n-th order correlation function of the electromagnetic field can then be defined as

$$g^{(n)}(t_1 \dots t_n) = \frac{\langle : \prod_{i=1}^{n} \hat{n}(t_i) : \rangle}{\prod_{i=1}^{n} \langle : \hat{n}(t_i) : \rangle} \,, \tag{2.14}$$

where : ... : denotes normal ordering. In the following, we will in particular concentrate on the correlation functions of the 1st and 2nd order which are of particular relevance to our experiments.

First-order coherence

Until the 1950's coherence of an optical field was exclusively synonymous to the quantity $\langle E^*(t) E(t+\tau) \rangle$ which is measurable by means of a Michelson interferometer. This quantity is connected via the Wiener-Khinchin theorem to the spectral density of the electric field $S_E(\omega)$ [34]

$$S_E(\omega) = \Re\{ \int_{-\infty}^{\infty} \langle E^*(t) E(t+\tau) \rangle e^{i\omega\tau} d\tau \} \,. \tag{2.15}$$

The first order coherence function $g^{(1)}(\tau)$ furnishes information about the phase stability of a given light field but does not allow one to draw conclusions about the statistical properties of the light field.

The normalised degree of first-order coherence is

$$g^{(1)}(\tau) = \frac{\langle \hat{a}^\dagger(t)\hat{a}(t+\tau)\rangle}{\langle \hat{a}^\dagger(t)\hat{a}(t)\rangle}\,. \tag{2.16}$$

Second-order coherence

Correlating the intensities as opposed to the electric fields furnishes information about the intensity statistics, i.e. photon-number fluctuations, in a light field. The degree of second-order coherence of a single-mode field can be written as

$$g^{(2)}(\tau) = \frac{\langle \hat{a}^\dagger(t)\hat{a}^\dagger(t+\tau)\hat{a}(t+\tau)\hat{a}(t)\rangle}{\langle \hat{a}^\dagger(t)\hat{a}(t)\rangle^2}\,. \tag{2.17}$$

For classical electromagnetic fields, 2.17 fulfils the Cauchy-Schwartz inequality

$$1 \leq g^{(2)}(0) \leq \infty \tag{2.18}$$

from which follows in particular that

$$g^{(2)}(\tau) \leq g^{(2)}(0)\,. \tag{2.19}$$

Violations of equation 2.19 were predicted to arise in the resonance fluorescence emitted by TLSs and constituted indeed the first direct evidence for the quantisation of the electromagnetic field, i.e. the existence of photons [32]. The $g^{(2)}(0)$ value can be calculated for the different photon statistics using the following relationship

$$g^{(2)}(0) = 1 + \frac{(\Delta n)^2 - \langle \hat{n}\rangle}{\langle \hat{n}\rangle^2}\,, \tag{2.20}$$

where $(\Delta n)^2 = \langle \hat{n}^2\rangle - \langle \hat{n}\rangle^2$ is the variance.

2.3 Light fields

In this section, we briefly revisit the three main classes of light fields typically discussed in textbooks on quantum optics which are the Fock, coherent and thermal state. For the sake of simplicity, we will mostly consider single mode fields contained in a cavity. Continuous progress in experimental techniques has allowed the creation and detection of ever more fragile and artificial states in the laboratory such as squeezed states, Schrödinger cat states and bi- and multipartite entangled states [35]. For more in depth treatment of this topic we refer the reader to the following sources[36–38].

2.3.1 Fock number states

The so called Fock number states are the eigenstates of the Hamiltonian of the free electromagnetic field given in equation 2.12,

$$\hat{a}^\dagger\hat{a}\,|n_k\rangle = \hat{n}\,|n_k\rangle = n_k\,|n_k\rangle\,. \tag{2.21}$$

They form a complete, orthonormal set of states. The experimental creation of such states for $n > 1$ remains challenging even today. Single photons emitted during spontaneous emission from a two-level system , albeit multimode, are a typical example of such one photon states. They are an eigenstate of the total number operator $\hat{N} = \sum_k \hat{n}_k$ but not of $\hat{n}_k$ and accordingly neither of $\hat{H}$. They can be written as

$$|1\rangle = \sum_k c_k \, |0, .., n_k = 1, ..0\rangle \ , \tag{2.22}$$

where $\sum_k |c_k|^2 = 1$.

The direct observation of such states using homodyne detection schemes [39, 40] or photon-number resolving detectors [41, 42] remains equally tricky as every kind of loss contaminates the signal with unwanted vacuum, i.e. $|0\rangle$. Therefore, the easiest way to evidence single photon states is by measuring the second-order autocorrelation function which is impervious to losses. The $g^{(2)}(\tau)$ function of a single mode Fock state at $\tau = 0$ can be written as

$$g^{(2)}(0) = 1 - \frac{1}{n} \, , \tag{2.23}$$

where n is the number of light quanta in the mode. Evidently, single photon states represent one class of light states that violate equation 2.18. It is therefore one prominent example of a non-classical light field. The phenomenon that $g^{(2)}(0) < 0$ (cf. Fig. 2.1) is sometimes referred to as antibunching due to the fact that the photons in such light fields never arrive in bunches at a detector and are separated in time. The photon-number distribution of such states is given by

$$p(n) = \sum_k \delta_{nk} \, . \tag{2.24}$$

The relative uncertainty $\delta n = \frac{\Delta n}{\langle \hat{n} \rangle}$ obviously vanishes for a Fock state while its phase is completely undefined.

2.3.2 Coherent states

These states are often called the most classical of all states as their properties most closely resembles the monochromatic solution of the wave equation in the limiting case of large average photon numbers $\langle \hat{n} \rangle$. Nevertheless it is also the most artificial light field as it cannot be found in nature. A typical man made source of coherent light are lasers well above the threshold which produce light with characteristics reasonably close to the theoretical idea. The coherent state $|\alpha\rangle$ is an eigenstate of the annihilation operator and can be expressed as

$$\hat{a} \, |\alpha\rangle = \alpha \, |\alpha\rangle = e^{-\frac{1}{2}|\alpha|^2} \sum_n \frac{\alpha^n}{\sqrt{n!}} \, . |n\rangle \, . \tag{2.25}$$

Coherent states are overcomplete, i.e. they do not represent a orthonormal basis of the electromagnetic field. The photon-number distribution of a coherent state is given by

$$p(n) = \frac{\langle \hat{n} \rangle^n exp(-\langle \hat{n} \rangle)}{n!} \, . \tag{2.26}$$

This Poissonian distribution is shown in Fig.2.1 (b) for different average photon numbers. The relative uncertainty for a given coherent state is $\delta n = \frac{1}{\sqrt{n}}$ which vanishes for large $\langle \hat{n} \rangle$. This property has

important consequences for experiments since in the limit of large $\langle \hat{n} \rangle$ the coherent state resembles a classical light wave and the amplitude fluctuations of the field become negligible. Evaluation of the degree of second-order coherence for a coherent state yields

$$g^{(2)}(\tau) = 1\,. \tag{2.27}$$

This signifies that the conditional detection of photons of a field prepared in a coherent state shows no correlations.

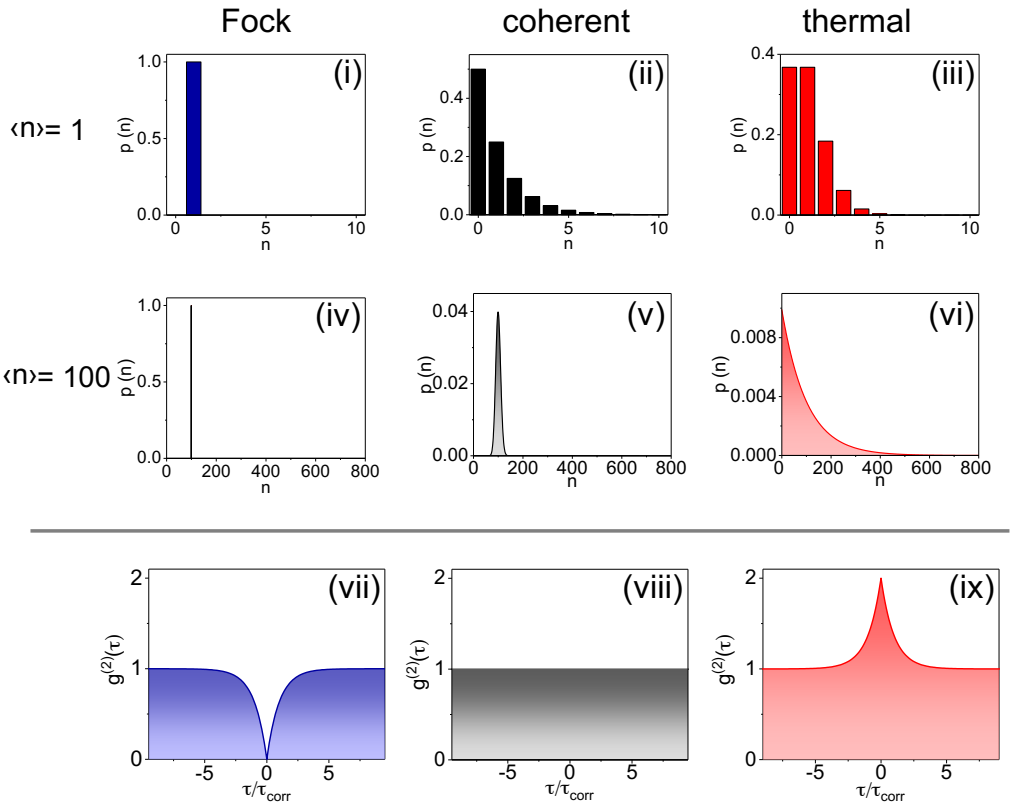

Figure 2.1: Photon-number distributions for different light fields and degree of second-order coherence functions. (i),(iv),(vii) Fock state, (ii),(v),(viii) coherent state, (iii),(vi),(ix) thermal state.

2.3.3 Thermal fields

Virtually all light occurring in nature exhibits thermal photon statistics. In contrast to the previous two examples, a thermal field is not a pure but a mixed state. Consequently, the state has to be represented in a density operator where the photons are distributed over the different number states according to the Bose-Einstein distribution. A single mode thermal field can be written as [36]

$$\hat{\rho} = \frac{exp[-\hbar\omega\hat{a}^{\dagger}\hat{a}/k_b T]}{\mathrm{Tr}\{exp[-\hbar\omega\hat{a}^{\dagger}\hat{a}/k_b T]\}}\,. \tag{2.28}$$

Calculating the photon-number distribution in this mode gives, as expected, the Bose-Einstein distribution

$$p(n) = \frac{\langle \hat{n} \rangle^n}{(1 + \langle \hat{n} \rangle)^{(n+1)}} \,. \tag{2.29}$$

Contrary to the coherent case, the relative uncertainty δn tends towards 1 for large average photon numbers which illustrates the important intensity fluctuations present in thermal fields. The $g^{(2)}(\tau)$ function of a single mode thermal light field with a Lorentzian spectrum is given by

$$g^{(2)}(\tau) = 1 + e^{-\frac{|\tau|}{\tau_{\text{corr}}}} \,. \tag{2.30}$$

The fact that thermal fields show strong correlations at zero time delay, i.e. $g^{(2)}(0) = 2$, signifies that photons in a thermal field tend to arrive in bunches at a detector. Thermal light with a Gaussian spectrum exhibits also a Gaussian bunching in the $g^{(2)}(\tau)$ function. This can be easily understood by recalling the following. Firstly, the first order coherence function is the Fourier transform of the power spectral density as stated by equation 2.15 and secondly the Siegert relation

$$g^{(2)}(\tau) = 1 + |g^{(1)}(\tau)|^2 \,, \tag{2.31}$$

which establishes a simple relationship between the degree of second and first order coherence for thermal fields. Thus a thermal source with a Lorentzian spectrum will exhibit an intensity autocorrelation function with an exponentially decaying bunching while a Gaussian spectrum entails also a Gaussian bunching in the second-order coherence function.

2.4 Two-level systems

Next to the harmonic oscillator and the hydrogen atom, the two-level system is one of the standard toy models of quantum mechanics as it allows one to study perturbations, e.g. light- matter interaction, on a fundamental level. The theory was first developed in the 1930's [43] to describe the interaction of a 1/2-spin, the prototype of a two-level system, and a magnetic field as encountered in nuclear magnetic resonance experiments pioneered notably by Rabi, Bloch, Purcell and coworkers [44–46].

Despite its conceptual simplicity, it describes a surprising wealth of phenomena ranging from the Mollow triplet to the generation of quadrature squeezed photons [47]. Today, the TLS (also more fancily known as qubit) represents the building block of quantum information science which has established an entirely new language and formalism around it [48, 49]. There are many different levels of sophistication for treating the problem theoretically especially when taking into account the complex and mostly detrimental effects of an environment which are abundant in solid state systems. This so called decoherence typically leads to a loss of information, i.e. the initially pure state of the TLS evolves into a mixed state.

2.4.1 Optical Bloch equations

We adopt the semi-classical approach where the driving field is treated as a classical plane wave (i.e. $dE(t) = \hbar\Omega\cos(\omega t)$ where $\Omega = dE_0/\hbar$ is the Rabi frequency) and the TLS (consisting of the ground state $|1\rangle$ and the excited state $|2\rangle$) is treated quantum mechanically. The Hamiltonian in the rotating

frame reads

$$\hat{H} = -\Delta\hat{\sigma}_{22} + \frac{\Omega}{2}(\hat{\sigma}_{12} + \hat{\sigma}_{21}) , \tag{2.32}$$

where $\Delta = \omega_L - \omega_0$ denotes the detuning between the laser and the transition frequency and $\hat{\sigma}_{ij} = |i\rangle\langle j|$ .This transformed Hamiltonian is time independent and its eigenenergies are

$$E_{\pm} = -\frac{\hbar\Delta}{2} \pm \frac{\hbar\tilde{\Omega}}{2} , \tag{2.33}$$

where $\tilde{\Omega} = \sqrt{\Omega^2 + \Delta^2}$ is the generalised Rabi frequency. The corresponding eigenstates are given by a rotation of the bare states

$$|+\rangle = \sin\theta\,|g\rangle + \cos\theta\,|e\rangle , \tag{2.34a}$$
$$|-\rangle = \cos\theta\,|g\rangle - \sin\theta\,|e\rangle , \tag{2.34b}$$

where the rotation angle θ is defined as

$$\tan 2\theta = -\frac{\Omega}{\Delta} . \tag{2.35}$$

The eigenenergies of the coupled and uncoupled system in the rotating frame are shown in Fig. 2.2 as a function of detuning . The coupling leads to an avoided crossing on resonance where the splitting is given by the Rabi frequency Ω. On resonance the eigenstates are an equal superposition of the uncoupled states, e.g. $|+\rangle = 1/\sqrt{2}\,|g\rangle + 1/\sqrt{2}\,|e\rangle$. As is evident from equation 2.35 the mixing of the states can be changed by detuning the light field. Eigenstates very similar to these also arise in the

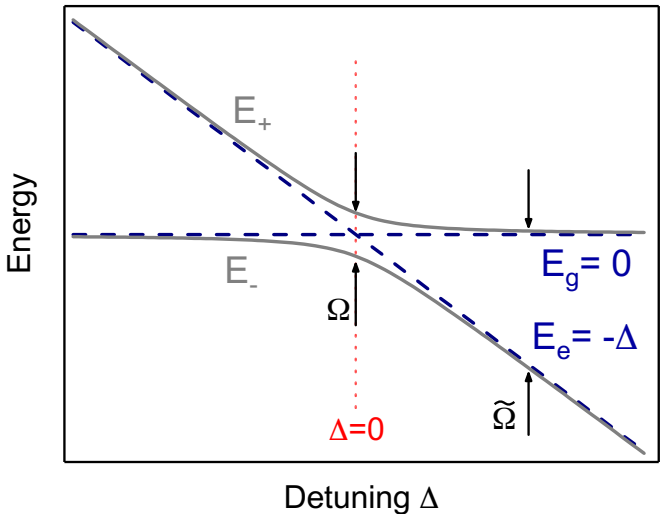

Figure 2.2: Solid (dashed) lines: Energy diagram depicting the eigenstates of the coupled (uncoupled) two-level system in the rotating frame as a function of the detuning Δ.

fully quantised theory where they are called dressed states. They lend themselves, as we will see in section 2.4.2, to a simple and elegant interpretation of resonance fluorescence experiments. For now, we return to the bare states to investigate the dynamic and stationary solution of the atomic populations.

To this end, we assume a radiative decay of the electronic states to a Markov continuum to obtain the master equation [50]

$$\begin{aligned}\frac{d\hat{\rho}}{dt} = -\frac{i}{\hbar}([-\Delta\hat{\sigma}_{22} + \frac{\Omega}{2}(\hat{\sigma}_{12} + \hat{\sigma}_{21}), \hat{\rho}] \\ + \Gamma_1 D[\hat{\sigma}_{12}]\hat{\rho} + \frac{\gamma}{2}D[\hat{\sigma}_{22} - \hat{\sigma}_{11}]\hat{\rho})\end{aligned} \tag{2.36}$$

where $D[\hat{\sigma}]\hat{\rho} = \hat{\sigma}\hat{\rho}\hat{\sigma}^\dagger - \frac{1}{2}\{\hat{\sigma}^\dagger\hat{\sigma}, \hat{\rho}\}$. The decay rate $\Gamma_1 = 1/T_1$ describes the spontaneous, radiative decay of the population while the decay constant $\gamma = 1/T_2^*$ is used to capture pure dephasing, i.e. processes that only lead to a decay of the coherences and not the population of the TLS. From which we yield the following set of coupled differential equations:

$$\dot{\rho}_{11}(t) = i\frac{\Omega}{2}(\rho_{10}(t) - \rho_{01}(t)) - \frac{1}{T_1}\rho_{11}(t)\,, \tag{2.37a}$$

$$\dot{\rho}_{00}(t) = -i\frac{\Omega}{2}(\rho_{10}(t) - \rho_{01}(t)) + \frac{1}{T_1}\rho_{11}(t)\,, \tag{2.37b}$$

$$\dot{\rho}_{01}(t) = \dot{\rho}_{10}^*(t) = -(\frac{1}{T_2} + i\Delta)\rho_{01}(t) - i\frac{\Omega}{2}(\rho_{11}(t) - \rho_{00}(t))\,. \tag{2.37c}$$

These equations are the famous optical Bloch equations. Here, we have introduced the following commonly used relation

$$\frac{1}{T_2} = \frac{1}{2T_1} + \frac{1}{T_2^*}\,. \tag{2.38}$$

Systems where the pure dephasing time T_2^* is infinite are said to be limited by radiative dephasing and the emitted photons are accordingly said to be Fourier-limited. In most solid state systems however, T_2^* is not infinite even at cryogenic temperatures and considerable effort has been invested into identifying and understanding the exact microscopic mechanisms.

Stationary solutions

The total intensity scattered by the TLS is proportional to the steady-state solution of the excited state (cf. equation 2.37a) which is given by

$$I_{\text{tot}} \propto \rho_{11}(t \longrightarrow \infty) = \frac{\Omega^2 T_1 T_2}{2}\frac{1}{1 + \Delta^2 T_2^2 + \Omega^2 T_1 T_2} = \frac{S}{2(1+S)}\,. \tag{2.39}$$

For the last simplified term on the right, we used the definition of the saturation parameter S

$$S := \frac{\Omega^2 T_1 T_2}{1 + \Delta^2 T_2^2}\,, \tag{2.40}$$

which is proportional to the intensity and has a Lorentzian profile with a full width at half maximum (FWHM) of $2/T_2$. Furthermore, one usually defines the saturation Rabi frequency for $S = 1$, i.e. $\Omega_{\text{sat}} = \frac{1}{\sqrt{T_1 T_2}}$. Typical coherent phenomena such as Rabi oscillations and the Mollow triplet are observable for excitation conditions exceeding this value as the dynamics will be dominated by the Rabi frequency in this regime.

The saturation behaviour of equation 2.39 shows that for small S the excitation grows linearly and saturates for large S towards the steady-state value of 1/2. Additionally, equation 2.39 reproduces

the effect known as power broadening [51, 52]. The full width at half maximum as a function of the excitation power is given by

$$\mathrm{FWHM} = \frac{2}{T_2}\sqrt{1+\Omega^2 T_1 T_2}\,. \tag{2.41}$$

For vanishing driving fields ($\Omega \to 0$) the linewidth (FWHM) is $2/T2$ while for large driving powers the linewidth increases as $2\Omega\sqrt{T_1/T_2}$. In addition to absorption, the response of a TLS features a dispersive

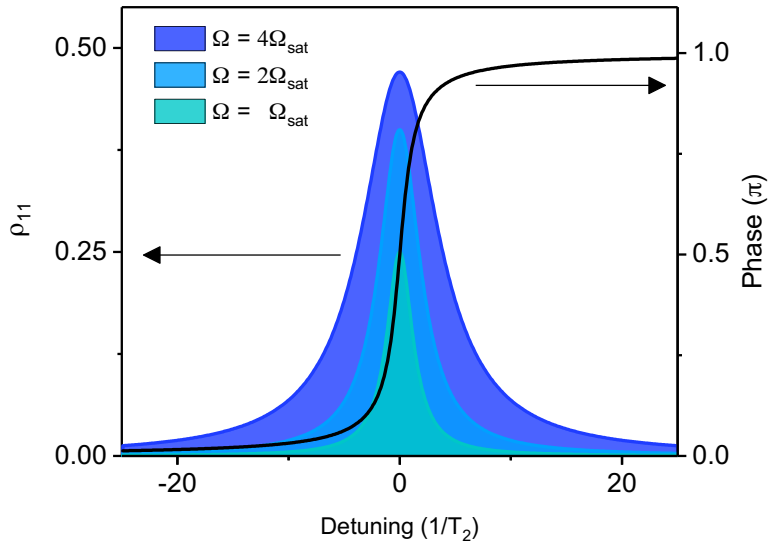

Figure 2.3: Blue shaded curves: Population of the excited state as a function of detuning for three different Rabi frequencies ($\Omega = \Omega_{\mathrm{sat}}, 2\Omega_{\mathrm{sat}}, 4\Omega_{\mathrm{sat}}$). Black solid line: phase lag induced by two-level system.

part which translates into a phase shift that is induced [28, 53, 54]. This phase shift can be calculated from the stationary solution of the coherences according to

$$\phi = \arctan\frac{\mathrm{Im}(\rho_{01}^{\mathrm{st}})}{\mathrm{Re}(\rho_{01}^{\mathrm{st}})} = \arctan(-\frac{1}{T_2\Delta}) = \arctan(T_2\Delta) + \frac{\pi}{2}\,. \tag{2.42}$$

Dynamic solutions

The analytic solution of equation 2.37a for a resonantly driven TLS initially prepared in the ground state reads

$$\rho_{11}(t) = \frac{1}{2}\frac{\Omega^2}{\Omega^2 + 1/(T_1T_2)}\left[1 - e^{\Gamma_+|\tau|}\left(\cos(\Omega_R|\tau|) + \frac{\Gamma_+}{\Omega_R}\sin(\Omega_R|\tau|)\right)\right], \tag{2.43}$$

where $\Gamma_+ = 3/(4T_1) + 1/(2T_2)$ and $\Omega_R = \sqrt{\Omega^2 - 1/(4T_1)^2 + 1/(2T_2)^2}$. These oscillations of the population of a driven TLS are known as Rabi oscillations. It can also be shown that the intensity autocorrelation function of a resonantly driven two-level system follow the very same equation (only the scaling factor

is dropped due to normalisation) [55]. An analytic solution is given on resonance by

$$g^{(2)}(\tau) = 1 - e^{\Gamma_+|\tau|}(\cos(\Omega_R|\tau|) + \frac{\Gamma_+}{\Omega_R}\sin(\Omega_R|\tau|)) . \tag{2.44}$$

At $\tau = 0$ we know that the system has just emitted a photon and can hence not emit another photon until time on the order of $2\pi\Omega$ has passed. It is thus impossible to detect two photons simultaneously in the resonance fluorescence of a single TLS. This is well illustrated by measurements performed on a single TLS which are shown in Fig. 2.4. Additionally one should note that Rabi oscillations can also be

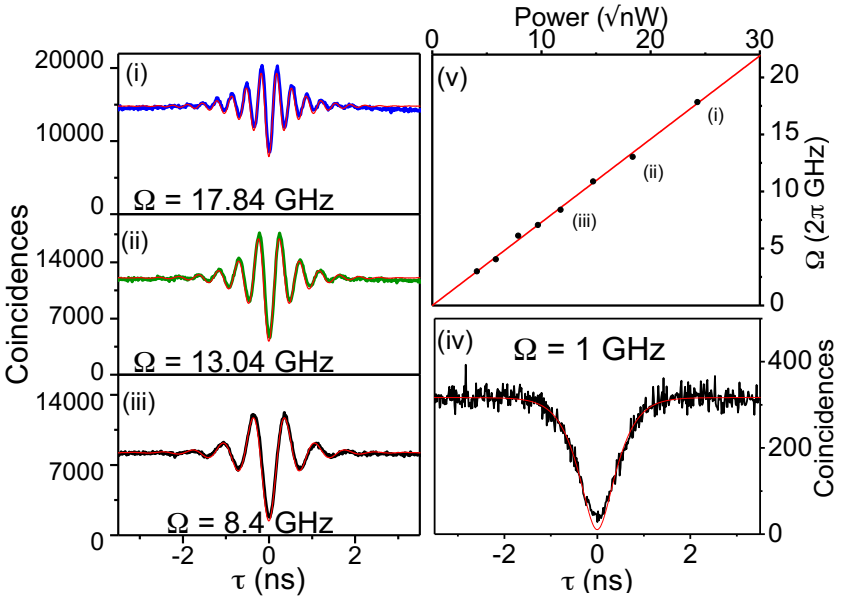

Figure 2.4: (i)-(iv) Experimentally recorded intensity autocorrelation function of a resonantly driven QD under different laser powers using the setup and experimental techniques presented in chapter 3. The data is fit with a convolution of equation 2.44 and a Gaussian (temporal resolution of the detector). (v) Rabi frequency as a function of the square root of the excitation power. The data is well reproduced using a linear fit function in agreement with theory.

observed as a function of the pulse area A

$$A = \int_{-\infty}^{\infty} \Omega(t')dt' , \tag{2.45}$$

where $\Omega(t')$ is the time dependent Rabi frequency. Thus by increasing the Rabi frequency of a pulse of constant temporal length one is also able to "wander" around the Bloch sphere.

At this point we digress a little to combine the results of this section and the preceding one. This means we look at the effect that the photon statistics of a light field have on the response of a TLS. It can be shown that the evolution of a TLS resonant with a single photonic mode inside a cavity [30, 56] is given by

$$\rho_{11}(t) = \sum_{n=0}^{\infty} |C_n|^2 \sin^2(\omega t\sqrt{n+1}) , \tag{2.46}$$

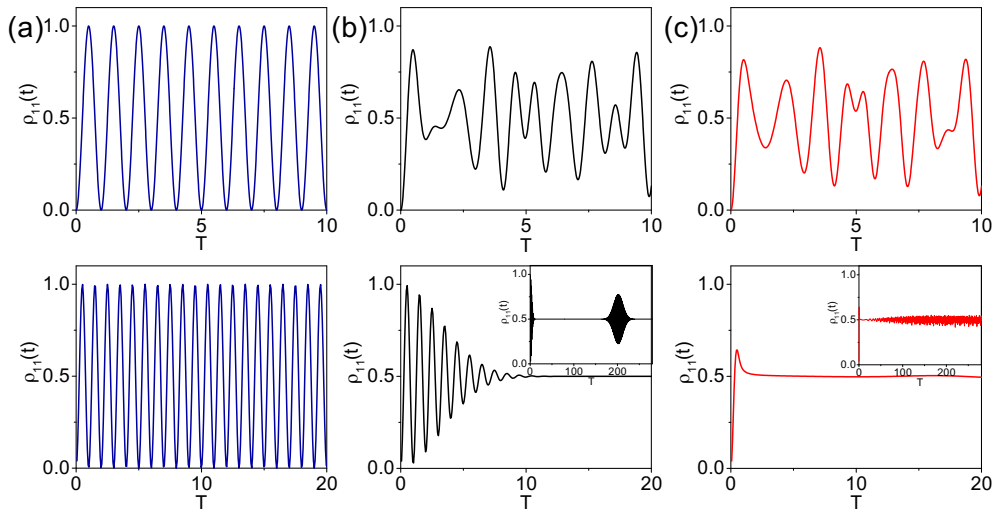

Figure 2.5: From left to right: the population of the excited state ρ_{11} versus time for the TLS initially in the ground state and the single mode cavity field initially in a (a) Fock, (b) coherent and (c) thermal state. Upper (Lower) row: the initial photon number in the cavity mode is n= 1 (100). T is the rescaled time T=$2\pi\omega\sqrt{n+1}$.

where n is the photon number and $|C_n|^2$ the weighting coefficient given by the particular photon-number distribution in the cavity mode. If we now insert for $|C_n|^2$ the different number distribution for a Fock, coherent and thermal state we obtain the evolution of the excited state. We plot the solution for the different statistics in Fig. 2.5 for 1 and 100 photons initially in the cavity mode and the TLS initially prepared in the ground state.

As we can see, for low photon numbers only the system driven by a field prepared in a Fock state exhibits clear Rabi oscillations. The response of the TLS to the thermal and coherent field look very similar as can be expected from the very similar photon-number distribution functions depicted in Fig. 2.1. For large photon numbers however the situation changes. Here clear, undamped Rabi oscillations are visible for excitation by a Fock state and damped oscillations under coherent excitation. It is important to stress that the damping does not occur due to relaxation effects which are not included in the simple model but due to the distribution of the Rabi frequencies which is illustrated by the typical revival of the Rabi oscillations at longer time scales (cf. inset). In contrast, under thermal excitation no steady oscillations occur with only slight oscillations about the means value of 0.5.

2.4.2 Resonance fluorescence

Coherent and incoherent scattering

The light scattered by a two-level system can be decomposed into two parts, i.e. the coherent and the incoherent part:

$$I_{\text{tot}} = I_{\text{coh}} + I_{\text{incoh}} \,. \tag{2.47}$$

As the name suggests, the coherent part is in phase with the driving field while the incoherent part has no fixed phase relation [57]. The coherent part is proportional to the squared magnitude of the

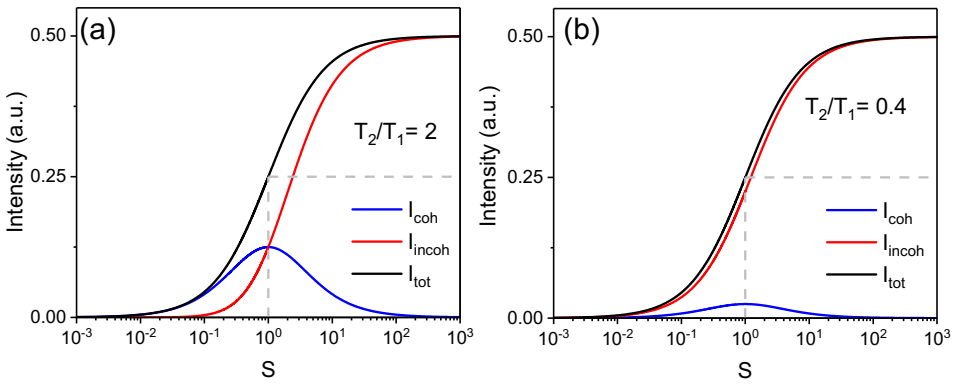

Figure 2.6: Saturation behaviour of a TLS. (a) For a TLS with only radiative dephasing ($T_2/T_1 = 2$). (b) For a TLS with pure dephasing ($T_2/T_1 = 0.4$). The black line represents the total scattered intensity while the blue and red line are the coherently and incoherently scattered intensities, respectively. The dashed line indicates the saturation intensity.

coherences, i.e.

$$I_{\text{coh}}(t) = |\rho_{01}(t)|^2 . \tag{2.48}$$

The fraction of the coherently scattered intensity of the total scattered intensity is [58]

$$\frac{I_{\text{coh}}}{I_{\text{tot}}} = \frac{T_2}{2T_1}\frac{1}{1+S} . \tag{2.49}$$

For systems without pure dephasing, i.e. where $T_2 = 2T_1$, the spectrum consists for $S \ll 1$ essentially only of coherently scattered photons. However, for system with a finite T_2^* time the spectrum contains even at the lowest excitation power incoherently scattered photons with the maximum achievable fraction dictated by $\frac{T_2}{2T_1}$. This is illustrated in Fig. 2.6 where the saturation curves are plotted for a TLS with and without pure dephasing. The incoherently scattered fraction is thus given by

$$I_{\text{incoh}} = I_{tot} - I_{\text{coh}} = \frac{S(1+S-\frac{T_2}{2T_1})}{2(1+S)^2} . \tag{2.50}$$

Emission spectrum

After having compared the integrated intensities we now turn to their respective spectral distribution. As we have seen in chapter 2.2.1, the emission spectrum can be obtained by Fourier transforming the degree of first order coherence. Additionally, it can be shown, that the detected first-order coherence in the far-field can be computed via [57]

$$\langle \hat{E}^{(-)}(\mathbf{r},t)\hat{E}^{(+)}(\mathbf{r},t+\tau)\rangle = I_0(\mathbf{r})\langle \sigma_+(t)\sigma_-(t+\tau)\rangle . \tag{2.51}$$

This two-time correlation function can be calculated by invoking the quantum regression theorem which tells us that two-time correlation functions follow the same equations of motion as one-time

averages [55]. An analytical solution on resonance is given by [59]

$$\begin{aligned} S(\omega) &= S_{\text{coh}}(\omega) + S_{\text{inc}}(\omega)\,, \text{ with} \\ S_{\text{coh}}(\omega) &= \frac{\pi\Gamma_R^2}{\Gamma_R\Gamma_P + \Omega^2}\delta(\omega-\omega_0)\,, \\ S_{\text{inc}}(\omega) &= \frac{\Gamma_P}{\Gamma_P^2 + (\omega-\omega_0)^2} \\ &+ \frac{\Gamma_+ Z_c + Z_s(\omega-\omega_0+\Omega_R)}{2(\Gamma_+^2 + (\omega-\omega_0+\Omega_R)^2)} + \frac{\Gamma_+ Z_c + Z_s(\omega-\omega_0-\Omega_R)}{2(\Gamma_+^2 + (\omega-\omega_0-\Omega_R)^2)}\,, \end{aligned} \tag{2.52}$$

where the systems decay rates are $\Gamma_R = 1/T_1$, $\Gamma_P = 1/T_2$. Furthermore, we introduced the following abbreviations: $\Gamma_\pm = \frac{\Gamma_R \pm \Gamma_P}{2}$, $Z_c = 1 - \frac{\Gamma_R^2}{4\Omega^2 + \Gamma_P\Gamma_R}$, $Z_S = \frac{1}{\Omega_R}(\Gamma_- + \Gamma_R - \frac{\Gamma_+\Gamma_R^2}{\Omega^2+\Gamma_P\Gamma_R})$ and $\Omega_R = \sqrt{\Omega^2 - \Gamma_-^2}$. The (renormalised) Rabi frequency Ω_R gives the splitting between the central peak and the two satellite peaks. As can be seen the existence of pure dephasing in a TLS leads to a renormalisation of the splitting. This effect has been observed in QDs where the contribution of phonons to pure dephasing was evidenced [60].

The coherent and incoherent component have evidently two very distinctive spectral distributions. The δ-function represents the coherently scattered photons dominant at low excitation powers (i.e. $\Omega \ll \Omega_{\text{sat}}$). For high excitation powers (i.e. $\Omega \gg \Omega_{\text{sat}}$) the spectrum consists of three distinct Lorentzian peaks which is known as the Mollow triplet. This triplet is also well known from classical physics where a signal at frequency ω_L is amplitude modulated with a frequency Ω. The spectrum of the modulated signal then exhibits sidebands at the position $\omega_l \pm \Omega$. However, the correct intensity ratios of the peaks and respective linewidths can only be obtained from a fully quantum optical treatment of the problem. The emergence of the Mollow triplet under strong excitation can be handily interpreted in the framework of dressed states [61]. As we have seen in section 2.4.1 the eigenstates of the combined atom-field system on resonance are an equal superposition of the ground and excited state and are split by Ω. Now in a fully quantised system where the photon number $\langle\hat{n}\rangle$ in the laser mode is very large and the fluctuations are accordingly negligible ($\langle\hat{n}\rangle \gg \delta n \gg 1$), these two levels are repeated in energy with a spacing of $\hbar\omega$. The three observed emission lines then correspond to the 4 transitions

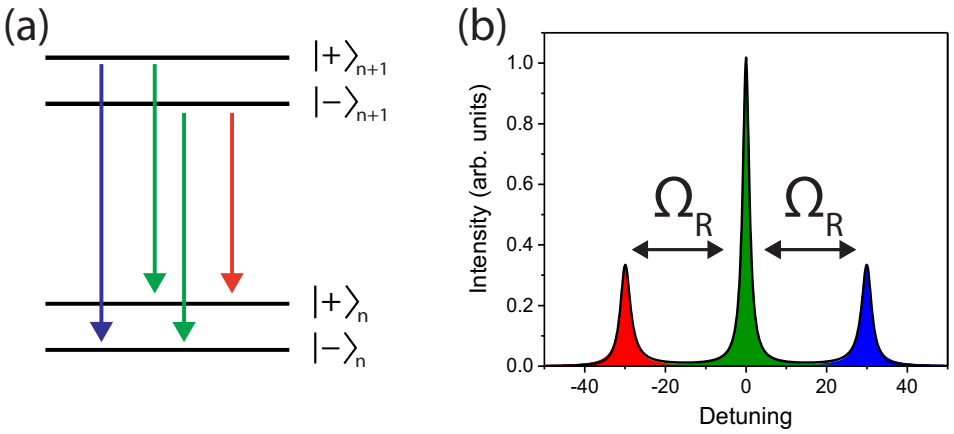

Figure 2.7: (a) Level scheme of a strongly driven TLS in the dressed state basis. The arrows represent the four possible transitions giving rise to the Mollow triplet. (b) Mollow triplet: incoherent spectrum of a strongly driven TLS. The different colours of the peaks correspond to the arrows in Fig. 2.7 (a).

between adjacent rungs of this Autler-Townes ladder. This is sketched in Fig. 2.7 (a). The two green lines ($|+\rangle \rightarrow |+\rangle$ and $|-\rangle \rightarrow |-\rangle$) contribute to the central Rayleigh line while the blue ($|+\rangle \rightarrow |-\rangle$) and red ($|-\rangle \rightarrow |+\rangle$) lines constitute the respective sideband. From this reasoning the peak area ratio of 1:2:1 which is valid for a system without pure dephasing [62] is also easily understandable.

2.5 Three-level systems

Typically, three-level systems are divided into the three following categories: (a) the ladder system, (b) the Λ -system and (c) the V- system which are schematically sketched in Fig. 2.8. In all of these systems the transition between states $|1\rangle$ *and* $|2\rangle$ and $|2\rangle$ *and* $|3\rangle$ are dipole allowed while the transition between $|1\rangle$ *and* $|3\rangle$ is dipole forbidden. Coherent phenomena such as coherent population trapping (CPT) or electromagnetically induced transparency (EIT) can be particularly well studied in Λ-systems [63, 64]. The ladder system on the other hand is attractive as a photonic cascade which was used to demonstrate the violation of the Bell inequalities for the first time by Aspect et al. [65].

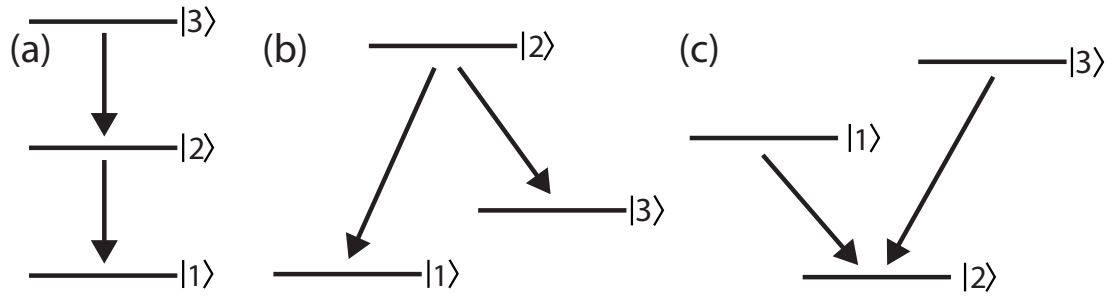

Figure 2.8: The three different configurations of a three level system where the two dipole-allowed transitions are indicated by arrows. (a) ladder (cascade) (b) Λ- and (c) V- system

Two-photon excitation of a ladder system

Besides single photon absorption and emission processes, Maria Göppert-Mayer realised in the 1930's that the laws of quantum mechanics also allow for multi-photon absorption via virtual states [66]. During these processes two or more photons are simultaneously absorbed. In the two-photon case this enables for example the direct excitation of a state which has the same parity as the initial state which is forbidden by dipole selection rules, e.g. between $|1\rangle$ *and* $|3\rangle$ in Fig. 2.8 (a).

We now consider a particular ladder system consisting of an upper state $|B\rangle$, two non-degenerate central states $|H\rangle$ *and* $|V\rangle$ and a ground state $|G\rangle$ (cf. Fig. 2.9 (a)). The two states are orthogonally polarised with respect to one another and a vertically polarised laser drives only the vertical polarisation. The energy E_B of the highest excited state $|B\rangle$ is given by

$$E_B = \hbar(\omega_H + \omega_V) + \Delta E_B\,, \tag{2.53}$$

where $\hbar\omega_H$ ($\hbar\omega_V$) is the energy of the intermediate state H (V) and ΔE_b is an energy shift called biexciton binding energy. This energy shift is significant as it allows to excite the state $|B\rangle$ resonantly without simultaneously driving the states $|H\rangle$ and $|V\rangle$. The Hamiltonian of the system in the rotating

frame of the exciting laser is given by

$$\hat{H} = \Delta_H \hat{\sigma}_{HH} + \Delta_V \hat{\sigma}_{VV} + (\Delta_H + \Delta_V + \Delta E_B)\hat{\sigma}_{BB} + (\Omega_V/2)(\hat{\sigma}_{GV} + \hat{\sigma}_{VG} + \hat{\sigma}_{BV} + \hat{\sigma}_{VB}), \tag{2.54}$$

where $\Delta_H = \omega_H - \omega_L$ and $\Delta_V = \omega_V - \omega_L$ are the detuning between the laser and the transition frequency of the respective state and the operators are $\sigma_{ij} = |i\rangle\langle j|$. The master equation where we take into account a radiative decay into the vacuum then reads in the rotating frame

$$\begin{aligned}\dot{\hat{\rho}} = &-\frac{i}{\hbar}[\hat{H}, \hat{\rho}] \\ &+ \Gamma_{GH} D[\sigma_{GH}]\rho + \Gamma_{HB} D[\sigma_{HB}]\rho + \Gamma_{GV} D[\sigma_{GV}]\rho + \Gamma_{VB} D[\sigma_{VB}]\rho\,.\end{aligned} \tag{2.55}$$

The radiative decay rates are Γ_{ij} which describe the transition between the states $i, j \in (G, V, H, B)$. Out of convenience we neglect pure dephasing and assume equal decay rates in the following discussion.

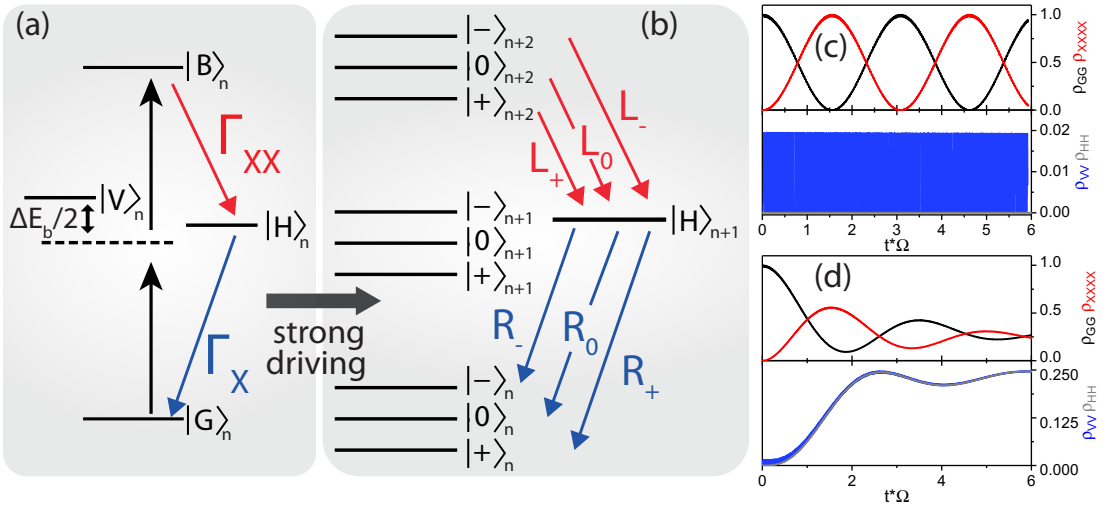

Figure 2.9: (a) Sketch of the two-photon excitation scheme in the effective three level ladder system. The excitation is vertically polarised while the fluorescence is only detected in the horizontal polarization. (b) Level scheme of spontaneously emitted photons detected in the H polarisation in the strongly driven system in the dressed basis. The designation is according to equations 2.57. (c) Temporal evolution of the population of the coherently driven and intermediate states in the absence of relaxation processes. (d) Temporal evolution of the populations including spontaneous emission as described by equation 2.55.

We plot the numerical solution of equation 2.55 without the Lindblad terms in Fig. 2.9 (c). As can be seen, the on resonance driving leads to Rabi oscillations between the ground state $|G\rangle$ and the highest level $|B\rangle$. In addition, we see that the intermediate state $|H\rangle$ is not directly involved in the driving remaining unpopulated. The very fast oscillations with small amplitude visible for ρ_{VV} are simply the driving of a very far detuned TLS as the laser is detuned by half the binding energy from the single photon resonance. This is of course determined by the relative magnitudes of ΔE_B and Ω. By including the Lindblad terms in our model, we obtain Fig. 2.9 (d). Here the Rabi oscillations of the biexciton state and ground state are damped by the coupling to the vacuum and the states reach a steady-state value of 0.25 (under the assumption of equal decay rates from B and H and V). The intermediate states

$|H\rangle$ and $|V\rangle$ are now populated via spontaneous emission from the biexciton and also show very weak oscillations which are solely a consequence of the oscillations in the $|XX\rangle$ state.

Akin to the two-level system we can also find new dressed states for the Hamiltonian of this system given in equation 2.54. In order to facilitate the algebra we now assume degeneracy of the two central states ($\Delta = \Delta_H = \Delta_V$) and set the laser frequency to the two-photon resonance, i.e. $\omega_L = \omega_{H/V} + \Delta E_B/2$. Diagonalisation then yields the eigenvalues

$$E_0 = 0\,, \tag{2.56a}$$

$$E_H = -\frac{\Delta E_B}{2}\,, \tag{2.56b}$$

$$E_- = -\frac{1}{4}(\Delta E_B - \sqrt{\Delta E_B^2 + 8(\Omega\hbar)^2})\,, \tag{2.56c}$$

$$E_+ = -\frac{1}{4}(\Delta E_B + \sqrt{\Delta E_B^2 + 8(\Omega\hbar)^2})\,, \tag{2.56d}$$

and the corresponding eigenvectors are given by

$$|0\rangle = \frac{1}{\sqrt{2}}(|B\rangle - |G\rangle)\,, \tag{2.57a}$$

$$|H\rangle = |H\rangle\,, \tag{2.57b}$$

$$|-\rangle = \frac{1}{\sqrt{2 + 4(\frac{E_-}{\Omega\hbar})^2}}(|G\rangle + \frac{2E_-}{\Omega\hbar}|V\rangle + |B\rangle)\,, \tag{2.57c}$$

$$|+\rangle = \frac{1}{\sqrt{2 + 4(\frac{E_0}{\Omega\hbar})^2}}(|G\rangle + \frac{2E_+}{\Omega\hbar}|V\rangle + |B\rangle)\,. \tag{2.57d}$$

It is important to note that all the new states apart from the H polarised exciton are superpositions of the bare states. Furthermore, the exact superposition of the bare states of the states $|-\rangle$ and $|+\rangle$ depend on the square root of the exciting power on resonance as well as the exciton binding energy.

The total incoherent spectrum can be calculated using $S(\omega) = \lim_{t\to\infty} \int_0^\infty \langle \hat{c}^\dagger(t)\hat{c}(t+\tau)\rangle e^{-i\omega\tau}$ where $\hat{c}(t) = \hat{\sigma}_{iB} + \hat{\sigma}_{Gi}(t)$ for i=H,V. The emission spectrum is plotted for two different excitation powers in Fig. 2.10 (a). For low excitation powers we observe two emission lines (dashed line) at the same energies as the bare states of the exciton and biexciton. This is due to the fact that in this regime the splitting between the states is smaller than the linewidths of the respective transitions. Under strong excitation we observe the emergence of three "Mollow" triplets (solid line), one centred on the two-photon resonance and the other two around the bare emission energies. If we now separate the spectrum into its two linear polarisation components H and V we obtain the two distinct graphs displayed in Fig. 2.10 (b). Both consist of a doublet located around the bare emission energies. For the H polarisation the emission lines closer to the two-photon resonance (i.e. 0) stay fixed while the outer emission lines shift outwards with increasing driving strength. This is in contrast to the V polarisation where both emission lines shift away from zero with increasing Rabi frequencies.

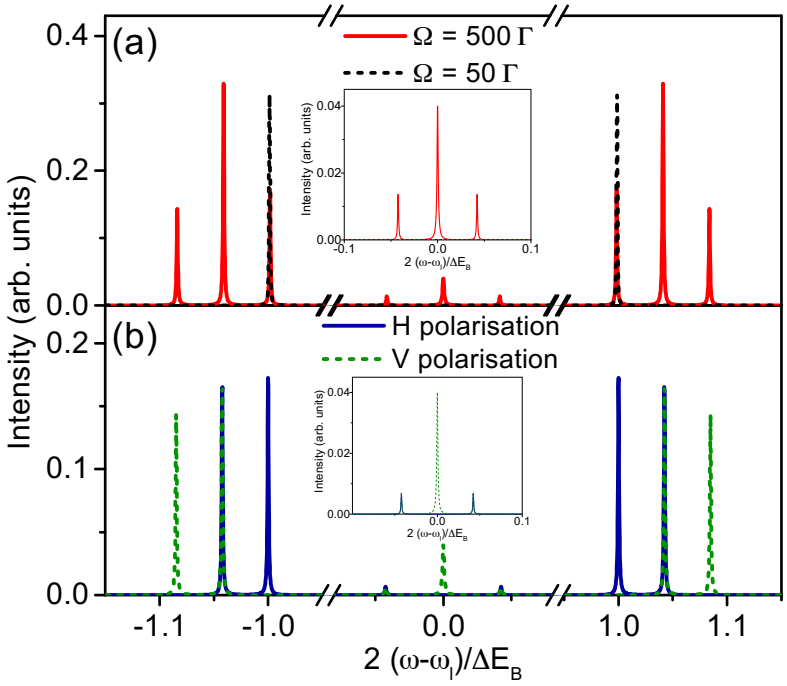

Figure 2.10: Spectra of the resonantly excited ladder system. (a) Spectrum under weak (black dashed line) and strong (red solid line) excitation. Under weak excitation only two emission lines at the bare resonances are visible. Under strong excitation three triplets located at the bare frequencies and the two-photon resonance emerge. (b) Polarisation resolved spectra under strong excitation. The insets are magnifications of the central part of the respective spectrum.

2.6 Solid-state quantum emitters

Atoms exhibit discrete energy levels and their specific complete level structure can become arbitrarily complicated. However, under the condition that the linewidth of the light source and involved states are a lot smaller than the energetic separation between the states and the detuning between the laser and two dipole allowed transition is small compared to all other dipole allowed transitions the interaction can be readily described within the framework of a TLS. Hence most of the earliest experiments in quantum optics were conducted using atoms and could be nicely described with the theory briefly described in the section 2.4. However, it was soon realised that if concepts such as quantum cryptography or quantum information processing were ever to leave the ivory tower of scientific research, more stable and scalable platforms would have to be developed. Nowadays, there is range of more or less advanced quantum emitters in the solid state which offer the prospect of technological scalability and integrability. Most prominent among them are rare earth ions in solids [67], defect centres in wide band gap semiconductors [68, 69] and semiconductor QDs [67].

Semiconductor quantum dots

Quantum dots are so called zero-dimensional semiconductor structures in reference to their discrete, delta-like density of states. The discrete spectrum arises due to the strong confinement of the charge carriers in space. This confinement is achieved by small islands of semiconductor material whose band gap is smaller than the one of the surrounding material. In this thesis, the QD material is always InGaAs ($E_{\mathrm{G}}^{\mathrm{InAs}} \approx 0.36\,\mathrm{eV}$ at room temperature (RT)) which is embedded in GaAs ($E_{\mathrm{G}}^{\mathrm{InAs}} \approx 1.42\,\mathrm{eV}$ at RT) matrix. More specifically, the spatial dimensions of the QD material in all three dimensions need to be smaller or on the order of the Bohr radius a_b of an exciton (i.e. a bound electron-hole pair) in the specific material system which is given by

$$a_b = \frac{4\pi\epsilon_0\epsilon_r\hbar^2}{\mu^* e^2}\,. \tag{2.58}$$

Here ϵ_0 is the relative permittivity and μ^* the reduced effective mass of the electron-hole pair [70]. Typically QDs are small clusters made up of $10^3 - 10^4$ atoms and have a spatial extension of below 100 nm. Due to this property, their delta-like density of states, they are also sometimes referred to as artificial atoms. In contrast to atoms however, their electronic properties can be easily engineered which offers advantages as well as disadvantages. Another appealing aspect is that they are fixed at a specific position in the surrounding matrix which allows for the integration into various photonic and optoelectronic devices such as cavities, waveguides, pin-diodes and lasers [71, 72] .

The observation of emission from single QDs put demanding requirements on the growth and fabrication of the devices. Non-radiative decay channels need to be minimised and dephasing times should be on the order of the natural lifetime. Nevertheless, it is nowadays routinely achieved using various, mostly self-assembled growth techniques. The most frequently applied one is the Stranski-Krastanow (SK) growth mode [73]. Here, a few monolayers of InGasAs is deposited onto a GaAs substrate. This layer is called wetting layer. Due to the lattice mismatch between the two materials it is then energetically favourable for subsequently deposited atoms to form small islands, i.e. QDs.

The QDs used in this thesis are epitaxially grown self-assembled InGaAs/GaAs QDs which are currently the most popular and mature platform in quantum optical research using QDs. Depending on the exact material composition, size and various growth parameters the emission wavelength of the

InGaAs- QDs can be tuned in a large range from about 850-1500 nm.

The two most widely used epitaxy techniques are the molecular beam epitaxy (MBE) and metal organic chemical vapour phase epitaxy (MOVPE). During the MBE the source materials of choice are heated until it slowly starts to sublime in a effusion cell. The gas is then directed as a beam onto the substrate where it condensates. The absence of carrier gases in conjunction with the ultra-high vacuum results in the highest achievable purity of the epitaxially grown films. In contrast, MOVPE does not rely on physical deposition but on a chemical reaction to grow the crystal. This takes place at moderate pressures inside the reaction chamber. MOVPE is currently the standard technique for the large scale fabrication of optoelectronic devices in the industry.

Excitons in quantum dots

InAs and GaAs are both direct semiconductors which means that the maximum of the valence band and the minimum of the conduction band are at the same quasi-momentum (the Γ point) in the Brillouin zone rendering them attractive for the application in optically active devices. At the Γ point, the atomic orbital wavefunction of electrons in the conduction band is primarily made up of the s orbitals of the group III elements (In and Ga, respectively). It is therefore called s-like and is spin degenerate with a total angular momentum $j_z = s_z = \pm 1/2$ (orbital angular momentum l=0). For holes in the valence band the atomic orbital wavefunction is of p-like symmetry. Due to the spin orbit interaction the conduction band is split into three distinct bands: the heavy-hole ($j_z = 3/2, s_z = \pm 3/2$), the light-hole ($j_z = 3/2.s_z = \pm 1/2$) and the split-off band ($j_z = 1/2$). The band diagram at the Γ point is sketched in the schematic in Fig. 2.11 (a).

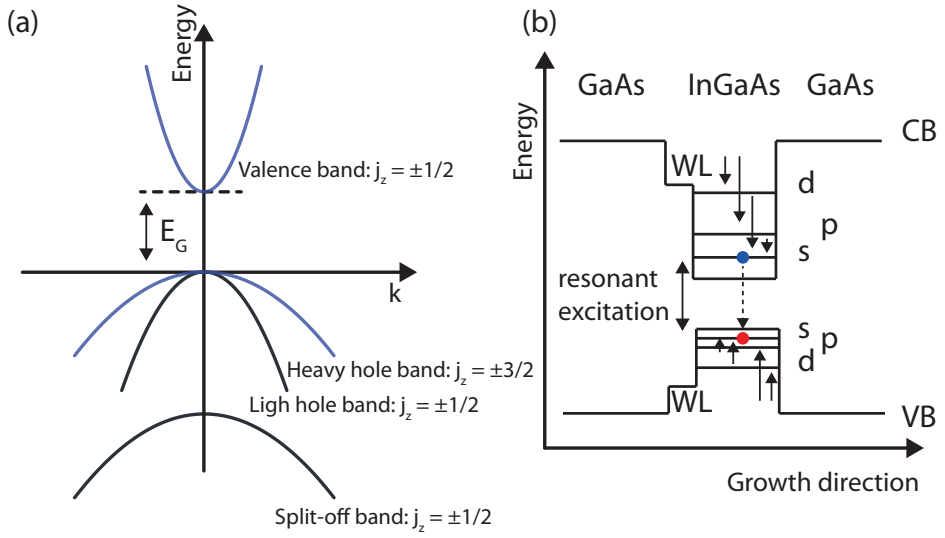

Figure 2.11: (a) Energy band diagram of a direct semiconductor around the Γ point. The split-off band is typically 0.1-1 eV below the lower valence band edge. (b) Schematic of the potential of a InGaAs QD embedded in a GaAs matrix. The one particle states states indicated for electron (holes) in the conduction (valence) band are named s,p,d in analogy to the orbitals of atoms.

After this brief discussion of the electronic properties we now turn to the optical properties of excitons in QDs. An energy band diagram of a QD and its wetting layer embedded in an undoped GaAs matrix is schematically displayed in Fig. 2.11 (b). Also the various optical excitation methods

and possible relaxations paths for electrons and holes are indicated. Excitons, i.e. electron-hole pairs, created in the bulk material or higher excited states quickly relax via scattering processes, e.g. phonon emission to the lowest energetic states for electrons and holes in QDs. These intraband transitions occur on a time scale of ~100 ps at cryogenic temperatures.

From the ground state of the QD, the electron can only relax via an interband transition. This relaxation can only occur if there is an unoccupied state (hole) in the valence band. As discussed above, for electrons the ground state is a s-like state while for holes the ground state is typically a p-like heavy hole state. This means that under the emission of a circularly polarised photon the exciton can recombine. The typical lifetime for an InGaAs QD is on the order of 1 ns.

In most experiments however an analysis of the polarisation of the photons emitted by a neutral exciton reveal typically two linearly polarised components that are perpendicular to one and another. The reason for this observation is rooted in the exchange interaction, i.e. the indistinguishability of particles and the spin statistics of fermions. Without the exchange interaction there are four degenerate spin configurations for the neutral exciton in a QD as shown on the left in Fig. 2.12. In our case quantum mechanics requires the wave function to be antisymmetric when two particles are exchanged. The exchange interaction then leads to a lifting of the degeneracy for the states with parallel spins which are the split by an energy Δ. These states are called dark excitons as the photon emission in the parallel spin configuration is dipole forbidden[1]. The two states with anti-parallel spins (the bright excitons) remain degenerate and can recombine radiatively by emitting circularly polarised photons.

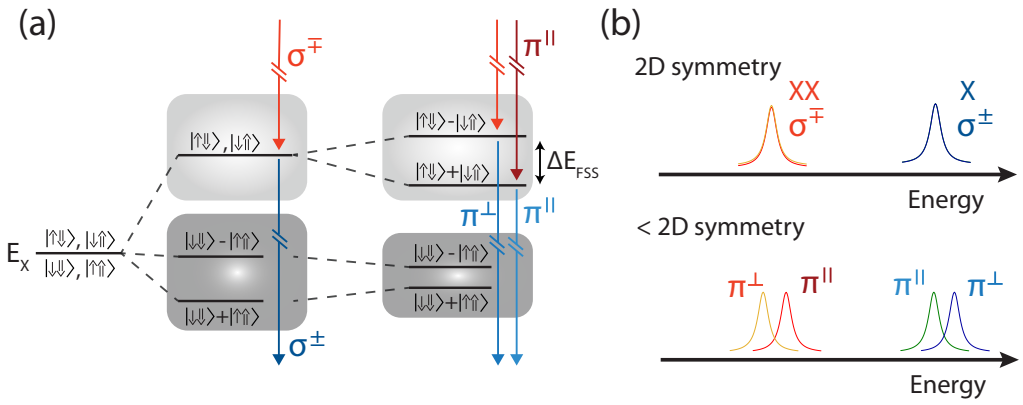

Figure 2.12: (a) From left to right: Level structure of exciton without exchange interaction, with exchange interaction, with exchange interaction in a QD of reduced symmetry. The vertical arrows are optical transitions where σ (Π) designates the circular (linear) polarisation. (b) Optical spectra of the transitions indicated in Fig. (a).

The linear polarisation measured in most experiments is caused by a reduced symmetry of most QDs compared to the ideal circular symmetry. The bright excitonic states in QDs with non perfect circular symmetry are therefore superpositions and emit linearly polarised photons. The difference in emission energy between the two components is called finestructure splitting (FSS) .

[1]This longevity offers interesting prospects for the dark exciton as a quantum memory or for the generation of photon cluster states [74–76].

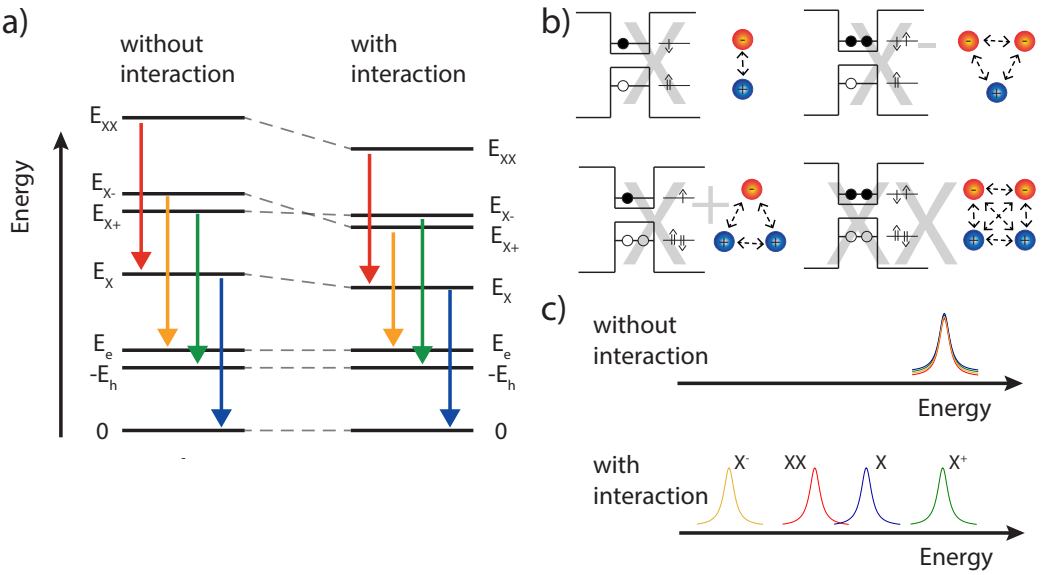

Figure 2.13: (a) Left (right): level scheme with optical transitions of different excitonic complexes without (with) manybody interactions. (b) Distribution of the charge carriers in the different excitonic complexes and respective Coulomb interactions. (c) Bottom (top): Spectra of different excitonic complexes taking the Coulomb interaction (not) into account .

Multi-particle states

Besides neutral excitons (X) there exist several other excited states. The most common ones are sketched in Fig. 2.13 (b). The state consisting of two electrons and two holes of opposite spin in the same shell is called biexciton (XX). An excitation where an exciton and an additional charge carrier are present in the QD is referred to as trion. Depending on the sign of the charge carrier one typically distinguishes between a positively (X^+) and a negatively (X^-) charged exciton. Since these states are many particle states interactions between the particles lead to shifts of the respective emission energies. The most important ones for understanding the spectra of QDs are certainly the (direct) Coulomb and exchange interaction (also referred to as indirect Coulomb interaction).

Figures 2.13 (a) and (d) illustrate the action of the Coulomb interaction on the level scheme and the emission spectrum. In the absence of the Coulomb interaction all transitions have the emission energy. The Coulomb interaction leads to a lowering of the many particle energy states as is depicted in Fig.2.13 (a). This results in a lifting of the degeneracy of the transitions energies. The binding energies are defined relative to the exciton transition energy and are grouped into binding and anti-binding states. Due to their large confinement potential QDs also allow for stable anti-binding states.

If your experiment needs statistics, you ought to have done a better experiment.

Ernest Rutherford

3 Experimental techniques

In this chapter, we will discuss the most important measurement techniques and devices used to conduct the experiments presented in the chapters 4, 5 and 6.

3.1 Optical microscopy

Optical microscopes, as the counterpart to telescopes, are among the oldest instruments used for scientific studies. A large variety of microscopes has been developed adapted to different purposes. In general, a microscope consists of two parts, an objective and an eyepiece. The objective collects the photons scattered by the sample and forms a real intermediate image. This image is then mapped by the eyepiece. In nanooptics, the confocal microscope has become the instrument of choice. Here, an infinity corrected objective collimates the light originating in the focal spot while a second lens focuses the light on a pinhole, i.e. small aperture. Detection of light stemming from outside the focal spot is thus considerably suppressed. The resonance fluorescence (RF) setup built to perform the experiments in this thesis is essentially a confocal dark field microscope and will be described in detail in the following section.

3.1.1 Resonance fluorescence setup

While resonance fluorescence of atoms was already established experimentally in the 1970[77, 78], it has only recently become a standard technique for the study of semiconductor QDs [79–81]. Inspired by atomic optics, early experiments achieved stray light suppression by aligning excitation and detection at right angles [79, 82]. Currently, the polarisation degree of freedom is most frequently used to achieve the high suppression of laser light larger than 6 oders of magnitude needed to observe resonance fluorescence. Our setup also employs polarisation filtering in conjunction with spatial filtering to observe resonance fluorescence. It is schematically sketched in Fig. 3.1.

A polarisation maintaining (pm) single mode fibre connected to a fibre collimator is used to allow for the easy and fast change between the various light sources during the experiments in a modular fashion. Furthermore, a fibre beamsplitter connected to the input fibre allows one to superimpose two lasers in the same spatial mode which is often required in experiments involving strict resonant excitation. A $\lambda/2$-plate is used to rotate the polarisation axis of the linearly polarised laser beam into the

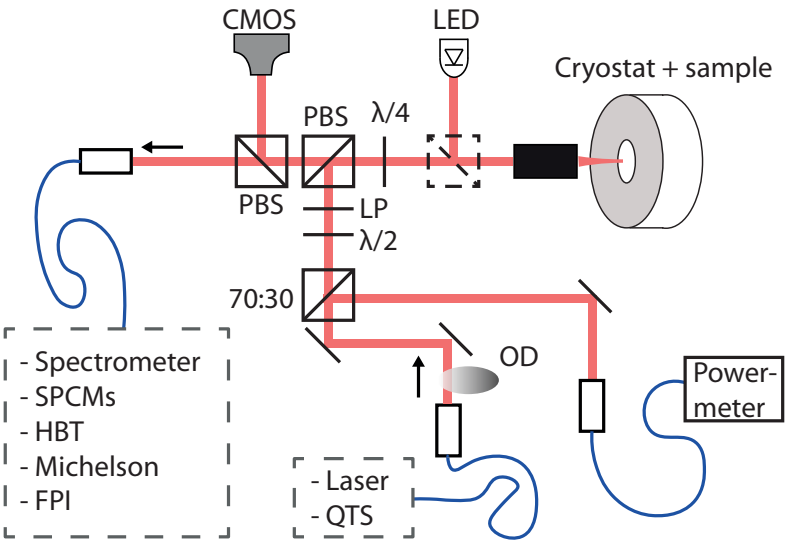

Figure 3.1: Sketch of the setup used for the experiments. LED -light emitting diode, LP - linear polariser, OD -optical density filter, PBS - polarising beam splitter, QTS - quasi thermal source

vertical direction. The beam then passes a linear polariser to further enhance its degree of polarisation before it is reflected by a polarising beam splitter (PBS) towards the microscope objective. We use an infinity-corrected objective with a numerical aperture (NA) of 0.65 (*Mitotoyu 50x Plan Apo NIR HR*) which is mounted on a closed-loop piezo cube (*PI Nanocube*) for fine adjustment of the objective position relative to the sample in all spatial dimensions. The piezo cube is fixed on a linear motor stage (*PI C843*) for coarse adjustment of the distance between sample and objective. The helium flow cryostat in which the sample is located is mounted on two linear motor stages for coarse displacement in the plane perpendicular to the excitation and detection beam path. A $\lambda/4$-plate between the polarising beam splitter and the microscope objective allows for the correction of effects of birefringence induced by the objective or the sample. The laser stray-light suppression is highly dependent on the orientation of the $\lambda/4$ plate and to a lesser degree on the orientation of the linear polariser. This is illustrated in Fig. 3.2 (c) and (d). Changing the orientation of the $\lambda/4$ plate by 25 mdeg reduces the suppression by one order of magnitude. It effectively allows one to change from a dark field to a bright field configuration. A second PBS in the beam path further filters vertical contributions so that effectively only horizontally polarised light reaches the single mode fibre. The successful suppression of laser light by more than 6 orders of magnitude in our experiments relies crucially on a confocal configuration. This can be understood by considering an image of the focal spot in the cross-polarised configuration displayed in Fig. 3.2 (b). Here, a characteristic clover shape is recognisable which is typical for this cross-polarisation detection scheme [83]. Although the laser is initially only vertically polarised, strong focusing of the beam leads to a considerable amount of intensity in the horizontal polarisation. This would be sufficient to make the detection of resonance fluorescence from a QD impossible. Thus, the core of the single mode fibre (diameter 5 μm) is placed right at the center of the clover in the image plane where hardly any residual laser photons are collected.

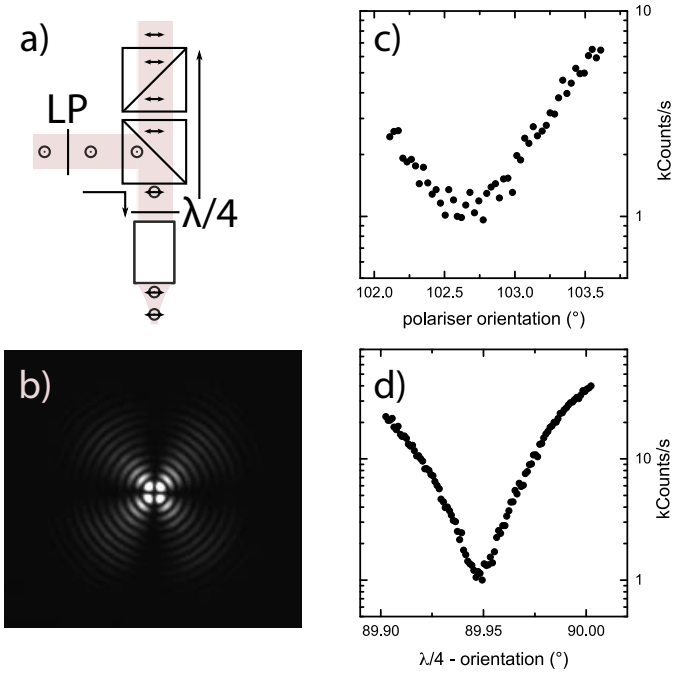

Figure 3.2: (a) Sketch illustrating the polarisation suppression scheme of the experimental setup (b) Image of the clover shaped focal spot observable in the dark field configuration of the microscope. (c) Dependence of the reflected laser intensity on the orientation of the linear polariser prior to the PBS in the exciting beam. (d) Dependence of the reflected laser intensity on the orientation of the quarter wave plate.

3.1.2 Photocurrent spectroscopy

Photocurrent spectrsocopy (PS) of a single QD was first demonstrated by Zrenner *et al.* [84]. A QD was embedded in the instrinsic region of a Schottky diode. Resonant excitation of the exciton transition results in the creation of an electron-hole pair in the QD. By application of a reverse bias the charge carriers tunnel from the QD and are detected as a change in the photocurrent. [84]. This technique has been widely used to address for instance the question of dephasing mechanisms in single QDs [85, 86]. Recently, it has also been successfully extended to the regime of cavity quantum electrodynamics (cQED) [87].

The advantage of this technique is an increased detection efficiency compared to conventional spectroscopy without the necessity of an elaborate stray light suppression [88]. On the other hand, it is more difficult to obtain information about the temporal evolution which typically requires pump-probe type experiments. Furthermore, it poses very stringent requirements to the sample processing and its quality as the electronic noise should be on the order of around 1 pA[1].

The optical setup used in our experiments is essentially the same setup used for the resonance fluorescence experiments however with additional equipment to measure the photocurrent. The photocurrent measuring circuit is shown in Fig. 3.3 (b). The bonded sample inside the cryostat is mounted on a chip carrier for electrical feedthrough which is itself fixed on a AlN platelet. We use a

[1]The maximum obtainable average photocurrent under pulsed excitation at a repetition rate of 80 MHz using a π-pulse is 12.8 pA.

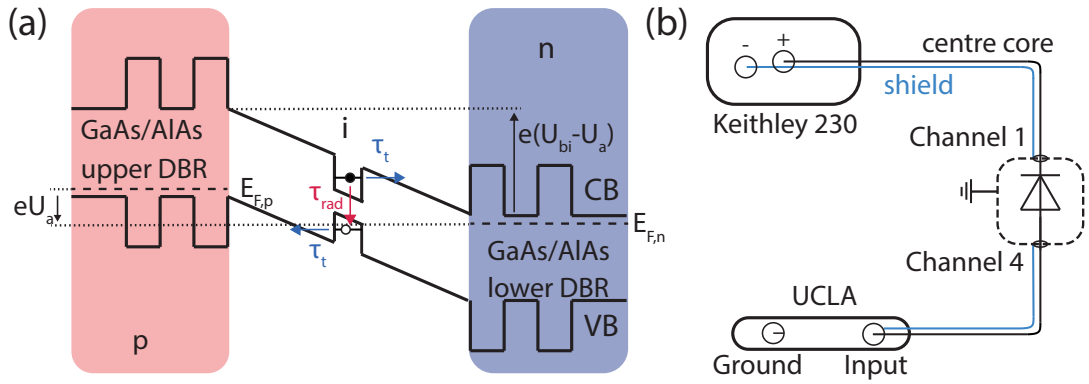

Figure 3.3: (a) Schematic showing the energy band diagram of a single QD photodiode with an applied reverse bias U_a. The electron and hole created by the resonant laser inside the QD can tunnel out and can be measured as a photocurrent. $E_{F,p(n)}$ is the Fermi energy in the p (n) doped region. (b) Sketch of the photocurrent measuring circuit. Blue lines represent the shield of the coaxial cables and black lines the inner core. The dashed box surrounding the QD photodiode is the cryostat which is connected to ground.

programmable voltage source (*Keithley 230*) to apply constant voltages to the sample and a custom-built analogue attoamperemeter (ultrastable low-noise current amplifier (ULCA)) to measure the current which was kindly provided to us by the Physikalisch-Technische Bundesanstalt [89, 90]. The ULCA effectively converts the measured current to an amplified voltage which is recorded by a data acquisition card (*NI PCIe-6321*). The circuit is connected to ground at the cryostat.

The sketch in Fig. 3.3 (a) illustrates the operational mode of photocurrent spectroscopy. The QD is located in the intrinsic region of a p-i-n diode. For our experiments, we use electrically contacted micropillar resonators [87, 91]. The built-in voltage U_{bi} of the diode which is equal to the potential across the depletion region in thermal equilibrium usually suffices in our samples for the ionisation and tunneling of charge carriers in the QD. In this manner, an exciton which is resonantly created within the QD can be electronically detected. The photocurrent is proportional to the average population of the exciton and the tunneling rate $1/\tau_t$. The tunnel rate can be altered by application of an additional external bias voltage U_a as U_a allows to set the width of the tunnel barrier. The tunneling rate $1/\tau_t$ as a function of the applied bias voltage can be calculated via an one-dimensional approximation according to [92]

$$\frac{1}{\tau_t} = \frac{\hbar\pi}{2m^* L^2} \exp\left(-\frac{4}{3\hbar e(U_{bi} - U_a)} \sqrt{2m^* E_{ion}^3}\right), \tag{3.1}$$

where m^* is the mass of the charge carrier, L the width of the confining potential and E_{ion} the ionisation energy. The total lifetime of the exciton at cryogenic temperature is given by [93]

$$\frac{1}{\tau} = \frac{1}{\tau_{rad}} + \frac{1}{\tau_t}, \tag{3.2}$$

which illustrates the competition between radiative and tunneling processes in the decay of the excitonic state.

3.2 Light sources

The groundbreaking experiments in early atomic physics which ushered in the development of quantum mechanics were conducted using high pressure lamps which are sources of thermal light. Today, virtually all experiments rely on lasers which act as coherent light sources and were first developed in the 60s of the 20th century. They provide light with almost perfect Poissonian statistics and very high frequency and phase stability. In fact, laser technology has reached such an astounding maturity and high degree of precision that laser frequencies derived from optical atomic clocks are stable to within a relative uncertainty of below 10^{-18} and are set to become the new time standard [94–97].

Lasers

Lasers provide highly directional, very intense and spectrally narrow light in conjunction with a stable intensity [98]. Lasers usually consist of three basic ingredients: a pump, a cavity and a gain medium. Depending on the specific gain medium, lasers are grouped in the following categories: gas, dye and solid state lasers. Basically all lasers used for quantum optical research are solid state lasers.

A diode laser (*Thorlabs CPS780S*) emitting at a fixed wavelength of 780 nm is used for the non-resonant above band gap excitation of the samples. Additionally, it is required as a weak background source in all experiments presented in this thesis involving the observation of resonance fluorescence of single-photon transitions. The phenomenon that RF from excitons can be gated by this additional laser has been investigated in some detail in literature [99, 100]. Most research explains the effect in the following way: Charge traps adjacent to the QD lead to strong spectral diffusion of the excitonic transition. The photocreation of charge carriers above the band-gap allows for the filling of charge traps thus stabilising the transition frequency [100, 101].

A pulsed laser diode (*PicoQuant LDH D-C-660*) emitting at 660 nm is used for experiments involving non-resonant excitation above the band gap.

For resonant excitation we use a *Toptica DLC CTL 950* which is a tunable, external cavity diode laser. It can be tuned from 915 to 985 nm using a mechanical motor while a piezo provides a fine tuning range of 72 GHz (294 μeV). The maximum achievable output power is around 80 mW. The linewidth is typically below 100 kHz measured over 50 μs. It is used for the resonant excitation of the QD excitons.

The Ti:Sa is a *Spectra Physics TsunamiHP fs 10 W* with a tuning range between 700 and 1080 nm. It is pumped by a cw diode laser (*Spectra Physics Millenia eV 10W*). Pulsed operation is achieved via passive mode-locking, typically giving pulses with a full width at half maximum of 2 ps. All lasers are fibre coupled.

Quasi-thermal light source

Most thermal sources are basically the opposite of lasers: they emit isotropically, they are spectrally broad and of limited spectral brightness. One possibility to circumvent these limitations however is to take a laser beam and specifically modulate its intensity. This preserves most of the previously mentioned laser characteristics whilst changing the photon statistics from Poissonian to thermal. One implementation of this idea was already established in the 1960's by Martienssen et al. [102, 103] . They took a focused laser beam and sent it through a rotating ground glass disk. Analysis of the transmitted light beam shows photon statistics very close to a thermal distribution [104]. Phenomenologically this can be understood as follows: The reflection of coherent light on a rough surface leads to many single independent waves with different phases being generated. If these waves are superimposed on a

image plane the different phases cause a spatially varying intensity distribution by interference. This interference pattern is commonly called a speckle pattern. Rotation of the ground glass then leads to a temporally changing speckle pattern. If the intensity in a small area is monitored in time, for example with a photodiode behind a pinhole, intensity fluctuations in time are observed. This random phase interference can also be described by a random walk of the electric field in the complex plane [104–106]. The corresponding intensity distribution is described by Boltzmann statistics

$$p(I) = \frac{1}{\langle I \rangle} e^{-\frac{I}{\langle I \rangle}}, \tag{3.3}$$

where $\langle I \rangle$ is the average intensity.

3.3 Detection of light

The experiments presented in this thesis can be grouped into 2 different categories depending on the studied properties: (i) spectral distribution of the emitted fluorescence in the steady state, (ii) time-correlated single-photon counting (TCSPC) experiments on the photon statistics of the emitted light field.

For the coarse spectral analysis of the emitted photons, we use a grating spectrometer (*Princenton Instruments SP2750*) with a focal length of 750 mm and 3 different gratings mounted on a turnable turret (300,1200 and 1500 grooves/mm). The maximum achievable resolution is approximately 25 μeV (6 GHz) at 930 nm. After the spectral decomposition by the grating, the light is focused onto a silicon charge coupled device (CCD) (*Princeton Instruments Pylon*) which is cooled to 153 K to reduce thermal noise [105].

In order to gain insights into the temporal or statistical properties of the light field emitted by the QDs, single-photon counting modules (SPCMs) are required whose temporal resolution is shorter than the lifetime of the QD. The standard SPCMs are avalanche photo diodes (APDs) whose active region typically consists of a silicon chip. Depending on the specific model used for the experiment, the temporal resolution ranges between 40-400 ps along with quantum efficiencies (typically) between 3-25 % in the near infrared at 900 nm. Usually, a trade-off between resolution and sensitivity has to be made as they scale inversely with the cross-section area of the diode. In contrast to APDs which don't need to be cooled, superconducting single-photon detectors (SSPDs) *Scontel* have to be cooled to below 2 K. The advantage of this increased experimental effort is however an increased quantum efficiency of about 85 % in combination with a temporal resolution of around 100 ps.

Besides the bandwidth of the photo detectors the dead time τ_{dead} is another important parameter. The dead time signifies the least time needed by the detector between two successive detection events in order to be able to record both of them. This seemingly technical side remark has important consequences for experiments with single-photon emitters. If the dead time is longer than the lifetime of the emitter T_1, i.e. $\tau_{\text{dead}} > T_1$, a single detector is not sufficient to record a intensity autocorrelation function $g^{(2)}(\tau)$ [107]. Since for typical APDs this dead time is between 50 and 100 ns (15 ns for the SSPDs), one needs to use a Hanbury-Brown and Twiss interferometer to measure intensity autocorrelation functions which will be discussed on the following section.

Interferometers

The Michelson interferometer certainly has a special place in physics as it was used to test the ether hypothesis in the late 19th century. More recently, it was also used for the first direct detection of gravitational waves [108]. Today, it is routinely used in optics laboratories to record the degree of first order coherence. In a Michelson interferometer, the light beam passes a beam splitter which splits the amplitudes in two equal parts. The two beams each impinge on movable retroreflectors which induces a parallel displacement of the reflected beam. The two reflected beams are superimposed on a beam splitter and directed towards a detector. The recording of a $g^{(1)}(\tau)$ is then conducted as follows. First, both arms are set to the same length and one retroreflector is moved on the scale of the wavelength of the light using a linear piezo actuator. Due to interference of the field amplitudes, the output intensity in the detection arm then varies sinusoidally as function of the displacement δx. The visibility of the observed oscillation is defined as

$$V = \frac{I_{\max} - I_{\min}}{I_{\max} + I_{\min}}. \tag{3.4}$$

This measurement is subsequently repeated for increasing path length differences Δx. Plotting the extracted visibilities over the time difference τ then yields the degree of first-order coherence.

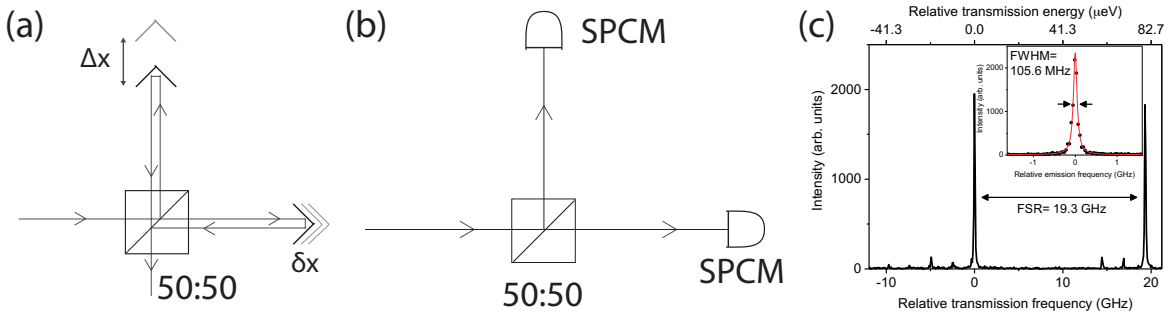

Figure 3.4: (a) Schematic of the Michelson interferometer. (b) Schematic of the Hanbury-Brown and Twiss interferometer. (c) Instrument response function of the Fabry-Perot interferometer. The Toptica CTL used to record the IRF has a linewidth below 10 kHz.

The same information i.e. the degree of first order coherence can obtained in the spectral domain using a Fabry-Perot interferometer . The scanning FPI used for our experiments is home built with a hemispheric geometry. It is controlled by a closed loop piezo element and provides a spectral resolution of 436.7 neV (105.6 MHz) and has a free spectral range of 79.8 μeV (19.3 GHz). Accordingly, the finesse is 183. It's instrument response function (IRF) is plotted in Fig. 3.4 (c).

The Hanbury-Brown and Twiss (HBT) interferometer has also had a considerable influence on physics and quantum optics in particular. The experiments revealed the importance of higher order coherences and enabled the first direct evidence for the quantisation of the electromagnetic field [32]. It consists of a simple 50:50 beamsplitter as well as two detectors, i.e. typically SPCMs. The central component is a counting electronics with the capability of time tagging, i.e. it records the detected counts and their respective arrival times. The time differences are binned and histogramed giving the degree of second-order coherence upon normalisation. In our TCSPC experiments, we either use a *PicoHarp 300* or a *qutau* counting module. For our experiments we use the following formula to

normalise the obtained experimental data $c(\tau)$

$$C_N(\tau) = \frac{c(\tau)}{N_1 N_2 w T} \tag{3.5}$$

where N_i are the count rates detected by SPCM i={1,2}, w is the widths of the bins and T is the total measurement time [109].

3.4 Sample fabrication

3.4.1 Epitaxial growth

The fabrication of the samples used in this thesis were grown via MBE (samples M2833-16.10 and M3569) or MOVPE (samples NP6303 and NP5647)[2]. Common to all these samples are the growth steps explained in the following. First, a buffer layer is grown to obtain a smoother sample surface with a thickness typically between 300-400 nm. This is followed by AlAs/GaAs mirror pairs of the lower distributed Bragg reflector (DBR). Since AlAs and GaAs have very similar lattice constants these structures can be grown lattice matched. Such backside DBR mirrors are found in virtually all QD devices in order to enhance the photon-extraction efficiency. An alternative approach consists in using gold mirrors instead of DBRs which offer the advantage that their reflectivity is less dependent on the wavelength and the angle of incidence [110]. Consecutively, a GaAs spacer layer of variable thickness is grown. Now the growth of the In(Ga)As layer starts which leads to the formation of the self-organised QDs in the SK growth mode. Due to the lattice constant mismatch of the two semiconductor materials the layered growth takes place in two dimensions until the critical thickness of a few monolayers is reached. At this point, the island growth begins. The morphological attributes of the QDs such as geometry, size and chemical composition and hence their optical properties can be influenced to a certain degree by the growth parameters. Finally, a GaAs capping layer is deposited on the active layer. During this growth step the island shape and composition can change dramatically due to surface exchange reactions and diffusion processes [111].

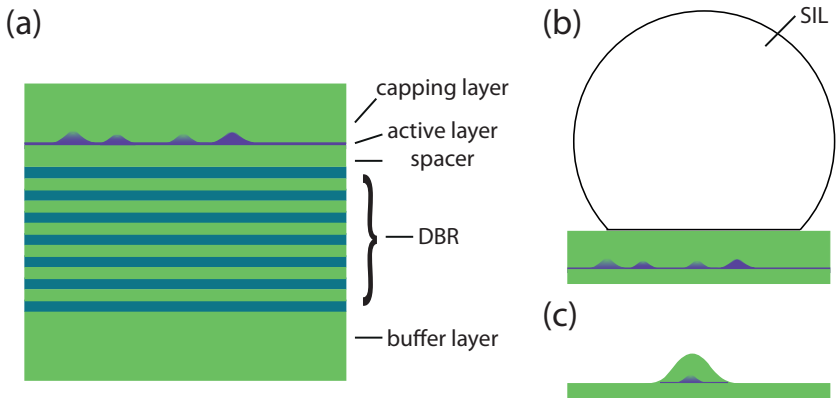

Figure 3.5: (a) Schematic of the typical lower sample structure described in the section 3.4.1. (b) Sketch of a solid immersion lens (SIL) (Weierstrass geometry) placed on the sample surface. . (c) Sketch of a deterministically fabricated mircolens which is situated around a preselected QD.

[2]The specific sample structures are listed in appendix 2.

3.4.2 Semiconductor microstructures

Since the QDs are embedded in GaAs which has a high refractive index of $n \approx 3.5$ only around 2 % of the photons emitted by the QD reach the objective lens in unprocessed samples. One strategy to tackle this problem is to engineer the local density of photonic states by the use of microcavities [112]. Such microcavities allow for a drastic increase in the photon extraction efficiency if the emitter is in resonance with the cavity mode. Micropillar cavities are certainly the most prominent example where extraction efficiencies as high as 66 % have been reported [11]. Moreover, micropillar cavities allow to access the strong coupling regime of cavity quantum electrodynamics [113].

For some applications such as the generation of polarisation entangled photon pairs from the biexciton cascade the broadband enhancement of the extraction efficiency is desirable. The most commonly used approach is the use of solid immersion lenses [114]. Further approaches consist in using waveguide structures or monolithic microlenses where extraction efficiencies of up to 29 % have been reported [115].

The fabrication of such microstructures requires additional processing steps after or in between growth steps. Typically, a electron beam sensitive resist is applied to the sample surface by spin coating in which the layout of the microstructure is subsequently written via high-resolution electron beam lithography. After development of the resist the unexposed parts of the resist are removed during the lift-off step using a solvent. Afterwards, the microstructures are excavated from the semiconductor material by reactive ion etching.

Science is the belief in the ignorance of experts.

Richard Feynman

4

Resonant spectroscopy of site-controlled quantum dots & photocurrent spectroscopy

In the first two chapters we introduced and discussed the theoretical, experimental and technological background for the studies which we will present in the following chapters. This chapter is devoted to the coherent spectroscopy of excitons in QDs, i.e. two-level systems. We begin this chapter by discussing resonance fluorescence from a site-controlled quantum dot (SCQD) realised by using the buried stressor growth technique. While this topic is somewhat more technologically motivated it also allows one to elucidate the basic phenomena of resonance fluorescence from a semiconductor QD. The most important results in this part have been published in Ref. [116]. Subsequently, we present experiments on photocurrent spectroscopy of single QDs. In these experiments, we observe pronounced light-matter and carrier-carrier interactions between the QDs and its solid state environment. Due to the creation of a hole gas in the vicinity of the QD we observe very asymmetric absorption lines in the spectra. The observation of Rabi oscillations in the photocurrent signal shows however that this effect does not preclude the coherent manipulation of this system. For all experiments presented in this thesis the samples were cooled to a temperature of 5 K unless it is stated differently.

4.1 Resonance fluorescence from site-controlled quantum dots

As was emphasised in the introduction, advances in the fabrication of quantum dot devices have established QDs as almost ideal two-level systems in the solid state. If, however, they are ever to become a scalable and reliably usable technological platform many obstacles are left to be overcome. The randomness regarding their spectral properties and spatial position represents certainly one of the biggest challenges. This randomness is of course rooted in the self-assembled growth process of semiconductor QDs via the SK mode(cf. chapter 2.6). This lead the community to direct a considerable amount of effort towards deterministic device fabrication. While the growth of a large number of QDs with an identical and predefined spectral position remains arguably close to impossible there exist today various different approaches to accomplish the site-controlled growth of QDs. One prominent approach is to pre-pattern the substrate by etching nanoholes or inverted pyramids [117–122]. During the consecutive overgrowth QDs preferentially nucleate aligned to these nanoholes. This method achieves a very high accuracy on the order of 10 nm with respect to the spatial position [118] but the

patterning typically diminishes the optical properties of the QDs in terms of quantum efficiency and emission linewidth by introducing defects in the substrate [123]. Another approach consists in growing QDs as embedded disks in nanowires [19, 124] which come with the built-in advantage of very high light extraction efficiencies [125, 126]. However, the proximity of the QD close to the surface of the nanowires (typical diameter on the order of 100-500 nm) leads to an enhanced spectral diffusion due to surface charge fluctuations.

In this context, we will introduce in the following section another site-controlled growth technique, i.e. the buried stressor growth technique which was developed at the Technische Universiät Berlin in recent years [127–129]. In section 4.1.2, we will evidence the successful growth of SCQDs by performing spatially resolved spectroscopy on the devices. Subsequently, by performing resonance fluorescence experiments we will see in section 4.1 that the SCQDs grown by the buried stressor growth technique possess promising optical properties.

4.1.1 Buried stressor growth technique

The basic idea behind the buried stressor growth technique is the lateral modulation of the strain field at the GaAs (001) growth surface by the use of selectively oxidised underlying AlAs layers. Nucleation of QDs during the subsequent growth then preferentially occurs at the regions of the highest tensile strain which is on top of the oxidised apertures. Hence, the SCQD are ideally located right in the middle on top of such apertures. In our case the final sample consists of several hundred square shaped mesas with a side length of about 20 μm. The aperture size is varied along the rows via a slight variation of the side length of the mesas. Figure 4.1 shows optical images of investigated mesas. In 4.1 (a) the aperture size was so large that a small spot is discernible in the middle of the mesa. For the mesa we studied in the following, which is depicted in Fig. 4.1 (b), this is not the case which suggests that the aperture is below the optical diffraction limit. The sample was grown and fabricated by Arsenty Kaganskiy and is a product of a elaborate technology process which is briefly explained in the following.

The SCQDs were grown by metal-organic vapour phase epitaxy using a n-doped GaAs substrate. The fabrication process starts by growing a template for the subsequent etching of mesa-structures and oxidation of the local apertures.

First, a DBR consisting of 27 pairs of $\lambda/4$ thick $Al_{0.9}Ga_{0.1}As$/GaAs layers is grown followed by a 30 nm thick AlAs layer which is embedded in 40 nm thick AlGaAs claddings. This initial growth step is followed by reactive ion etching in an inductively coupled plasma during which the 20-21 μm wide square shaped mesas are formed. The square shape is deliberately chosen as to minimise the formation of defects during the overgrowth of the structures. These defects tend to form faster on side walls in [110] and [1-10] direction. The etching removes the semiconductor material down to the last mirror pair and lays bare the AlAs layer which is required for the subsequent oxidation. The oxidation is performed at 420°C in a H_2O/N_2 atmosphere with the possibility to control the aperture diameter on the scale of a few hundred nanometres via in-situ optical monitoring of the oxidation process.

As mentioned briefly at the beginning of this section the site-controlled growth itself is achieved by the local modification of the free energy of a GaAs (001) surface using a spatially modulated strain field. This strain field is predominantly modified by the partial oxidation of the underlying AlAs layer. The most important parameter for enabling site-controlled growth of single QDs is here the diameter of the aperture. This dependency is illustrated by Fig. 4.2 (b). The surface strain is plotted for different aperture diameters as a function of the position on the mesa. It turns out that for aperture sizes of about 500 nm there is only one maximum of tensile strain right on top of the AlAs aperture.

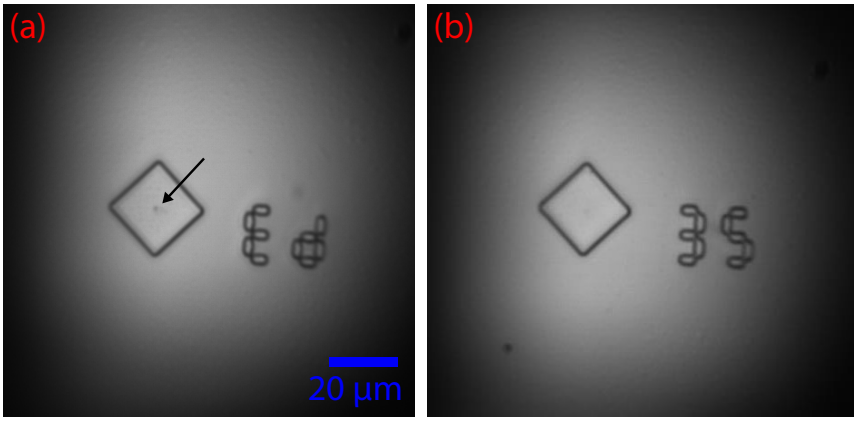

Figure 4.1: Optical image of the sample surface taken with the experimental setup presented in Fig. 3.1. (a) Mesa where the aperture (∅ ≈ 1300 nm) is larger and already visible (indicated by the arrow) on the surface. (b) Mesa used for the experiments. Here the aperture (∅ ≈ 700 nm) is not visible on the surface.

Subsequent growth of the strained InGaAs layer preferentially takes place at this maximum. Single QDs can accordingly be positioned in the middle of the mesa as is shown exemplary in an atomic force microscope (AFM) image in Fig. 4.2 (c). As can be seen there are two QDs positioned on the aperture with a diameter of approximately 700 nm. This diameter can also be regarded as an upper

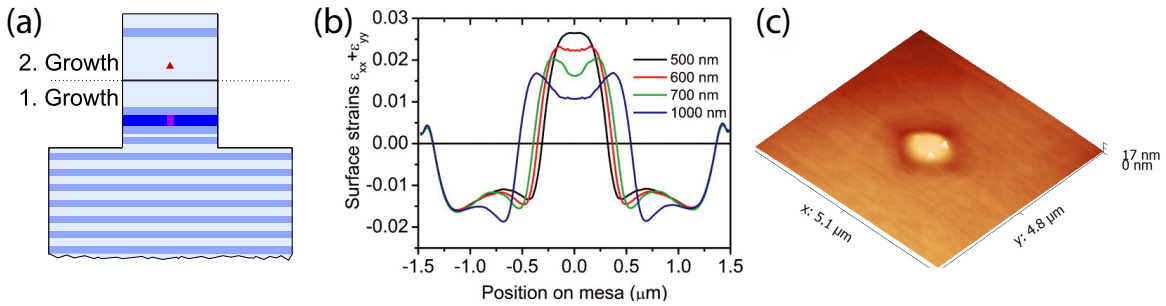

Figure 4.2: (a) Sketch of cross section of sample. The dark blue line represents the AlAs layer. The red shaded square represents the oxidised aperture and the red triangle the SCQD. (b) Calculated surface strain across mesa for different aperture radii. From [128]. (c) Atomic force microscope image of a mesa centre. Two QDs are visible on the edges of the overgrown aperture.

bound of the alignment accuracy of SCQDs in the centre of the large mesa structures. This accuracy is certainly lower than the 10 nm achieved for SCQDs based on nanohole arrays. Nevertheless it is well suited for the deterministic integration of QDs into resonant-cavity light emitting diodes and into micropillar cavities with a diameter of a few micrometers and a comparatively large lateral mode profile of several 100 nm. Furthermore, the buried stressor has the appealing prospect of scalability to larger wafer sizes as it is does not require delicate nanometre-scale processing which typically requires sequential processing.

4.1.2 Optical precharacterisation of the SCQDs

A statistical analysis of the success probability to achieve site-controlled growth using the buried stressor approach reveals a success rate of 65% [1] [130]. Thus the first step requires the identification of a mesa where the site-controlled growth was successful. To this end we perform a photoluminescence (PL) map scan of the mesa by raster scanning the piezo actuator on which the objective is mounted, effectively laterally displacing the focal spot across the relevant sample area of 25 x 25 μm. We use a non-resonant laser for excitation and detect the emitted photons with our spectrometer (cf. 3.1). The obtained PL intensity map is shown in Fig. 4.3 (a) where the spectra are integrated over a range of 6 nm (920 nm-926 nm). The spatial extent of the mesa can actually be well identified as photon emission into free space is increased due to lateral scattering along the edges. Furthermore, a bright emission spot can be identified close to the centre of the mesa. The spectra recorded at the location is depicted in Fig. 4.3 (c). We can observe a single bright emission line at around 923 nm along with two dimmer ones at lower energies. We perform a TCSPC experiment to measure the lifetime of the QD using a pulsed diode laser emitting at 660 nm with a pulse length of 40 ps as excitation source. Figure 4.3 (d) shows the recorded time trace of the PL from which we extract a natural lifetime of 898 ps. Power dependent measurements of the emitted intensity exhibit the typical dependency expected for a single excitonic complex in QDs, i.e. $I \propto P^1$ (cf. Fig. 4.3 (e)). From the same measurement we can extract the linewidth of the emission line as a function of excitation power. The data is plotted in Fig. 4.3 (f). For low excitation powers (<100 nW) the emission linewidth is limited by the resolution of our spectrometer (~ 25 μeV). For values exceeding 100 nW we observe a broadening which can be attributed to spectral diffusion due to increased charge carrier fluctuations [131, 132].

4.1.3 Cw resonance fluorescence from a SCQD

While non-resonant excitation of QDs allows for a reliable and basic characterisation of devices it has been shown that the emission properties of QDs are substantially enhanced under resonant excitation [13]. In non-resonant excitation schemes additional charge carriers are created in the vicinity of the QD which leads to significant spectral diffusion [133, 134]. Furthermore, carrier relaxation processes result in an additional broadening of the observed excitonic linewidths. Thus, in order to assess the underlying optical quality of the SCQDs more thoroughly we perform resonance fluorescence experiments. The first measurements consist in sweeping the laser across the resonance of the QD and collecting the scattered fluorescence photons on a SPCM. A typical scan at an excitation power of approximately 240 nW is displayed in Fig. 4.4 (a). We observe two Lorentzians which are separated by 18.5 μeV. The two lines correspond most likely to the finestructure splitting of the neutral exciton of the QD. Plotting the RF intensity as a function of excitation power we obtain the excitation power dependence depicted in Fig. 4.4 (c). The recorded data is well reproduced by the saturation behaviour expected for a TLS. We fit the data using equation 2.39 to which yields a saturation power of 89 nW. Another important figure of merit that can be drawn from this data is the linewidth for vanishing excitation power (cf. equation 2.41). From this limit it is possible to infer the dephasing time T_2. In our case this value is around 10 μeV which shows that there are fast dephasing processes such as charge fluctuations in our sample and the emitted photons are as a consequence about a factor of 13 above the fundamental

[1] This was determined by the ratio of (number of SCQDs)/(number of SCQDs+ number of randomly grown QDs) in an area of 5 μm x 5 μm. This value was determined via a statistical AFM analysis of 15 mesa structures of a reference sample processed in parallel with the sample used for the optical study.

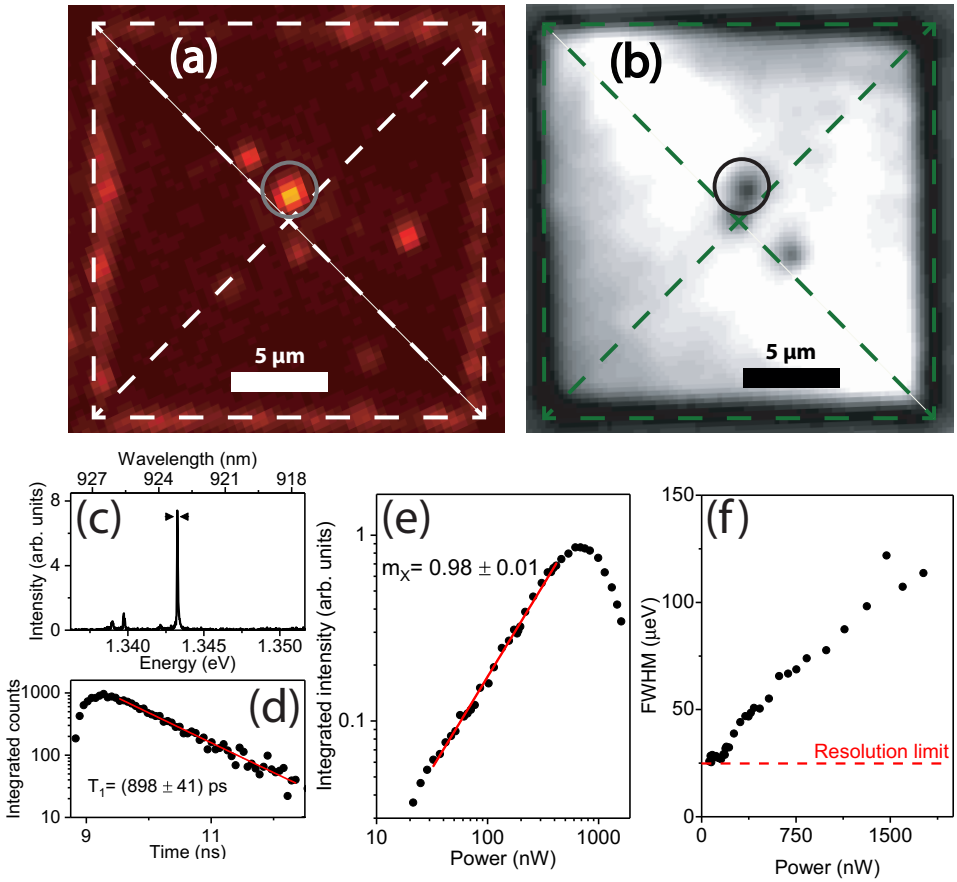

Figure 4.3: (a) Spatially resolved PL intensity map of a mesa containing a SCQD (indicated by the circle) very close to its centre. To obtain a scalar map the spectra are summed from 920 nm to 926 nm. (b) 2D cathodoluminescence intensity map of the same mesa. Here we sum the spectrum at each coordinate over the emission range of the wetting layer (895-915 nm). A dark spot (marked by a circle) at the centre indicates the aperture. (c) Non-resonantly excited μPL spectrum of the investigated QD. (d) TCSPC measurement of the QD PL under non-resonant pulsed excitation. (e) Integrated intensity as a function of excitation power. (f) Emission linewidth dependence on excitation power under non-resonant excitation.

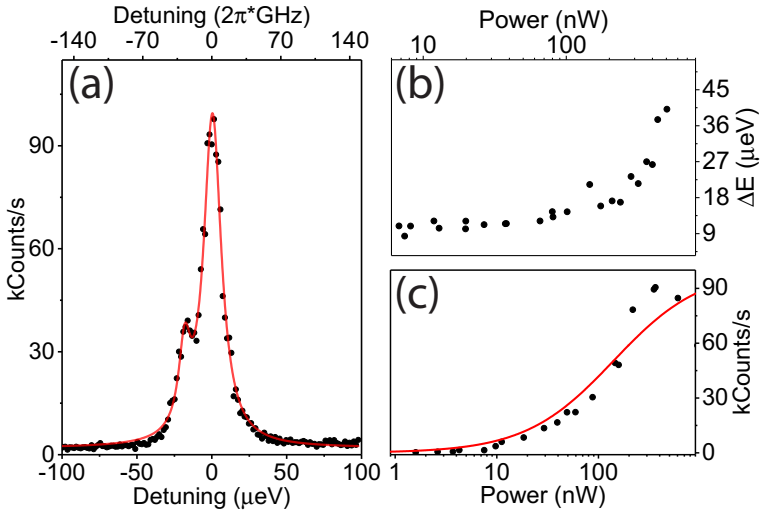

Figure 4.4: (a)Resonance scan across the exciton transition. The double peak is probably due to a finestructure splitting of 18.5 μeV. (b) Linewidth of excitonic component at $\nu = 0$ as a function of excitation power. The minimum observed linewidth is on the order of 10 μeV. (c) RF signal on resonance as a function of excitation power. Equation 2.39 is fit to the data.

radiative limit. For SCQDs, this Fourier limit has not been reached yet with the smallest reported linewidths being 3.6 μeV [135]. Fourier-limited photons are required for many schemes in photonic quantum communication technology, such as the quantum repeater, as the indistinguishability depends crucially on it [133]. Currently, there are two different approaches to obtain Fourier-limited photons from semiconductor QDs. The first one applies CQED effects to reduce the radiative lifetime T_1 of the emitter below half the dephasing time in the device. This is typically achieved by tuning the QD in resonance with a cavity mode where the reduction of the lifetime is given by the Purcell factor of the mode [11, 134]. The second approach employs external electric fields to stabilise the charge fluctuations in the vicinity of the QD [136].

After this basic characterisation where we analysed the steady-state response of the QD to a cw laser we now look at coherent phenomena in the light-matter interaction. First, we observe the Mollow triplet to evidence the coherent interaction between the resonant light field and the exciton. A typical emission spectrum under strong driving at 260 μW is displayed in Fig. 4.5 (a) where the fit function consists of three independent Lorenztians. The ratio of the central peak area and sideband area is around 3:1, i.e. larger than the value of 2:1 expected from theory [137]. This discrepancy is most likely due to imperfect laser suppression and pure dephasing [62]. By detuning the laser relative to the transition frequency we detect the typical dispersive behaviour associated with the Mollow triplet (cf. inset in Fig. 4.5 (a)). Evidently, the intensities of the sidebands also change with detuning. For negative detunings the higher energy sideband is brighter while for positive detunings the lower energy sideband is brighter. This phenomenon is a further evidence of the influence of pure dephasing in our device.[2] Plotting the spectrum as a function of the power of the incident laser, we obtain the data presented in Fig. 4.5 (b). The splitting between the sidebands and central peak increases linearly with the square root of the power as is expected from theory [55]. The slope of the increase of the Rabi splitting with the amplitude of the electric field is $(5.12 \pm 0.04)\ \mu\text{eV}/\sqrt{\mu\text{W}}$ and $(4.78 \pm 0.02)\ \mu\text{eV}/\sqrt{\mu\text{W}}$ for the higher and lower energetic sideband, respectively. This value which is mainly influenced by the light-matter

[2] In the case of radiative limited dephasing the intensity of both sidebands should be equal regardless of the detuning.

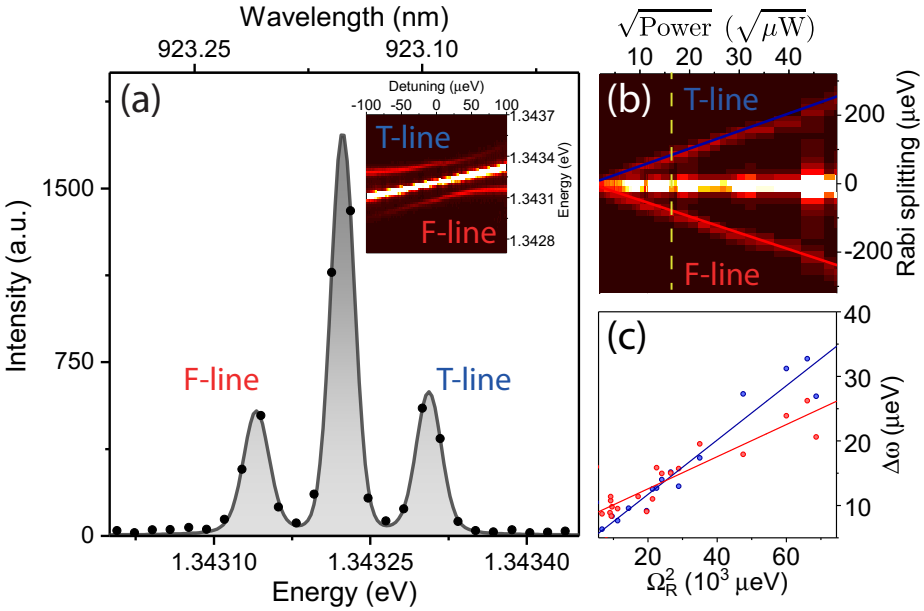

Figure 4.5: (a) Emission spectrum of the target QD at an excitation power of 260 μW (indicated by the dashed vertical line in (b). The inset visualises the dispersive behaviour of the Mollow triplet. (b) Emission spectrum as a function of excitation power. The Rabi splitting increases linearly with a slope of 5.1 (-4.8) $\mu eV/\sqrt{\mu W}$. (c) Blue (red) dots: linewidth (FWHM) of the T(F)-line as a function of excitation power. A linear function $\Delta\omega \propto \chi\Omega_R^2$ is fit to the data giving a slope of χ = 0.42(0.26).

coupling strength is very similar to values reported for SCQDs (5.04 μeV/$\sqrt{\mu W}$ [123]) and standard QDs (5.4 μeV/$\sqrt{\mu W}$ [59]) in planar samples.

On a quick glance, the observed behaviour has so far experimentally reproduced the theory of a TLS coupled to the vacuum of the electromagnetic field presented in chapter 2. Since QDs are not isolated TLSs but embedded in a solid-state matrix traces of the interaction between QD and their solid-state environment can also be found in the photons emitted by them. Inspection of equation 2.52 reveals that the linewidth of the components of the Mollow triplet depends on T_1 and T_2. Several experimental studies reported a broadening of the sidebands as a function of excitation power [60, 138]. The sidebands lend themselves particularly well for these measurements as they are spectrally well separable from the laser. Since T_1 can safely assumed to be independent of the excitation power in most experiments the culprit for the observed broadening necessarily needs to be an excitation dependent dephasing. The observed effect could be well reproduced with different theoretical approaches incorporating an exciton-phonon interaction and has generally become known as excitation induced dephasing (EID) [138, 139]. This mechanism could also successfully explain the damping of Rabi oscillations observed in pulsed photocurrent experiments [85, 86].

When we briefly discussed the TLS in chapter 2.4.1 the master equation (cf. equation 2.36) contained the term $\frac{\Gamma_2}{2} D[\sigma_{11} - \sigma_{22}]$ which captures pure dephasing effects, i.e. effects that lead to a decay of the coherences but preserve the populations of the TLS. This is of course a very crude approximation as it assumes the decay rate to be constant and furnishes no information on the physical mechanism responsible for this decay only that the reservoir it couples to is Markovian. As described above phonons have been identified to be the major source of dephasing in QDs. Phenomenologically, the excitation of an electron from the conduction to the valence band leads to a change of the charge

configuration of the semiconductor crystals. Consequently, the equilibrium positions of the lattice ions are modified effectively resulting in a local variation of the band structure and as a consequence in a coupling between excitons and phonons. This coupling mechanism is known as deformation potential interaction which is by far the most dominant coupling mechanism in QDs at low temperatures[3]. The phonon spectral density which characterises the exciton-phonon coupling is given for longitudinal acoustic (LA) phonons by

$$J_{\mathrm{ph}}(\omega) = \omega^3 \frac{(D_e - D_h)^2}{4\pi^2 \eta u^5} e^{(-\frac{\omega^2 d^2}{2u^2})} \tag{4.1}$$

$$= \alpha \omega^3 e^{-\frac{\omega^2}{\omega_c^2}}. \tag{4.2}$$

Here, D_e and D_h denote the bulk electron and hole deformation potential constants. d is the dot dimension, u the speed of sound in the material and η the sample density. Evidently, the spectral density increases towards the cut-off frequency $\omega_c = \frac{u}{d}$. This signifies that for Rabi frequencies Ω approaching ω_c the coupling between exciton and phonons is increased which results in a larger dephasing in the system [141]. Cut-off frequencies in InGaAs QDs are typically of 1 meV and are larger for smaller QD dimensions. To account for EID we rewrite the dephasing rate more accurately as

$$\Gamma_2 = \frac{1}{2}\Gamma_1 + \gamma_{\mathrm{PD}} + \gamma_0 \tag{4.3}$$

where γ_{PD} is the phonon-induced pure dephasing and γ_0 non-phonon induced dephasing. The exact expression for γ_{PD} can be derived from a weakly-coupled master equation [60]. Under the assumption that $\Omega < k_B T, \omega_c$ it can be shown that

$$\gamma_{\mathrm{PD}} = \pi \alpha k_B T \Omega^2. \tag{4.4}$$

Here α is a measure of the exciton-phonon coupling strength which is defined though the phonon spectral density $J_{\mathrm{ph}}(\omega)$. The FWHM of the sidebands is thus determined by

$$\Delta\omega = \frac{3}{2}\Gamma_1 + \gamma_{PD} + \gamma_0. \tag{4.5}$$

We extract the linewidths of the sidebands from the previous measurement and plot the power dependent broadening of the sidebands as a function of the squared Rabi splitting in Fig 4.5 (c). In accordance with equation 4.4 we observe a linear increase for both sidebands albeit with slightly different slopes of 0.42 for the high energy sideband and 0.26 for the low energy sideband. From equation 4.5 we can also deduce also a non-phonon induced dephasing rate of $\gamma_0 = (6.0 \pm 1.3)\ \mu$eV ($T_1 = \frac{1}{\Gamma 1} = (898 \pm 41)$ ps, $\gamma_{PD} = 0$ for $\Omega = 0$). This value is smaller than values of 30 μeV reported for SCQD achieved via alignment to etched nanoholes [123] but considerably larger than values of 0.56 μeV reported for self-assembled QDs [60].

4.1.4 Pulsed resonance fluorescence from a SCQD

After having explored the dephasing mechanisms of the SCQDs we now investigate their potential to act as single-photon emitters. To this end we perform pulsed resonance fluorescence experiments. First,

[3] Other coupling mechanisms are the piezoelectric electron-acoustic phonon coupling and the electron-optical phonon Fröhlich interaction [140]

we perform power dependent measurements to observe Rabi oscillations. We observe damped Rabi oscillations to about pulse areas corresponding to 2π[4]. For higher pulse areas the laser background becomes too strong to faithfully evaluate the data. The observed damping of the oscillations is again due to the coupling to LA phonons [142]. From these measurements we can also infer the power corresponding to a π-pulse which allows for the (almost) deterministic generation of an exciton in the QD. In this case this is achieved for 1.1 μW. Interestingly, we also observe a considerable amount of power dependent linewidth broadening in this experiment. The extracted linewidths as a function of the square root of the power are plotted in Fig. 4.6 (b). The linewidth increases linearly with the square root of the power up to the power corresponding to a π-pulse. Here the linewidth stays more or less constant at a width of about 62 μeV. The mechanism responsible for the observed broadening is probably also EID as discussed in the previous section. Curious is however the observed stagnation of broadening for pulse areas from 1 to 2 π.

The final experiment consists in measuring the intensity autocorrelation function of the emitted light field. The obtained data is shown in Fig. 4.6 (d). The reduced area of the peak at zero time delay with $g^{(2)<0}$ compared to the adjacent peaks indicates that we indeed observe only a single two-level system. Double sided exponential decays are fit to each peak and convolved with a Gaussian to account for the limited temporal resolution of the used SPCMs (τ_{res}= 350 ps). From this analysis we extract $g^{(2)}(0) = 0.12$ which is well below 0.5 but also significantly above commonly reported values of 0.01 and below [11, 12, 134, 144]. The non-ideal value is most probably due to residual, uncorrelated scattered laser photons as is illustrated by the spectra displayed in Fig. 4.6 (c) and (d). The spectrum in (c) corresponds to the excitation conditions of the $g^{(2)}(\tau)$ function. Plotting the spectrum with a logarithmic y-scale reveals the reflected laser pulse. This can however be remedied for example by the implementation of pulse shaping techniques for the excitation pulse as well as spectral filtering of the emission by a Fabry-Perot cavity [145]. Furthermore, a reduction of the laser spot size at the QD position by the use of a higher NA objective or by placing a solid immersion lens on top of the mesa [114] might further reduce the power required to create an inversion in the QD.

[4]This is probably due to the strong wavelength dependence of the utilised zero order quarter wave plate in our setup. For experiments involving pulsed excitation, it is probably advantageous to utilise linear polarisers for achieving polarisation suppression as their performance is less wavelength dependent.

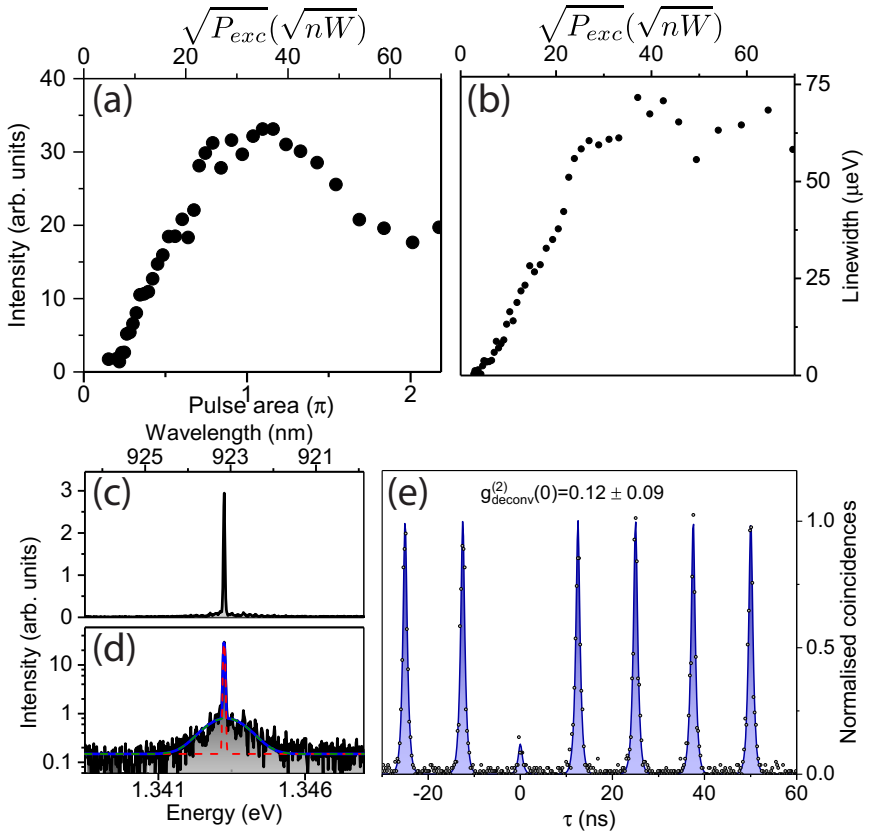

Figure 4.6: (a) Power series under pulsed excitation revealing Rabi oscillations as a function of the pulse area. The excitation power required for the maximum inversion of the population of the QD (π-pulse) is 1.1 μW. (b) Linewidth of the emission spectrum as a function of the power. The data is extracted from the same measurement as in (a). Each spectrum is fitted with a Voigt profile where the Gaussian contribution is used to account for the IRF of the spectrometer. (c) Emission spectrum under excitation of an pulse area of 0.9 π (=0.89 μW). (d) Semi-logarithmic representation of the data in (c). Below the emission line of the QD (red dashed line) the exciting pulse is still visible (green dashed line). (e) Second- order correlation function under pulsed excitation with an intensity of 0.9 π. The reduced peak area at τ=0 with $g^{(2)}_{\text{deconv}} < 0.5$ is indicative of single-photon emission [4, 143].

4.2 Photocurrent spectroscopy of quantum dot micropillars

Apart from the coherent spectroscopy of QDs via resonance fluorescence encountered in the preceding section their solid-state nature also allows for coherent spectroscopy via photocurrent spectroscopy. In this section we will briefly discuss experiments that we conducted using QDs embedded in electrically contacted micropillars [146]. The samples used for these experiments were grown and processed at the Technische Physik Würzburg. The lower and upper DBR consist of 27 and 23 mirror pairs, respectively. The active QD ($In_{0.6}Ga_{0.4}As$) layer is centred inside a λ cavity at the antinode of the electric field. The p (n) doping is gradually decreased within the DBR towards the cavity from the top (bottom) of the pillar for an optimised ratio of low absorption and low resistivity [91, 147]. A cross-sectional scanning electron microscope (SEM) image of an fully processed image is depicted in Fig. 4.7 (a). From these wafers micropillar cavities were patterned using electron beam lithography and reactive ion plasma etching. For electrical contacting the sample is in a subsequent step planarised using a polymer (benzocyclobutene, BCB). Finally, a second electron-beam lithography is used to pattern a ring-shaped Au p contacts around the upper facet of the micropillars. This approach allows for current injection without degrading the optical access along the cavity axis. The direction of propagation of the incident laser photons is of particular importance in experiments with such micropillar cavities as the optical density of states is greatly reduced by the cavity along the direction of its axis [87, 148]. In our experiments, we excite the sample from the top, i.e. along the cavity axis. This leads to most photons whose frequency does not match the resonance frequency of the cavity being reflected.

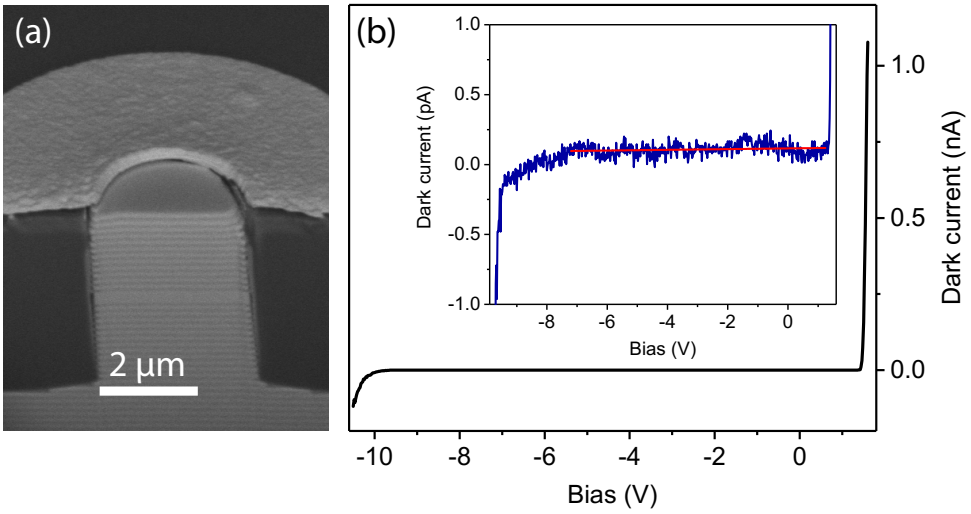

Figure 4.7: (a) Cross-sectional SEM image of an electrically contacted micropillar. Image courtesy of Tobias Heindel. (b) I/V curve of an electrically contacted micropillar showing the expected diode characteristic. Inset: Magnification of the reverse bias region showing a dark current below 0.2 pA in our sample.

As mentioned in section 3.1.2 photocurrent spectroscopy of single QDs requires high quality samples with very little electronic noise in order to be able to detect the photocurrent by the creation of single excitons in the QD. A typical dark-current I/V curve recorded without any laser irradiation of the sample is shown in Fig. 4.7 (b). In reverse direction the dark current is below 0.2 pA over a broad range of about 8 V with a very small gradient. This data demonstrates the very high quality and close to ideal pn-diode behaviour of the sample and allows for the photocurrent spectroscopy of single QDs.

4.2.1 Photocurrent spectroscopy of single QDs

A laser scan of a single QD at an excitation power of 9.3 μW is plotted in Fig. 4.8 (a). Scanning the laser emission energy from lower to higher value (forward direction) we observe that the line shape is far from Lorentzian as would be expected for a single TLS and exhibits a strong asymmetry (black curve). On the low energy side of the peak the slope increases gradually until the maximum where the current rapidly drops off. Interestingly, this effect also exhibits a hysteresis depending on the scan direction of the laser frequency: By tuning the laser frequency from higher to lower values (backward direction), we obtain the red curve. Evidently, the maximum photocurrent is less than half the value obtained for the forward scan direction and the linewidth is also greatly reduced (141 μeV compared to 92 μeV).

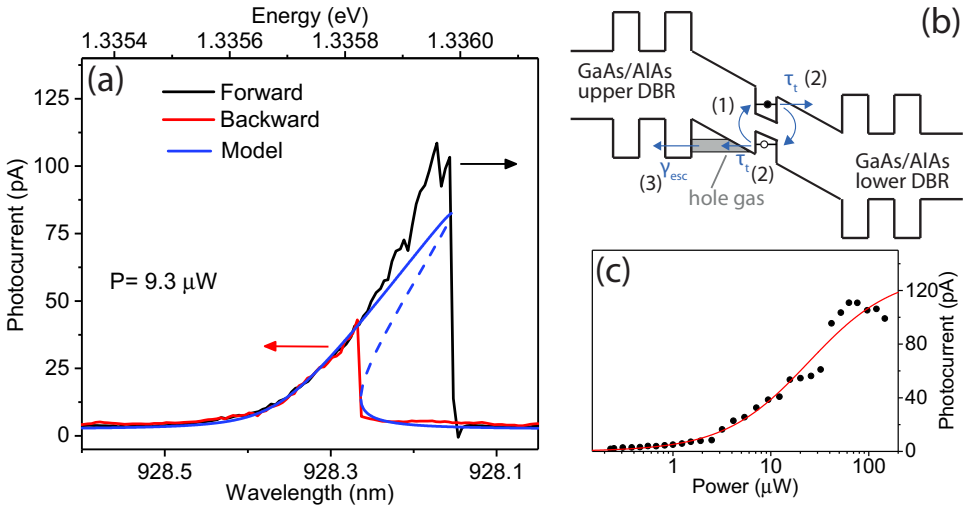

Figure 4.8: (a) Photocurrent spectrum of a single QD at an excitation power of 9.3 μW. Black (Red) solid line: Photocurrent spectrum obtained when the laser is scanned across the transition from lower (higher) to higher (lower) energies. The hysteresis is well accounted for by a stationary solution to equation 4.6 represented by the blue line. (b) Schematic depicting the creation of the hole gas at the interface of the upper DBR. (c) Saturation behaviour of the detected photocurrent. A fit of equation 2.39 to the data yields a saturation power of $P_{\mathrm{sat}} = (24 \pm 3)\ \mu$W.

A similar effect has been reported recently in resonance fluorescence and reflectivity experiments [149, 150]. In the following we will briefly outline the interpretation of the hysteresis effect put forward by Merkel *et al.* in reference [150]. The underlying mechanism can be divided into three distinct steps and is illustrated in Fig. 4.8 (b). (1) Optical excitation leads to the creation of excitons in the QD. The excitons can either recombine radiatively or electron and hole can tunnel to the respective back contact with the rate τ_t (cf. section 3.1.2) (2) Tunnelled holes can get trapped at the AlAs interface (in our case the upper DBR) where a 2D hole gas is formed. (3) The hole gas slowly decays with the tunnel rate γ_{esc}. The draining of this hole gas depends on its population n_h. n_h is in turn via process (2) dependent on the creation efficiency of excitons in the dot. This process can account for the observed lineshape as well as hysteresis: On the low energy side of the resonance, the creation of excitons in the dot will lead to the formation of the hole gas. The hole gas leads to a blue-shift of the exciton resonance due to the Coulomb interaction. This blueshift leads to reduced generation rate of excitons in the QD which in turn entails a reduction of the hole gas population n_h. Consequently, the resonance is red-shifted again towards the laser. Evidently, the formation of this hole gas effectively acts as a negative feedback loop

for negative detunings. The rate equation model for the hole gas population n_h which accounts for the observed effects is given by [150]

$$\dot{n}_h = \gamma_{pump} - \gamma_{leak} = \gamma_{abs}\tau_t L(n_h) - \gamma_{esc} n_h \,, \tag{4.6}$$

where

$$L(n_h) = \frac{(\Gamma/2)^2}{(\nu_l - \nu_0 - \delta\nu(n_h))^2 + (\Gamma/2)^2}. \tag{4.7}$$

Here, Γ is the linewidth of the transition, $\nu_{0(l)}$ the transition (laser) frequency, γ_{abs} the absorption rate and $\delta\nu(n_h) = \delta\nu^{1h}\, n_h$ is the shift of the resonance due to the electric field change induced by to the hole gas. This model is valid in the low excitation regime where the hole tunnelling rate τ_t can be assumed to be constant. Importantly, it reproduces the observed bistability observed in our system. We plot a numerical stationary solution (blue curve) superimposed on the experimental data in Fig. 4.8 (a). The dashed part of the curve corresponds to the unstable solution of equation 4.6. According to this model, the strength of the hysteresis is determined by the ratio $\delta\nu_{\max}/\Gamma$. Here, the maximum frequency shift $\delta\nu_{\max}$ due to the hole gas is given by $\delta\nu_{\max} = \delta\nu^{1h}\tau_t\gamma_{abs}/\gamma_{esc}$. By performing power dependent measurements we recover a saturation behaviour typical for a TLS as is shown in Fig. 4.8 (c). From a fit of equation 2.39 to the data we obtain a saturation power of $P_{\text{sat}} = (24 \pm 3)\,\mu$W. This very large value (compared for example to the 90 nW in the section 4.1) can be attributed to the fact that the QD is spectrally far detuned off the cavity resonance, i.e. most of the laser intensity is reflected by the upper DBR [87].

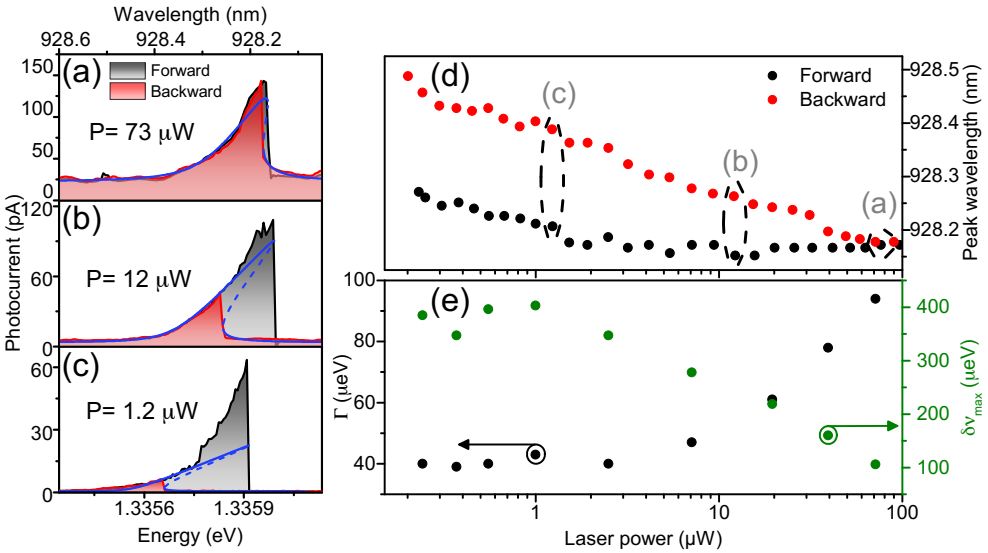

Figure 4.9: (a)-(c) Photocurrent spectra of a single QD at an excitation power of 73 μW, 12 μW and 1.2 μW, respectively. Black (Red) solid line: Photocurrent spectra obtained in forward (backward) laser scan direction. The hysteresis is well accounted for by a stationary solution to equation 4.6 represented by the blue line. (d) Black dots: Wavelength of the maximum photocurrent signal in forward (backward) laser scan direction as a function of excitation power. (e) Linewidth an maximum hysteresis as a function of excitation power extracted from solutions of equation 4.6 to the experimental data.

Interestingly, we observed in these saturation measurements that the hysteresis actually decreases with increasing excitation power and even almost vanishes above saturation. Figure 4.9 (d) shows the extracted peak maxima as a function of excitation power. Exemplary, we plot in Fig. 4.9 (a)-(c) the photocurrent spectra for three different excitation powers illustrating the decreasing hysteresis. We observe that in addition to the decrease of the fold-over region, the linewidth in the backward scan also increases. While not explicitly included in the model, the latter effect is the typical power broadening of the absorption linewidth in a TLS discussed in section 2.4. In Fig. 4.9 (e) we plot the extracted linewidths Γ and maximum frequency shifts $\delta\nu_{\max}$ obtained from solutions of equation 4.6 to the experimental data. The simulation has five free parameters and the extracted values are therefore only to be regarded as a indicator for the observed trend. It is however evident that in addition to the observed power broadening of the linewidth the maximum frequency shift $\delta\nu_{\max}$ also decreases by a factor of 4 over the observed power range which suggests a power dependence of at least one of the parameters $\tau_t, \gamma_{abs}, \gamma_{esc}$.

In order to fully elucidate the observed effects, independent measurements of the parameters are required. For example, one could saturate the hole gas by applying a weak, non-resonant laser similar to experiments in resonance fluorescence. The photocurrent induced by the resonant laser could then be separated from the non-resonant contribution using a lock-in technique. Such a measurement can serve to unambiguously determine the linewidth Γ and its power dependence in these experiments.

4.2.2 Photocurrent spectroscopy in the regime of cQED

A typical photocurrent spectrum of a micropillar with a diameter of 1.7 μm under cw excitation at 350 nW is shown in 4.10. We can observe two single, asymmetric QD lines whose asymmetry we discussed in the previous section. The Lorentzian shaped cavity mode at 925 nm is most prominent at this excitation power. This is the fundamental HE_{11} mode with a Q factor of 8700 which we extract from the spectrum. The possibility to observe the photocurrent of a photonic mode can be attributed mostly to two effects. Firstly, there can be QDs in the active layer close to the cavity resonance which we are unable to observe in PS [151]. Secondly, coupling to QDs via non-resonant inverse cavity feeding effects mediated by phonons also enable the detection of cavity modes in the photocurrent [152–154].

By using the temperature or the applied electric field as a parameter we can also tune the QDs through the cavity which is illustrated by a PC temperature series in Fig. 4.10 (b) [(c)] where we scan the laser in the backward [forward]direction. The QDs shift through the cavity with the resonance temperature being at around 35 K for QD1 and 37 K for QD2. Interestingly, we observe an increase in the detected photocurrent when QD and cavity are in resonance which is typical in PL experiments. In PL experiments, this increase is caused by the reduced radiative life time of the QD due to the Purcell effect. A reduction of the radiative life time should actually cause a drop in the photocurrent on resonance which has been observed in PC experiments when exciting the micropillar from the side [87]. The increase we observe is due to the more efficient coupling of laser light into the cavity at resonance which overcompensates the loss in PC due to the Purcell effect. Thus, by tuning the QD into the cavity we perform again a power series as in the previous section.

Similarly, we also observe a reduction of the hysteresis when tuning the QD into the cavity resonance which we plot in 4.11. In addition to the reduction of the hysteresis due the increased pump light intensity a Purcell-effect induced reduction of the radiative life time could be also responsible for the observed effect. In order to clarify the contribution of the reduced radiative lifetime to the observed reduction in hysteresis the experiment could be performed under side-excitation where the intensity at

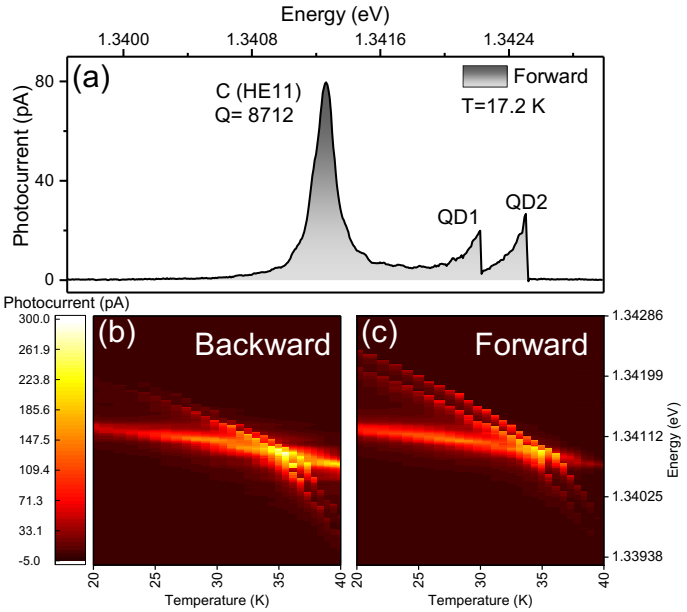

Figure 4.10: (a) Photocurrent spectrum of an electrically contacted micropillar. The fundamental (HE11) cavity mode C is dominating the spectrum while two QDs are visible far off resonance. (b) Temperature dependent PC scan of the micropillar resonator in backward laser scan direction. The QDs are tuned into resonance around 36 K. (c) Temperature dependent PC scan of the same micropillar resonator in forward laser scan direction.

the QD would be constant irrespective of the detuning from the cavity.

4.2.3 Coherent phenomena in photocurrent spectroscopy

Obviously, under cw excitation there are clear deviations between the QDs in our sample and an ideal TLS due to the strong interaction with the solid-state environment. It is therefore interesting to investigate whether it is nevertheless possible to observe coherent phenomena in our system. We use the Ti:Sa to resonantly excite a QD with pulses of 2 ps pulse length. Recording the photocurrent as a function of excitation power yields the data plotted in Fig. 4.12 (a).

For large excitation powers we observe a linear increase in the photocurrent. This background is typical for photocurrent measurements and attributed to absorption from other nearby QDs in the sample. At low powers, we observe deviations from the linear increase. By subtracting the linear increase from the data and plotting the subtracted data as a function of the square root of the excitation power we obtain Fig. 4.12 (b). We observe heavily damped Rabi oscillations to about pulse areas corresponding to $2\,\pi$. It is thus possible to evidence coherent light-matter interaction in the sample using photocurrent spectroscopy despite the hole-gas interaction discussed in the previous section.

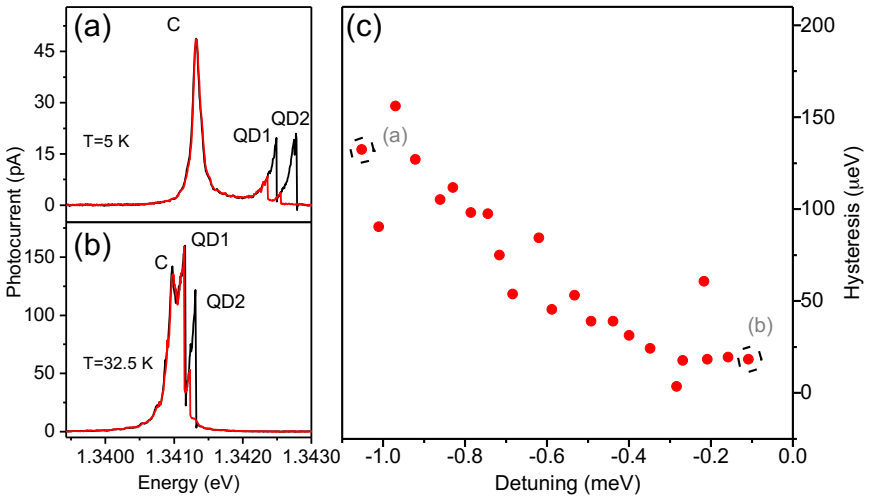

Figure 4.11: (a) Black (Red) line: Photocurrent spectrum of the micropillar at 5 K in forward (backward) laser scan direction. A clear hysteresis is discernible for both QDs. (b) Black (Red) line: Photocurrent spectrum of the micropillar at 32.5 K in forward (backward) laser scan direction. The hysteresis of QD1 has almost vanished close to the cavity resonance. (c) Hysteresis of QD1 as a function of detuning from the fundamental cavity resonance.

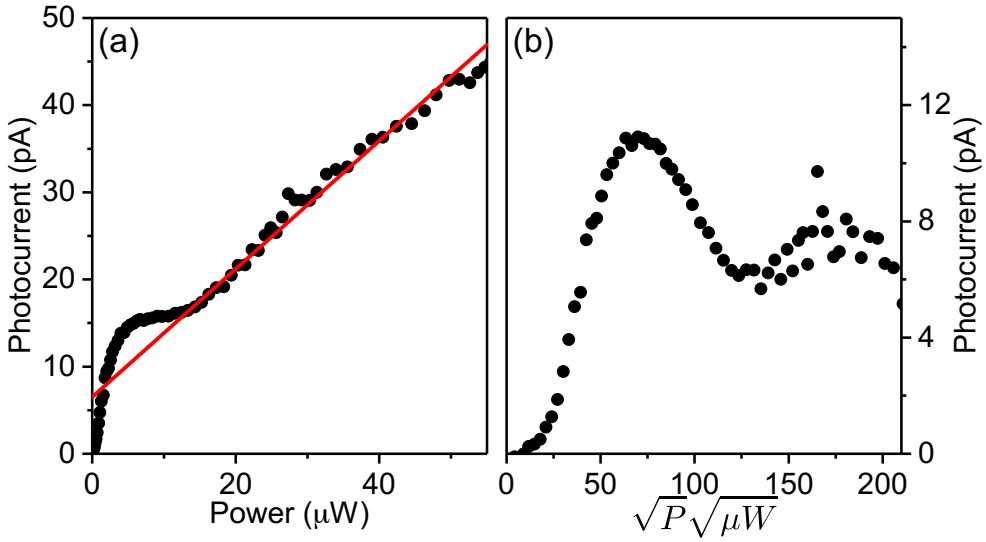

Figure 4.12: Rabi oscillation measurement in the photocurrent. (a) Raw data from the measurement. The red line represents a linear fit which is caused by background photocurrent. (b) Data after subtraction of the linear background plotted over the square root of the excitation power.

4.3 Summary of chapter 4

This chapter presented studies on single QDs which were less concerned with fundamental studies but were more technologically motivated. First, we presented standard resonance fluorescence experiments performed on site-controlled QDs to assess their optical quality. We showed that the approach using the buried-stressor growth technique achieves site-controlled growth without greatly compromising the optical quality of the QDs. The integration of these SCQDs in pin structures has already been successfully demonstrated [129] and might allow for a reduction of the dephasing via Coulomb blockade [136]. Thus, the SCQD grown via a buried-stressor might also serve as a deterministic source of indistinguishable photons in the future.

In the last section of this chapter we presented experiments on the coherent spectroscopy of single QDs via measurement of the photocurrent. Here, we observed asymmetric line shapes and a hysteresis effect which are qualitatively well accounted for by a model which suggests the formation of a hole-gas in the proximity of the QD. We also investigated the influence of a cavity on the observed hysteresis effect by tuning the QD into resonance. We measured a reduction of the hysteresis towards the resonance of the cavity which is however attributable to the increased field strength of the electric field in resonance. In order to observe a reduction of the hysteresis due to the Purcell effect it will be interesting in the future to use a side-excitation scheme to circumvent the spectral filter properties of the cavity in axial direction.

Das Wesentliche an jeder Erfindung tut der Zufall, aber den meisten Menschen begegnet dieser Zufall nicht.

Friedrich Nietzsche

5

Wigner time delay & photon-statistics excitation spectroscopy

In this chapter, the focus is shifted towards more fundamental studies of the physics of a TLS interacting with a resonant light field. First, we examine the Wigner time delay induced by a single QD which is an effect observable in the low excitation regime of resonance fluorescence where the TLS behaves very much like a classical oscillator. More precisely, a low-intensity wave packet resonantly scattered by a TLS experiences a phase shift that leads to a temporal delay between the exciting and scattered pulse. For purely coherent scattering this time delay was predicted by Wigner in 1955. We show that in solid-state systems the presence of pure dephasing leads to additional incoherent scattering and thus clear deviations from Wigner's theory. These results have been published in Ref. [155].

Subsequently, we explore the influence of the photon statistics of the exciting light field on the response of a single TLS. We contrast the influence of thermal with coherent excitation on different phenomena such as Rabi oscillations, the Mollow triplet and the photon statistics of the emitted light field. With these experiments, which have been published in Ref. [156],we demonstrate that a QD can act as very sensitive probe to the photon-number fluctuations present in a light field.

5.1 Wigner time delay induced by a single quantum dot

In the previous chapter, we have seen that a lot of effort is required to obtain high quality samples which allow for QDs with good optical qualities and to achieve even Fourier-limited photons is considerably more challenging. However, it is a curious fact that coherently scattered photons, i.e. photons emitted by a TLS under very low optical excitation ($s \ll 1$) have properties which are independent of the dephasing properties of the TLS. This regime is also sometimes referred to as Heitler regime, as the δ-like spectrum of a TLS in this regime was first calculated by Heitler [157]. In the experiment, of course, the spectrum always has a finite width as phase fluctuations leads to a finite correlation time i.e. bandwidth of the exciting light field [34, 158]. It was however demonstrated that the photons coherently scattered by a TLS have a first-order coherence almost identical to the exciting laser field while possessing the second-order coherence of the TLS [47, 58, 159]. This intriguing property has motivated further research on photons emitted in the Heitler regime. In particular, it was shown that these photons are indeed phase-locked to the exciting field [22, 160–162].

In the limit of low excitation, the TLS responds linearly to the incoming light field like a classical oscillator. The associated dispersive behaviour gives rise to the phase of the emitted photons. As in the case of the classical oscillator, this phase depends on the detuning between the laser frequency and the transition frequency of the TLS. The associated phase lag between exciting and emitted photons has been directly observed for atoms and QDs [28, 53]. Interestingly, this phase lag gives rise to another phenomenon which is called Wigner time delay. This term refers to the time delay between exciting and scattered pulse observable in the low excitation regime. This effect can also be understood in the framework of Fourier analysis. Multiplying a pulse in the spectral domain with a constant phase leads to a temporal shift of the pulse in the temporal domain upon Fourier transformation. This has already been studied for single single atoms where the maximum time delay is given by twice the radiative lifetime [163]. In systems with pure dephasing processes such as our QD devices the maximum delay is given by the decoherence time T_2.

The sample (M3569) used for this experiment are self-assembled InGaAs QDs which emit between 918 and 930 nm and were grown by MBE at the Technische Physik Würzburg. The QDs are embedded in a planar low-Q DBR cavity consisting of 24 lower and five upper mirror pairs. In this particular sample, naturally occurring micron-sized photonic defects on the surface of the sample enhance the photon extraction efficiency [164].

5.1.1 Optical pre-characterisation of the QD

Figure 5.1 shows the basic RF characterisation of the QD which we used to study the Wigner time delay. The measurements aim in particular to determine the T_1 and T_2 times of the exciton transition. The laser scan across resonance in Fig. 5.1 (a) is fit by a single Lorentzian which suggests that the transition is most likely a trion. On resonance, we detect a maximum photon flux of $1.36\,x\,10^6$ photons/s on the SPCM. The saturation power P_{sat} which we obtain from fitting the data using equation 2.39 is 40.8 nW. From these measurements we also extract the absorption linewidths. We fit equation 2.41 to the data which yields a minimum observable linewidth at vanishing power of $(3 \pm 0.1)\,\mu$eV (cf. power series Fig. 5.1 (b)). According to equation 2.41, this value corresponds to a T_2 time of (445 ± 16) ps. From an intensity autocorrelation measurement well below saturation (P=0.07 P_{sat}) which is displayed in Fig. 5.1 (d) we extract a lifetime of the excited state of $T_1 = 750 \pm 150$ ps. Thus, from these experiments we can conclude that the photons emitted from our QD are about a factor of 3.3 above the Fourier limit.

This is also confirmed by recording the emission spectrum of the QD well below saturation where part of the total intensity is coherently scattered. As we have seen in section 2.4.2 the emission spectrum of the coherently scattered photons in resonance fluorescence is given by the excitation source, i.e. the spectral properties of the laser. In the absence of pure dephasing processes the measurement of the emission spectrum at low excitation powers should thus simply yield the IRF of the FPI as the linewidth of the laser is below 10 kHz and thus 4 orders of magnitude smaller than the FWHM of the FPI [159]. In our case however, even far below saturation we still record a single peaked spectrum with a FWHM of 0.84 μeV. This is due to the fact that in our system the maximal fraction of coherently scattered photons is given by $T_2/(2T_1)$=450 ps/1500 ps$\approx$ 0.3. Accordingly, we always find the properties of the TLS in the emission spectrum since the incoherent part is at least three time as large as the coherent part and masks the coherent response of the system (cf. section 2.4.1).

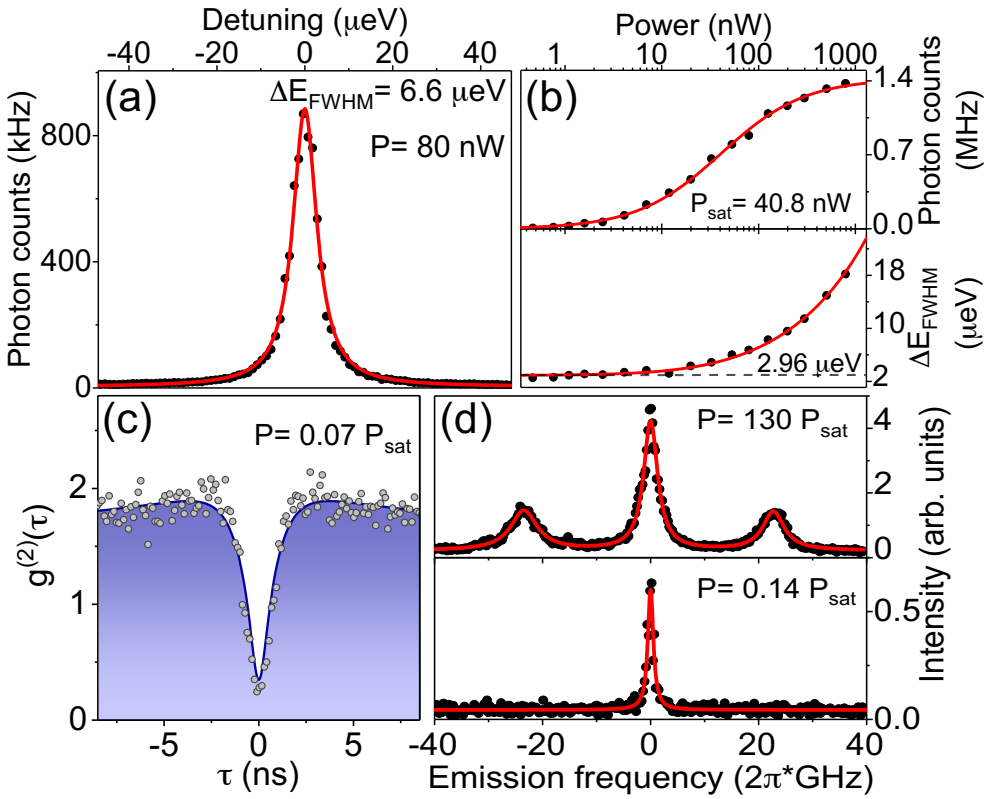

Figure 5.1: (a) Resonance scan of the trion transition. (b) Upper panel: scattered intensity on resonance as a function of excitation power. Lower panel: linewidth as a function of excitation power. (c) Intensity autocorrelation measurement of the RF signal at an excitation power of 2.9 nW yielding $g^{(2)}_{\mathrm{deconv}}(0) = 0 + 0.03$. (d) Upper (lower) panel: High resolution emission spectrum above (below) saturation.

5.1.2 Wigner time delay

After having determined the optical properties of the QD, we now want to explore the Wigner time delay induced by this single QD. We saw in section 2.4.1 that the phase lag induced by a TLS in the steady-state is given by

$$\phi = \arctan \frac{\mathrm{Im}(\rho_{01}^{\mathrm{st}})}{\mathrm{Re}(\rho_{01}^{\mathrm{st}})} = \arctan(T_2\Delta) + \frac{\pi}{2}\,. \tag{5.1}$$

This phase lag gives rise to the Wigner time delay which can be calculated to be [163]

$$\tau(\Delta) = \frac{d\phi}{d\omega} = \frac{T_2}{1 + (\Delta T_2)^2} \tag{5.2}$$

in systems with pure dephasing. Thus, in a solid-state system the maximally observable time delay (at $\Delta = 0$) is given by the decoherence time T_2 present in the system. Furthermore, we see that in theory the time delay depends on the detuning Δ via a Lorentzian function with a FWHM of $\frac{2}{T_2}$. We want to point out that this derivation only describes the temporal delay of the coherent fraction of the RF signal. Since the presence of pure dephasing in a TLS invariably entails the generation of incoherently scattered photons [1], it is clear that we will not directly recover this dependence in our experiments when detecting the entire light emitted by the TLS.

While this derivation assumed a cw excitation the only way to measure this time delay in the experiment is to use pulsed excitation. There are evidently two requirements that need to be fulfilled to observe the effect. First, the pulses obviously need to be of low power and secondly, the pulses need to be sufficiently longer than the lifetime of the emitter, i.e. the atomic dipole needs to reach a steady-state [165]. If the pulses are too short, i.e. spectrally broad, different spectral parts of the pulse will pick up a different phase from the TLS and thus a distortion of the pulses may occur.

We use an electro-optic modulator (EOM) (*Jenoptik amplitude modulator am905*) driven by a pulse generator custom-built by *PicoQuant* to shape Gaussian pulses with a FWHM of $\Delta t = 1.05\,\mathrm{ns}$[2]. The combined timing resolution of the used SPCM and time-tagging electronics is $\Delta\tau_{FWHM} = 388\,\mathrm{ps}$. Evidently, we only obtain a pulse that is around 1.4 times longer than the lifetime of the QD thus not quite fulfilling the aforementioned requirements. The resonant laser pulse reflected of the sample surface is recorded with the quarter waveplate deadjusted from the dark-field configuration. Setting the waveplate to the dark-field configuration allows us to only record the photons scattered by the TLS. In Fig. 5.2 (a) we plot the reflected laser pulse and photon wave packet scattered by the QD under a slight detuning of $\Delta = 0.5\,\mu\mathrm{eV}$ which are normalised for a better comparability. The response of the TLS is delayed with respect to the laser pulse as expected. Likewise, we plot the scattered pulses for two additional detunings in Fig. 5.2 (b). We determine the centre of the pulses by fitting a Gaussian to the central area of the experimental data. As predicted by equation 5.2 the temporal delay decreases with increasing detuning. Apart from the delay there is however also a visible pulse distortion from the original Gaussian pulse shape which is particularly marked for the pulse close to resonance ($\Delta = 0.5\,\mu\mathrm{eV}$). To understand the origin of the distortion we simulate the experiment using the optical Bloch equations (cf. equations 2.37) with a time dependent driving term $\Omega(t) = \sqrt{I/I_{\mathrm{sat}}}\exp(-\frac{t\sqrt{8\log(2)}}{(4\Delta t)})^2$. In the simulation, which is shown along the experimental data in Fig. 5.2 (c), all parameters apart from a scaling factor (which is

[1] The maximally coherently scattered fraction is given by $\frac{T_2}{2T_1}$ (cf. section 2.4.2).

[2] This is the maximum pulse length obtainable from the pulse generators available to us with an amplitude output of at least 0·6 V.

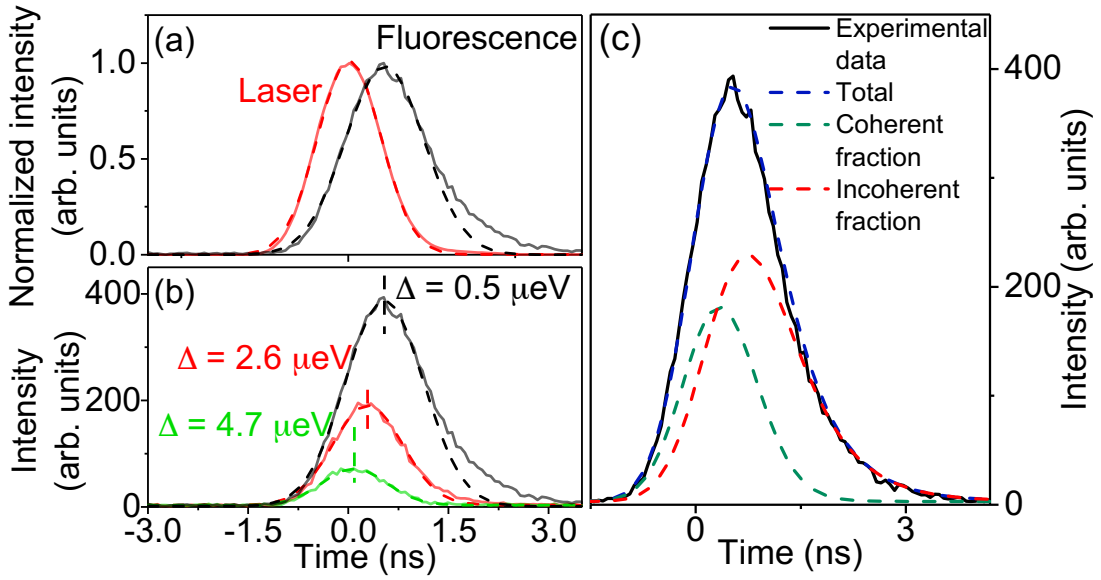

Figure 5.2: (a) Red solid line: Laser pulse reflected off the sample surface which is used to excite the QD. The pulse has a FWHM of 1.05 ns. Black solid line: maximally delayed fluorescence signal close to resonance. (b) Fluorescence pulses emitted for different relative detunings between laser and TLS. The dashed lines are Gaussian fits to the central part of the data.(c) Black solid line: Experimentally detected pulse for $\Delta = 0.5\,\mu$eV. Blue dashed line: Simulation of the fluorescence signal. The green and red lines represent the coherent and incoherent fraction, respectively.

used to convert occupation of the excited state to a fluorescence signal) are fixed to the values obtained from the experiments in the previous section. The total fluorescence emitted by the QD is proportional to the population of the excited state and $I_{\mathrm{tot}} \propto \rho_{11}(t)$ and reproduces well the experimental data. Furthermore, we can calculate the coherent ($I_{\mathrm{coh}} \propto |\rho_{01}|^2$) and incoherent contribution to the total fluorescence ($\mathrm{I}_{\mathrm{incoh}} \propto I_{\mathrm{tot}} - I_{\mathrm{coh}}$). Evidently, the deviations from the Gaussian pulse shape at the falling edge are due to incoherent scattering while the rising edge of the pulse consists predominantly of coherent scattering. This is a consequence of the underlying Bloch equations: At first, coherence must be built up before the coherence drives a population transfer to the excited state.

Next, we want to experimentally reproduce the dependence predicted by equation 5.2. To this end we recorded the scattered pulse during 2 minutes for each frequency step. In this way we scan the laser across the resonance as is illustrated in the inset in Fig. 5.3 which shows the integrated intensity of the scattered pulse for each measurement. The experimental data is well reproduced by the simulation.

In Fig. 5.3, the centre of the scattered pulses is plotted as a function of detuning. Evidently, the pulse delay is maximal on resonance in accordance with equation 5.2 and decreases with increasing detuning. We measure a maximum retardation of (528 ± 6) ps close to resonance ($\Delta = 0.5\,\mu eV$). This is well above the delay of 445 ps predicted by equation 5.2. As mentioned above, this is attributed to the large fraction of incoherently scattered photons which lags behind the coherently scattered photons. This lag of the incoherent fraction leads to the larger temporal shift of the total fluorescence with respect to the coherent fraction. Interestingly, the pure dephasing also leads to a finite, non-zero temporal delay off resonance which is not the case for systems without pure dephasing. While the simulation correctly reproduces the time delay close to resonance the delays measured off resonance are up to 150 ps smaller

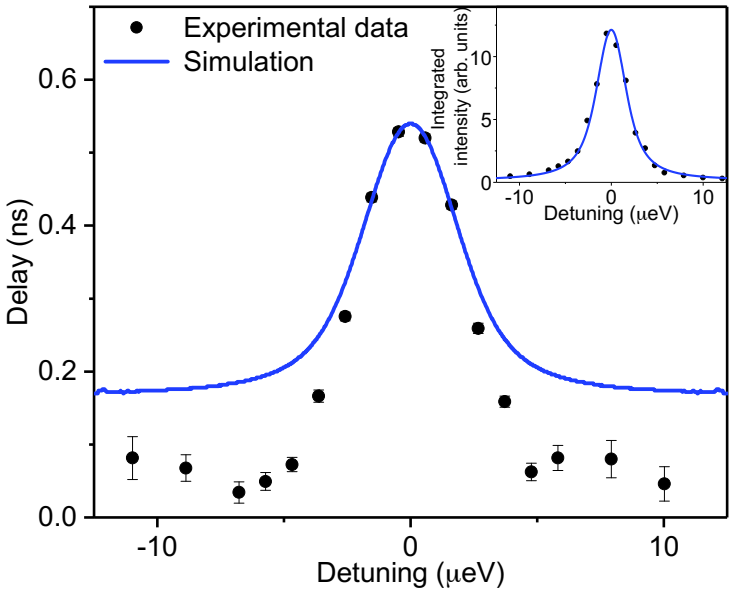

Figure 5.3: Wigner time delay induced by a single InGaAs QD as a function of detuning. Close to resonance ($\Delta = 0.5\,\mu eV$), the maximum observed delay is 530 ps. Inset: Integrated intensity of the scattered pulse as a function of detuning. The blue solid lines are the result of the simulation of the experiment as described in the main text.

than the values obtained from the simulations. A more precise knowledge and modelling of the pure dephasing processes could lead to an increased agreement between simulation and experiment.

Despite these ambiguous results these measurements allow for an indirect and easy measurement of the phase lag induced by a TLS in a system with considerable pure dephasing.

5.2 Exciting a quantum dot with thermal light

The previous experiments have mostly reproduced the expected and well-known textbook results where the light field is treated as a classical monochromatic plane wave (cf. chapter 2.4). This of course due to the fact that lasers well above the threshold emit light with properties astoundingly close to this ideal. In particular, the integration times during the experiments are sufficiently long so that the average photon numbers $\langle \hat{n} \rangle$ are so large that the relative uncertainties δn become negligible, i.e. the Rabi frequency can be regarded as fixed. Nevertheless, several investigations, theoretical as well as experimental [25, 166–169], have shown that the response of a TLS depends very sensitively on the photon statistics of the exciting light field. The most prominent example of this being, perhaps, the revival of Rabi oscillations observable for coherent fields with low average photon number $\langle \hat{n} \rangle$ [170]. Interestingly, while the excitation of a TLS with non-classical light fields such as single-photon states has been experimentally explored before [22, 171] the excitation of a TLS with thermal radiation has not been the subject of experimental studies [3]. In the following section, we will contrast the influence of thermal and Poissonian photon statistics on the response of an exciton in a QD. First, we will present some of the early theoretical predictions dating back to the 1970's which we intend to verify with our experiments. In the same section the theoretical model used for simulating the conducted experiments

[3] Remarkably people skipped this topic and investigated this influence on a hugely more complex system, namely living cells [172].

is treated. Then we will briefly introduce the properties of our thermal light source, a home built Martienssen lamp. The experiments themselves will show that thermal light is less efficient at exciting a single-photon transition than light exhibiting Poissonian photon statistics. Furthermore, we will observe that coherent phenomena such as Rabi oscillations and the Mollow triplet disappear under thermal excitation and that the light emitted by a TLS remains non-classical irrespective of the exciting photon statistics. Finally, we will show that thermal light can be used to excite a two-photon transition, e.g. the biexciton, more efficiently than it is possible with coherent light.

5.2.1 Theoretical predictions and modelling

The first lasers employed for spectroscopy suffered still from considerable phase and intensity fluctuations. Theoreticians therefore started in the 1970's almost simultaneous to the first experiments with lasers and atoms to investigate the influence of several parameters of the laser light, such as the bandwidth or photon statistics, on the optical response of atoms, i.e. two-level systems. For instance, the groups of Peter Zoller and Claude Cohen-Tannoudji explored in their work the influence of the photon statistics on the emission spectrum of a TLS [166, 168]. The relevant graphs from the respective publications are displayed in Fig. 5.4. Evidently, they both predict a disappearance of the Mollow sidebands under thermal excitation. Cohen-Tannoudji and coworkers conclude:

"Due to the large dispersion of the amplitude of the light electric field, the three peak structure in the fluorescence spectrum which appeared when a laser beam of very well defined amplitude was used for the excitation, is now completely washed out in this limiting case. The disappearance of the three-peak structure clearly shows the sensitivity of the fluorescence spectrum to higher order correlation functions of the light electric field." [166].

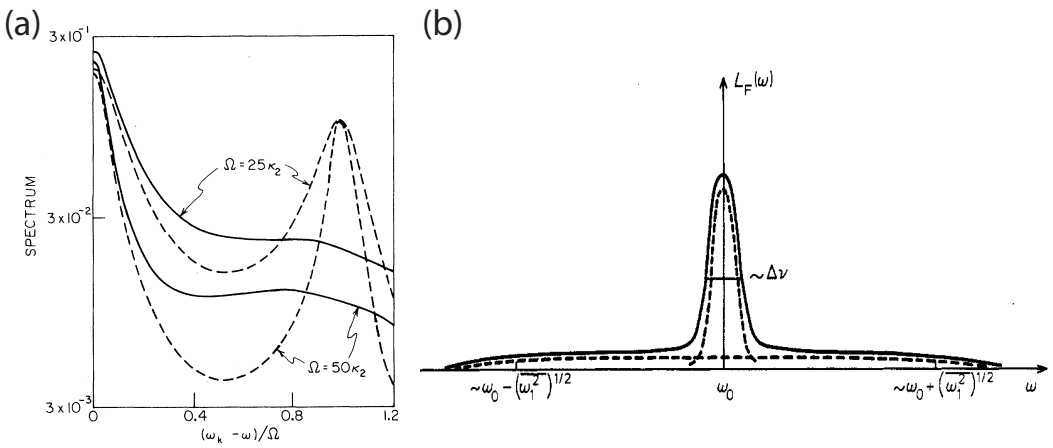

Figure 5.4: (a) Solid (Dashed) line: Theoretical prediction of the emission spectrum of a TLS under thermal (coherent) excitation for two different average Rabi frequencies. From [168]. (b) Emission spectrum of a TLS excited by an intense Gaussian thermal field of spectral width $\Delta\nu$. From [166].

The group around Peter Zoller arrives at the same prediction but they also show that in the steady-state regime the excitation of a TLS with thermal light is less efficient than with coherent light, stating: "This means that the chaotic field is less effective than the coherent field in saturating a one-photon transition." [168].

Researchers in the group of Peter Knight also looked into the dynamic evolution of a TLS under thermal light. They found that the Rabi oscillations which are observable under coherent excitation are washed out under thermal excitation [167].

In 1979, Schubert and coworkers theoretically investigated the influence of thermal excitation on the photon statistics of the light field emitted by the TLS and compare it to excitation by a laser [169]. For both excitation schemes they predict an antibunching for time scales that are short compared to the lifetime of the emitter T_1. On intermediate time scales however they derive that excitation by a thermal light source leads to bunching effects (i.e. $g^{(2)}(\tau) = 2$) in the fluorescence of the TLS.

Besides single-photon transitions, the influence of photon statistics on multi-photon transitions has also been addressed in various works. In particular, Carmele et al. calculated that the biexciton of a QD is more efficiently excitable using thermal compared to coherent light [173].

From the preceding discussion it is clear that thermal light more or less destroys all the characteristic quantum features that one usually works so hard to observe in the lab. Nevertheless we believe that the following experiments are very instructive for illustrating some fundamental concepts. In particular, these experiments show once more that not only intensity, first order coherence and frequency are crucial parameters for optics experiments but also photon statistics, i.e. second-order coherence of the excitation light.

For simulating the experiments involving the coherent excitation we use the semi-classical theory presented in chapter 2.4. This adoption is warranted as for the experiments involving steady-state solutions, such as the Mollow triplet, the photon numbers during the interaction time are so large that the Rabi frequency can be regarded as constant and the occurring relative photon-number fluctuations are negligible. For example, at an excitation power of 100 nW and a radiative lifetime of about 1 ns, we estimate $\langle \hat{n} \rangle$=460 and $\delta n = 4.7\,x\,10^{-2}$. For experiments in the transient regime the question is more delicate. Here, we operate at an excitation power of at least 1 μW where around 180 photons arrive at the sample during 40 ps which is the temporal resolution of the SPCMs which yielding a relative uncertainty δn of roughly 7 percent. However, the central part of the experiment takes place after the Rabi frequency has reached a constant value, i.e. after the rise time of the pulse (200 ps). By then at least 900 photon have arrived at the sample reducing the relative uncertainty below 4 percent.

We simulate the experiments involving the thermal excitation using the following equation

$$\langle \rho_{11}^{\mathrm{th}} \rangle = \sum_n p^{\mathrm{th}}(n) \langle \rho_{11}^{\mathrm{coh}}(n) \rangle \approx \int_0^\infty \mathrm{d}\Omega^2 \frac{\langle \rho_{11}^{\mathrm{coh}}(\Omega) \rangle}{\bar{\Omega}^2} \mathrm{e}^{\frac{-\Omega^2}{\bar{\Omega}^2}}, \tag{5.3}$$

where $\bar{\Omega}$ is the average Rabi frequency and the last approximation is valid for large average photon numbers $\langle \hat{n} \rangle$ [4] [36]. Thus we weight the response of the TLS to coherent excitation $\langle \rho_{11}^{\mathrm{coh}}(\Omega) \rangle$ with the coefficient dictated by the thermal statistics. The adoption of this model is justified for our experiments as the correlation time τ_{corr} is much longer than the coherence time T_2 and life time T_1 of our TLS, i.e. τ_{corr} = 900 ns vs T_2 ≈400 ps and T_1 ≈700 ps (see experiments section 5.2.4 and 5.2.6). In this context, it is also important to note that when discussing thermal light the relative scales of the involved times need to be taken into account. Firstly, in order to reveal the fluctuations in the photon number present in the thermal field the temporal resolution of the system (or detector) has to be considerably shorter than the correlation time of the light field. Because during observation times τ that are short compared to the correlation time τ_{corr} of the light field (i.e. $\tau \ll \tau_{\mathrm{corr}}$), the phase and intensity of the thermal light

[4] The average relative deviation of the occupation probability of the approximation from $p^{\mathrm{th}}(n)$ is roughly 1% for $\langle \hat{n} \rangle$ = 65 and monotonically decreasing for increasing $\langle \hat{n} \rangle$.

field can be considered constant [166]. That means that during each of these short intervals the thermal light actually is a coherent source. Only when integrating over several acquisition cycles (ideally several thousand) the intensity fluctuations become visible and the Bose-Einstein distribution is sampled uniformly. If however the correlation time is shorter than the temporal resolution of the system (or detector) the fluctuations are averaged and the light field would appear without any correlations to an observer [174].

In the experiments to be discussed in the following the minimum integration time is 100 ms during which the experiment is repeated on average at least 10^5 times even for small excitation powers.

5.2.2 The quasi-thermal light source and sample structure

The main problem is of course that thermal sources are typically broad band, are undirectional and exhibit low spectral brightness. For modern quantum optical spectroscopy these features are of course just the opposite of the requirements for a light source. In order to verify the theoretical predictions, we used a home built Martienssen lamp (cf. chapter 3.2), i.e. a quasi-thermal light source (QTS) . The experimental setup is sketched in Fig. 5.5 (a). Its input and output are fibre coupled which allows for an easy and modular use of the QTS. The circularly polarised laser is focused onto a ground glass disk with a diameter of 1 inch which was ground with a 3 μm-grain polish.. The disk itself is mounted on a electro motor allowing for rotation frequencies of up to 640 Hz. The reflected light is collected by a single mode fibre. We use a Martienssen lamp in a reflective configuration as opposed to a transmissive one because of higher mechanical stability and reproducibility.

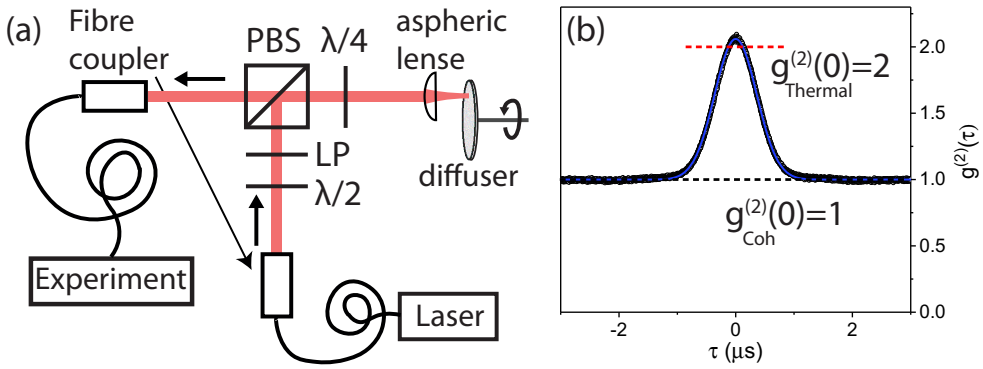

Figure 5.5: (a) Sketch of the home built Martienssen lamp. (b) Measured $g^{(2)}(\tau)$ function of the quasi-thermal light source. The blue solid line is a fit of $f(\tau) = 1 + A\exp[-\pi(\frac{\tau}{\tau_{\text{corr}}})^2]$ to the data giving a correlation time of 0.9 μs at a rotation frequency of 330 Hz.

A typical autocorrelation recorded behind the output fibre is plotted in Fig. 5.5 (b). As can be seen, the $g^{(2)}(0)$ is slightly above 2 which indicates small deviations from perfect thermal statistics. This can be attributed to imperfections in the experimental setup such as mechanical vibrations. The function

$$g^{(2)}(\tau) = Ae^{-\pi(\frac{\tau}{\tau_{\text{corr}}})^2} \tag{5.4}$$

is fit to the data from which we can extract the correlation time τ_{corr}. The relation between the

correlation time τ_{corr} and the rotation frequency ω of the ground glass is given by

$$\tau_{\text{corr}} \propto \frac{f\lambda}{\sigma\omega R}. \tag{5.5}$$

Here f (f=30 mm)is the focal length of the focusing lens, R (R=9.5 mm) is the distance between the focal spot and the centre of the ground glass, σ (σ = 0.7 μm) is the diameter of the focal spot and λ (λ = 780 nm) is the wavelength. This dependency was recorded for our Martienssen lamp. As can be seen in Fig. 5.6 (a) the measurements lie within the theoretically expected range (shaded area). The uncertainty is caused by the uncertainty with which we can determine the parameters in equation 5.5.

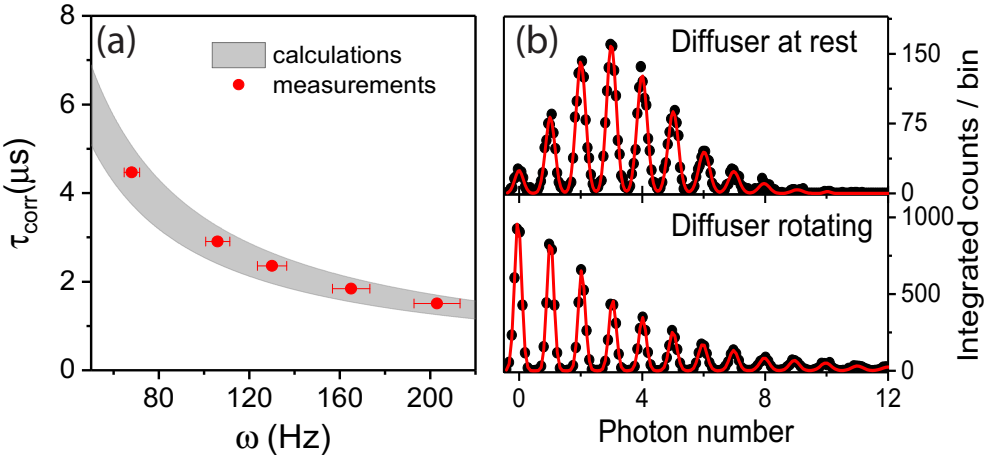

Figure 5.6: (a) Dependence of the correlation time τ_{corr} on the rotation frequency ω of the ground glass. (b) Upper (lower) panel: photon-number distribution of light emitted by the Martienssen lamp when the ground glass is at rest (rotating at ω = 40 Hz) as recorded with the TES using a pulsed diode laser at 660 nm as input. In both plots the average photon number is 4.08 photons per pulse.

Another neat and convincing experiment illustrating even more directly the way in which the Martienssen lamp alters the photon statistics is displayed in Fig. 5.6 (b). Here, pulses emitted by a pulsed diode laser were passed through the Martienssen lamp and the output fibre was connected to a transition edge sensor (TES) [41, 175]. The TES is capable via a calorimetric measurement to determine unambiguously the photon number within a pulse up to about 10 photons per pulse. By integration over many pulses it is thus possible to faithfully reconstruct the photon statistics of the light field. In the upper panel in Fig. 5.6 (b) the diffuser is at rest acting like a mirror. The photon number of the reflected pulses exhibit clearly a Poissonian distribution. The lower panel in Fig. 5.6 (b) shows the measurement where the diffuser is rotating at a frequency of ω=40 Hz and the photon statistics manifest a thermal dependency.

The sample used for these experiments is the same as the one used in section 5.1.

5.2.3 The steady-state regime

First, we want to investigate the response of a TLS to thermal light is the steady-state regime. Here, the laser is scanned across the resonance of the exciton under investigation and the scattered fluorescence is recorded by a SPCM. A typical laser scan well below saturation is shown in in the inset in Fig. 5.7. The absolute emission wavelength is 924 nm and the observed finestructure splitting is (37.4 ± 0.1) μeV.

Each scan is fit with two independent Lorentzians. Plotting the extracted peak height (here we only consider the peak at zero detuning) under laser excitation over the excitation power yields the blue graph in Fig. 5.7. The obtained data can be well fit by the expected saturation behaviour of a TLS given in equation 2.39. If we change now the excitation to the QTS and repeat the experiment we obtain the black dots. Taking the fit parameters obtained from the fit to the coherent data, we can reproduce the recorded data reasonably well using equation 5.3. From these measurements we can conclude that it is

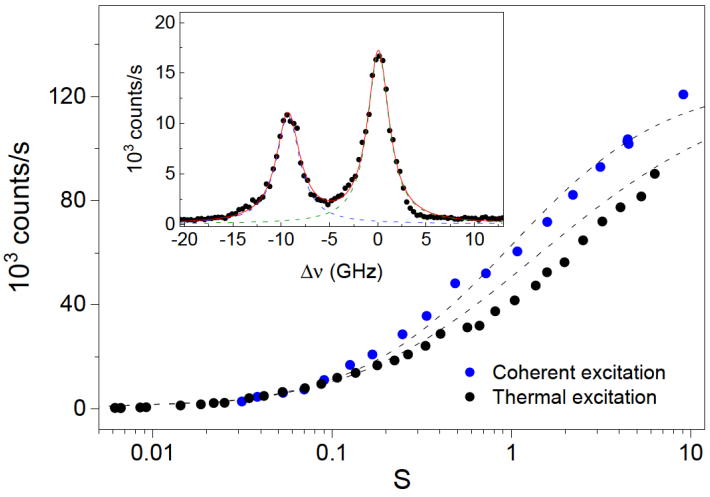

Figure 5.7: Blue (Black) dots: Saturation behaviour of the TLS under coherent (thermal) excitation. The excitation power is rescaled in the dimensionless saturation parameter S defined as $S = P/P_{\mathrm{sat}}$. The saturation power P_{sat}=95 nW is extracted from a fit of the coherent data to equation 2.39. The dashed line for the thermal excitation represents a simulations according to equation 5.3. The inset shows the laser scan across resonance at an intensity of $S = 0.1$. Two excitonic transitions are with visible with a fine-structure splitting of 9.1 GHz (37.6 μeV). The data in the main plot are extracted from experiments on the component centred at $\Delta\nu = 0$. The absolute emission energy at $\Delta\nu = 0$ is 1.34678 eV (920 nm).

less efficient to excite a TLS, i.e. a single-photon transition, with thermal light than with coherent light. This can also be intuitively understood as the photons in a thermal light field tend to arrive in bunches at the TLS. While one photon is absorbed and excites the exciton, the remaining photons pass the TLS unabsorbed. In the coherent case, of course, the photons arrive uncorrelated in time at the TLS, i.e. the likelihood of two or more photons arriving simultaneously at the TLS is reduced compared to the thermal light field.

5.2.4 The transient regime

After having examined the steady-state response of a TLS on the different photon statistics we turn to the transient regime. To this end we use a fibre-based EOM (*Jenoptik amplitude modulator am905*) with a bandwidth of 5 GHz which is driven by a custom made programmable pulse generator. We choose square pulses with a temporal width of 1.5 ns which is longer than the coherence time and lifetime of the typical QD exciton. The laser pulses used to excite the QD are shown in Fig. 5.9 as the shaded pulses.

In the top panel in Fig. 5.9 the response of the TLS, i.e. the time trace of the emitted fluorescence, to the coherent excitation is shown for three different excitation powers. The time trace shows clear Rabi

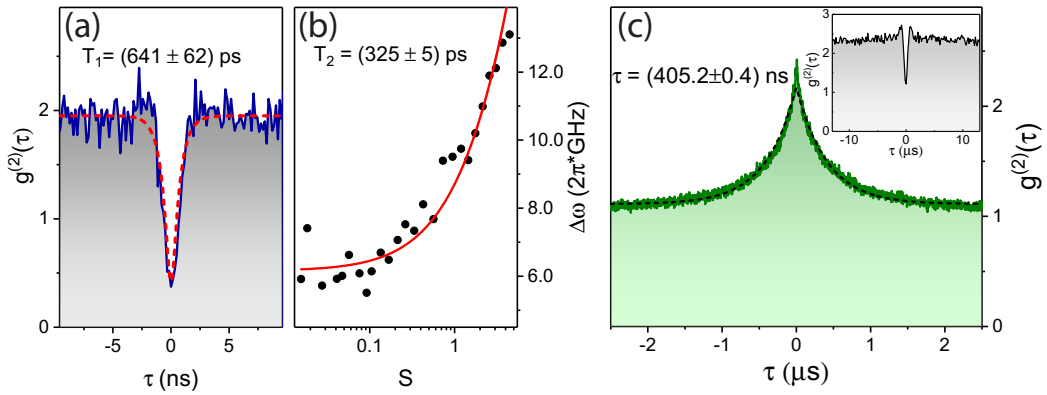

Figure 5.8: (a) The lifetime T_1 is extracted from a $g(2)(\tau)$ measurement at low excitation power (S≈0.6) yielding a value of T_1=(641±41) ps. (b) The decoherence time T_2 is extracted from the power dependence of the absorption spectra. Equation 2.41 is fitted to the data giving a decoherence time of T_2=(325±5) ps. (c) Intensity autocorrelation measurement revealing a long-time bunching of the fluorescence of the investigated QD. A exponential decay is fit to the data from which we obtain a correlation time of (405.2±0.4) ns. The inset shows the antibunchung visible on short time scales with the overshoot being indicative of the strong driving (Rabi oscillations).

oscillations as is expected for a TLS driven by a coherent, resonant light field. In order to theoretically describe the experiments, we solve the optical Bloch equations (cf. equations 2.37a) numerically. To reflect the experimental conditions, we make the Rabi frequency $\Omega(t)$ time dependent with a temporal shape corresponding to the one of the experimentally measured exciting pulses. The other parameters relevant for the simulation, i.e. T_1 and T_2 are extracted from the measurements shown in Fig. 5.8 (a) and (b). The simulation is able to reproduce the experiment quite well. However, for the larger Rabi frequencies we observe a slight deviation at longer time scales. This could be caused by slight deviations between the measured laser pulse shape and the one used for excitation which arise due to slow phase drifts inside the fibre-based EOM.

In the lower panel, we plot the result of the same experiment but this time using thermal light to excite the QD. Here, we observe no Rabi oscillations and only a simple switch-on behaviour of the fluorescence with a small overshoot is visible at the beginning of the pulse. This is in agreement with the theoretical predictions (cf. sections 2.4 and 5.2.1). Intuitively, this can be understood if we recall equation 5.3. To the QD the thermal light is just like the coherent light, it "sees" one fixed Rabi frequency during one excitation pulse. The amplitudes of the excitation pulses at a given average excitation power exhibit, however, a broad distribution given by the Bose-Einstein statistics. By integrating over many pulses ($> 10^7$) we sample the response of the TLS to each amplitude in this Bose-Einstein distribution uniformly. Thus, due to the large distribution of the amplitudes of the electric field under thermal excitation the Rabi oscillations are smeared out in the detected signal.

5.2.5 The emission spectrum

When thinking of resonance fluorescence, the Mollow triplet is of course its most iconic hallmark. We have seen in section 2.4.2 that an elegant explanation can be given in the framework of dressed states, i.e. coherent superpositions between the states of the exciting light field and the states of the TLS. One important prerequisite for the validity of this picture is, however, that the average photon number of

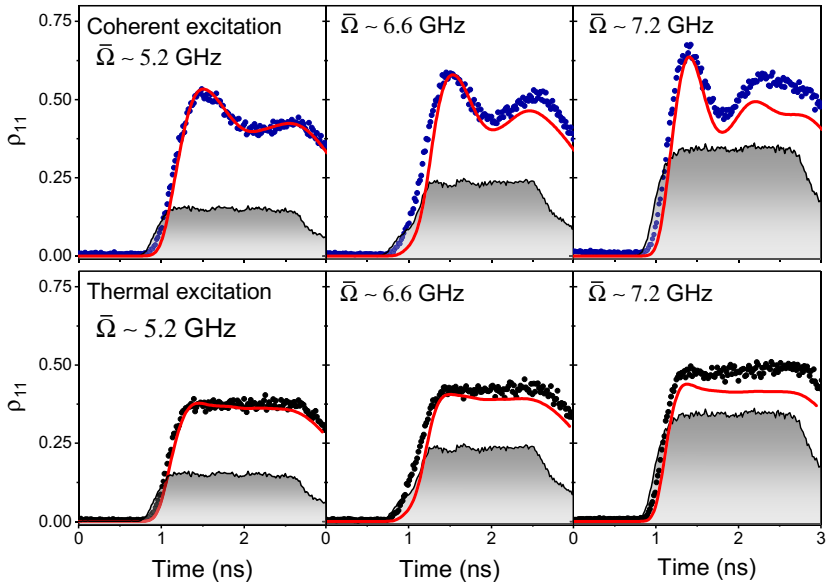

Figure 5.9: Time trace (dots) of light scattered by a single QD upon resonanct excitation by a 1.5 ns long square pulse (rescaled: solid black line). Upper panel: Excitation by coherent light shows Rabi oscillations of the exciton for three different average Rabi frequencies $\tilde{\Omega}$ (approximately 5.2, 6.6 and 7.2 GHz, respectively). Lower panel: Excitation by chaotic light by pulses of the same intensity creates no oscillations. The solid, red line represents simulations based on the optical Bloch equations as described in the main text.

the exciting light field is very high and that the fluctuations are small compared to the average photon number (i.e. $\langle \hat{n} \rangle \gg \Delta \hat{n} \gg 1$). The later condition is clearly not fulfilled for a thermal light field. Since the Mollow triplet is also the spectral signature of the Rabi oscillations occurring in the temporal domain we are led to expect from the results of the experiments in the previous section also a vanishing of the Mollow triplet under thermal excitation as is also predicted by theory (cf. section 5.2.1).

In order to observe the Mollow triplet we use the Fabry-Perot interferometer described in section 3.3. The inset in Fig. 5.10 (a) shows the expected spectrum and in the main graph we plot the high energy part for three different Rabi frequencies. As expected the splitting between central and side peak increases with increasing power and a broadening of the sidebands is observed. A convolution of equation 2.52 and the IRF of the FPI is fit to the coherent data. For the data under thermal excitation we also used equation 2.52 weighing the contribution of the different Rabi frequencies according to the Boltzmann statistics. All parameters except for the average Rabi frequency are kept identical for all spectra. The apparent deviations between theory and experiment observed for higher Rabi frequencies can be again attributed to excitation induced dephasing processes (cf. section 4.1) which are not included in the theory. Figure 5.10 (b) shows the emission spectra for the same excitation powers but under thermal excitation. As expected no sidebands are discernible which is again in good agreement with the theoretical prediction. Thus, our experiments confirmed theoretical predictions that the emission spectrum of a TLS acts indeed as a very sensitive probe of the higher order correlation functions of the exciting light field.

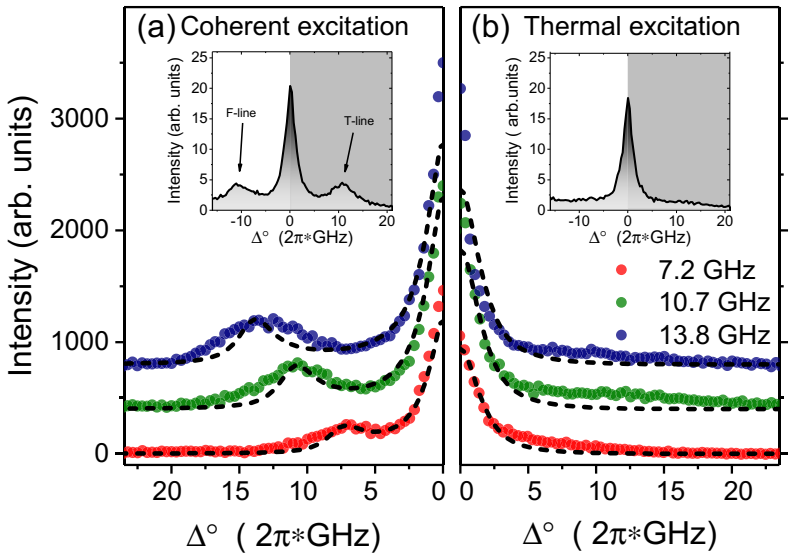

Figure 5.10: Emission spectrum of the strongly driven QD for three different average Rabi frequencies. Panel (a) displays the result obtained for coherent excitation. The T-line of the Mollow triplet is clearly visible. Inset: Complete emission spectrum highlighting the displayed part of the Mollow triplet. For chaotic excitation, shown in (b), no side peaks are discernible. The dashed lines represent simulations according to equation 2.52 with T_1 = 710 ps and T_2 = 500 ps convolved with the IRF of the FPI.

5.2.6 The photon statistics of the emission

The previous experiments have shown that a TLS responds very sensitively to the intensity fluctuations present in a classical light field. This hinged mostly on coherence in the system being induced by the well defined phase and amplitude of the laser which is averaged out by the large intensity fluctuations in the experiments involving thermal excitation. The single-photon emission however is not a coherent effect but a consequence of the discrete level structure of the emitter and the quantisation of the light field. It is thus obvious that the photon statistics of the emitted light field, i.e. the emission of single photons by the TLS, should be observable independent of the statistics of the exciting light field. As discussed in section 5.2.1 this was also predicted by Schubert and coworkers [169]. In order to verify this prediction we use a fibre-based HBT interferometer and record the intensity autocorrelation function $g^{(2)}(\tau)$. The APDs used for this experiment are the Excellitas modules providing a combined temporal resolution of the HBT setup of $\Delta\tau_{FWHM}$ = 550 ps. In Fig. 5.11 (a) the result of the measurement under weak coherent excitation (S≈ 0.6) is displayed. We observe the expected antibunching on time scales which are short compared to the lifetime of the emitter ($\tau < T_1$). For intermediate time scales ($10\,\mu s > \tau > T_1$) we observe a bunching. Such a bunching is typically caused by blinking of the emitter [101, 176, 177]. Various mechanisms can give rise to such a blinking be it spectral diffusion, dark states or charging of the QD. In this particular case the blinking has a correlation time of 405 ns (cf. Fig. 5.8 (c)). Under thermal excitation (Fig. 5.11 (b)) we likewise observe an antibunching for $\tau < T_1$ albeit with a slightly deteriorated $g^{(2)}(0)$. This is most likely due to the limited temporal resolution of our detectors. Since the bunching effect for the intermediate time scales is increased compared to the coherent case a convolution of the real signal with the IRF automatically leads to an increased $g^{(2)}(0)$ value. We discussed the expected results for an ideal TLS under thermal excitation in section 5.2.1. The presence

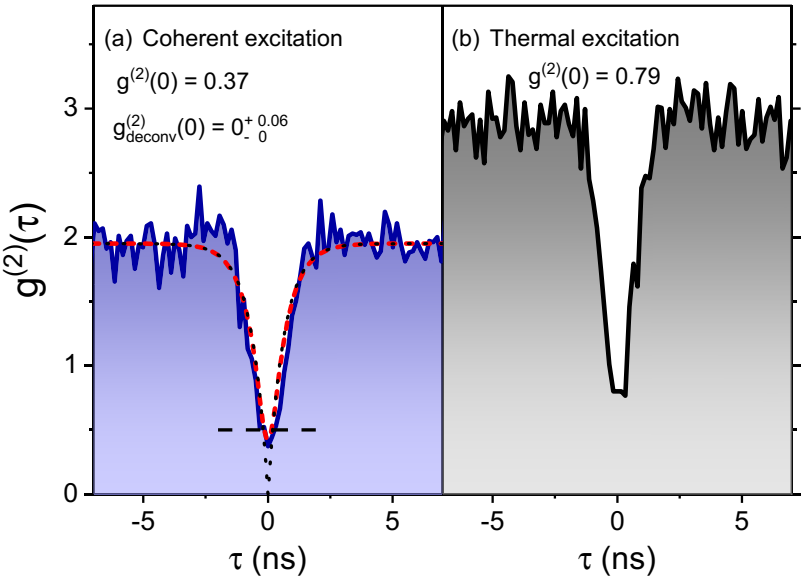

Figure 5.11: $g^{(2)}(\tau)$ measurement of the emitted radiation. The excitonic transition is driven at a Rabi frequency of $\Omega \approx 1.7$ GHz (0.6 S). (a) Measurement using the laser as the light source (solid line). The dashed line shows a convolution of the solution for a TLS with the detector response and provides very good agreement with the experimental data. (b) Measurement using the Martienssen lamp as the light source. In both measurements, pronounced antibunching is visible at $\tau = 0$.

of blinking in our system whose exact origin is unknown renders a direct comparison to the theory difficult. From the measurements we can conclude however that, trivially, a TLS emits non-classical light irrespective of the statistics of the exciting light field.

5.2.7 Two-photon transitions

As we have seen in section 5.2.3 the excitation of a single TLS with thermal light is less efficient than coherent excitation. However this is predicted to change for higher order absorption processes such as a two-photon absorption process [173]. The underlying physics and technicalities are presented in full detail in chapter 6. At this point we restrict ourselves only to a discussion of the results pertinent to the current topic, i.e. the influence of the photon statistics of the exciting light field on the response of the quantum system.

Figure 5.12 (a) shows the spectrum of a biexciton cascade under resonant two-photon excitation (the excitation scheme is depicted in Fig. 2.9). The blue (black) line represents the spectrum under coherent (thermal) excitation for an excitation power of approximately 300 μW. Evidently, the thermal excitation leads to a higher occupation of the biexciton state than the coherent excitation at the same excitation power. A saturation curve is displayed in Fig. 5.12 (b). Unfortunately, due to the considerable losses of optical power in our Martienssen lamp (around 2 orders of magnitude) we are only able to go up to about one sixth of the saturation power of 1.9 mW in these experiments. However, we already observe the predicted increased efficiency in populating the biexcitonic state using thermal excitation. In an intuitive picture, this is explained by the increased probability that in thermal light field two photons arrive simultaneously at the three-level system. Generating biexciton population is a two-photon process and thus it is understandable that bunched photons are favoured. This in of course

in contrast to single-photon transitions such as QD excitons where in principle antibunched photons are most efficient.

Due to this property, two-photon transitions can be used to probe temporal photon correlations in light fields on much shorter time scales than is possible with current photo detectors [178, 179].

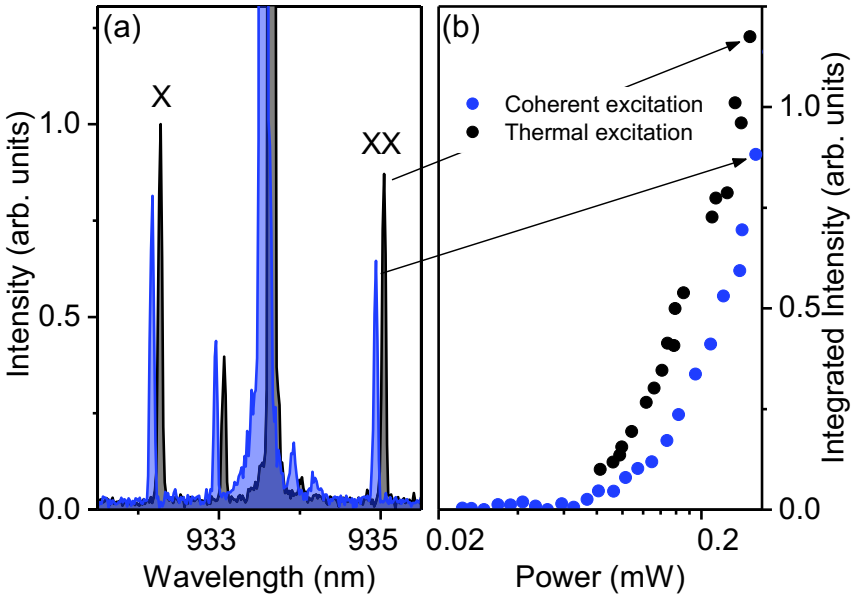

Figure 5.12: (a) Spectrum of the biexciton cascade under resonant TPE. The black (blue) curve represent the experimental data obtained under thermal (coherent) excitation at (almost) identical excitation powers. The thermal spectrum is shifted by 0.1 nm to larger wavelengths for better visibility. (b) Black (blue) dots: Saturation behaviour of the resonantly driven biexciton under thermal (coherent) excitation.

It would be highly appealing to reach the strong excitation regime under thermal excitation in this experiment where we can observe interesting phenomena under coherent excitation which we will discuss in chapter 6. Theoretical studies and predictions for such experiments, e.g. the emission spectrum of the resonantly driven biexciton cascade, are also lacking so far.

5.3 Summary of chapter 5

In this chapter we investigated several different phenomena that can be studied experimentally using the exciton as two-level system.

In section 5.1 we investigated the Wigner time delay induced by a single QD. We were successfully able to measure the effect and qualitatively reproduce the expected dependency of the temporal delay on the detuning. We found a maximum delay of 530 ps close to resonance which exceeding the expected value of 450 ps determined via an independent measurement. Simulations of the experiment showed that this deviation is caused by the presence of pure dephasing in our system leading to a significant portion of incoherently scattered photons. This incoherent fraction lags behind the coherently scattered fraction thus shifting the center of the overall scattered pulse to values larger than the expected value derived for the coherent response of the system.

For the experiments in section 5.2, we first built and characterised a Martienssen lamp which is a source of quasi thermal light. We then discussed a list of predictions that were made for the resonant excitation of a TLS with thermal light. Subsequently, we present resonance fluorescence experiments where we contrast the response of the TLS to thermal and Poissonian photon statistics. Most strikingly, we evidence the disappearance of the Mollow triplet under thermal excitation and the suppression of Rabi oscillations in the temporal domain. Furthermore, we showed that it is more efficient to excite the biexciton with thermal light than with coherent light. While our experiments involved only classical photon statistics as an excitation source, it is certainly more interesting to move the experiments to non-classical statistics. Such an experiment can for example be realised by quantum cascaded systems [180, 181] which have attracted a lot of research interest recently [182–184]. While first experiments have been done [22, 185], the enhancement of photon collection efficiencies and light-matter coupling strengths are vital to these experiments.

Die Schönheit der Theorie wird durch
die Nähe zum Experiment zerstört.

Andreas Knorr

6

Coherent excitation of the biexciton: a cascaded cascade

In the previous chapters we have seen that (charged) excitons in QDs are a decent approximation of the idea of a two-level system which has rendered them very attractive for fundamental research[1]. As discussed in the introduction to this thesis QDs show, however, considerable promise beyond fundamental science. For example the biexciton cascade allows for the generation of photon pairs which are resources of heralded single photons and can be utilised for various schemes in QKD or in the quantum repeater concept. Moreover, entangled photon pairs allow for the investigation of the non-local properties of quantum mechanics, probably its most intriguing feature.

Due to these prospects the biexciton cascade of QDs has attracted a lot of research interest since it has been first proposed as a source of polarisation-entangled photon pairs [15]. The emission of time-correlated photon pairs by this cascade was first experimentally demonstrated in 2001 [189]. It took however a few more years until the first experimental proof of the polarisation-entanglement of photon pairs emitted by this cascade was presented in 2006 [190]. Another possibility to create entangled photon pairs using this cascade, so called time-bin-entanglement, was shown in 2014 [191]. The simultaneous entanglement in both degrees of freedom, so called hyper-entanglement, was also recently reported [192].

Resonant and coherent excitation of the cascade which is a prerequisite for time-bin entanglement and beneficial to polarisation entanglement distribution via Bell state measurements is usually achieved using a pulsed two-photon excitation scheme. Two-photon emission from the cascade using resonant cw excitation was also recently explored theoretically [193]. Furthermore, in this work it was shown that due to the creation of dressed states via two-photon excitation the selection of different spectral windows could be used to tune the statistics of the emitted photon pairs. The experimental observation of this dressed biexciton cascade was reported in 2016 independently by two research groups [194, 195]. The photon-photon correlations of photons emitted in this dressed cascade has, however, remained unexplored mainly due to an insufficient signal to noise ratio. In the following chapter we will therefore aim to investigate for the first time the correlations of the photons emitted in this dressed cascade.

First, we will characterise the non-resonantly pumped cascade. Then we will present experiments

[1] Although such TLS are usually considered to be the single-photon emitter par excellence they can also be used to generate multiphoton states, such as two-photon states and photon pairs [186–188].

using the Ti:Sa for pulsed two-photon excitation. The main part of this chapter will be devoted to the investigation of the cascade dressed by a cw laser. As a first step we will explore the dephasing mechanisms in the dressed system and show that for large powers the linewidth increases quadratically as a function of excitation power. The observation of the renormalisation of the Rabi frequency with temperature suggests that phonons are also the main source of decoherence in this system as is the case for excitons in QDs . Subsequently, we will perform time resolved measurements under cw excitation allowing us to evidence the resonant, coherent interaction between the biexciton and ground state by observing two-photon Rabi oscillations. Finally, we look at the correlations between photons emitted in this cascade. Our experiments show that by adjusting power, spectral filters or detuning different photon pair correlations can be distilled. Most of the results presented in this chapter have been published in Ref. [196] and [197].

6.1 Characterisation of the biexciton cascade

In this chapter the sample used for the experiments are again self-assembled InGaAs QDs grown by MOVPE on a GaAs substrate. A DBR consisting of 23 alternating $\lambda/4$-thick bi-layers of AlGaAs/GaAs is located 65 nm below the low density ($2.5 * 10^8$ cm^{-2}) QD layer. A 400 nm thick GaAs capping layer covers this QD layer and is utilised for the monolithic fabrication of the microlenses. The monolithic microlenses were fabricated using a deterministic nanoprocessing technique based on low temperature cathodoluminescence and 3D in-situ electron beam lithography [144, 198]. Figure 6.1 (a) shows a SEM image of such a microlens while in (b) an optical image of a processed sample with 3 EBL written field each with 6-8 microlenses.

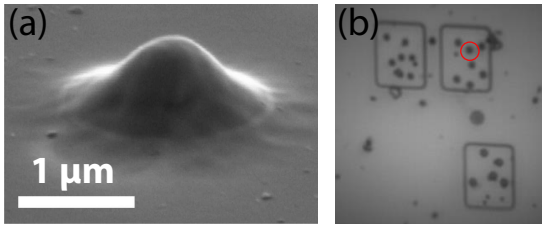

Figure 6.1: (a) SEM image of a microlens. (b) Optical image of sample surface with processed microlenses. The red circle encloses the microlens in which the investigated QD is embedded.

The preliminary characterisation of the QD under non-resonant excitation aims to identify and assign the different observed spectral lines to the different excitonic complexes, in particular the exciton and biexciton.

Under excitation by the 785 nm laser three bright spectral lines can be observed. Biexciton and exciton are located at 935.05 nm and 932.83 nm, respectively.

The first hint for identifying spectral lines from QDs is usually obtained by performing a power dependent measurement of the emission spectrum which is displayed in the inset in Fig. 6.2. Here, the intensity emitted by the exciton increases with a slope of roughly $m_X = 0.77 \pm 0.02$ in the low excitation range while a slope of m=1 is ideally expected in a double logarithmic representation. The biexciton only starts to emit at higher incident powers. This power is typically the point where the population rate of the s-shell of the QD via relaxation processes of electrons and holes from above the band gap is faster than the decay rate of the exciton. Hence biexciton complexes can be formed. The saturation of the biexciton slope is well reproduced with a slope of $m_{XX} = 1.85 \pm 0.03$. A typical quotient of the two slopes is 2 since the biexciton can decay in a simple model to two excitonic states hence its decay rate is twice as large as the exciton decay rate. In our experiment, the quotient is $m_{XX}/m_X = 2.4 \pm 0.1$ which could hint at spin relaxation processes which would lead to an increased measured exciton lifetime [76,

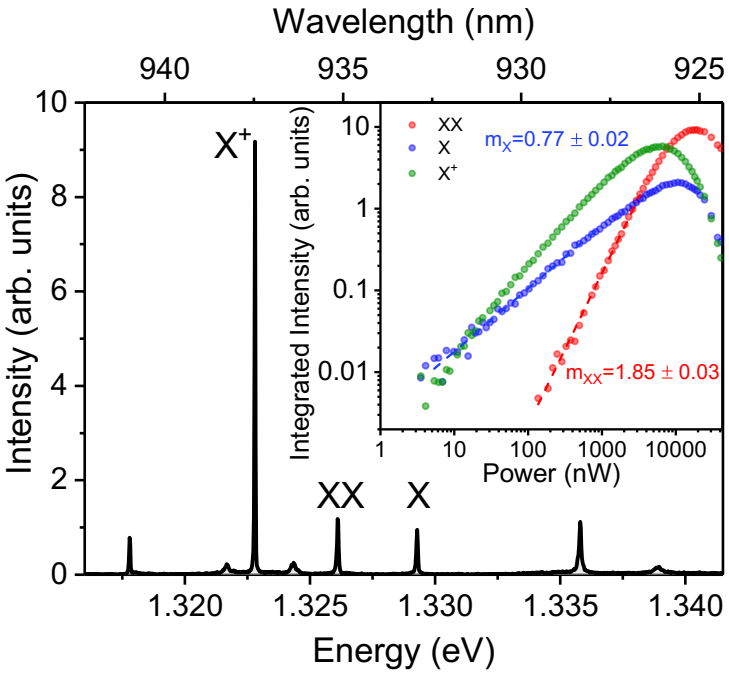

Figure 6.2: Non-resonant excitation spectrum of the QD (λ_{exc} = 785 nm). Inset: Saturation behaviour of the three labelled emission lines. The exciton and biexciton are each fit with an exponential function with an exponent of $m_X = 0.77 \pm 0.02$ and $m_{XX} = 1.85 \pm 0.03$, respectively. Dividing the exponents yields $m_{XX}/m_X = 2.4 \pm 0.1$.

199]. Additionally, in the experiment, there is the possibility that the biexciton decays not only into the neutral exciton state but also into other charged or dark exciton states [199]. This can lead to the observed deviation of the expected quotient of two.

Harder evidence for the identification of the exciton and biexciton lines is gained by performing polarisation resolved measurements. The results are displayed in Fig. 6.3 b. The exciton and biexciton lines show a clear oscillation as a function of the orientation of the $\lambda/2$-plate with opposite phase. We extract a finestructure splitting of (17.7 ± 0.8) μeV. This value is in agreement with the result of a laser scan across the exciton resonance with $\Delta E_{\mathrm{FSS}} = (18.8 \pm 0.6)\mu eV$ [cf. Fig. 6.3 (c)]. As mentioned previously, photons emitted by this cascade show strong correlations with respect to their emission time [200]. This can be evidenced in a cross-correlation measurement. The term cross-correlation signifies here that the temporal correlations between photons in two different spectral windows are investigated. In Fig. 6.3 (a), the result of a cross-correlation between the exciton and the biexciton under non-resonant excitation is shown. The bunching for positive time delays ($\tau > 0$) indicates that the detection of a biexciton photon heralds the detection of an exciton photon. Conversely, the anti-bunching for negative time delays ($\tau < 0$) signifies that the probability to detect a exciton photon before biexciton photon is strongly reduced. This result is intuitively expected from the level scheme sketched in the inset of Fig. 6.3 (a). If the s-shell of the uncharged QD is populated by two electron-hole pairs the first recombination will be accompanied by the emission of a photon with the energy E_{XX}. The consecutively emitted photon will have the energy E_X. The time before the QD can emit another XX photon is given by the population (pumping) rate.

The previous measurements have unambiguously identified the exciton and biexciton state of the QD. All these measurements were performed under non-resonant excitation, i.e. by exciting the sample

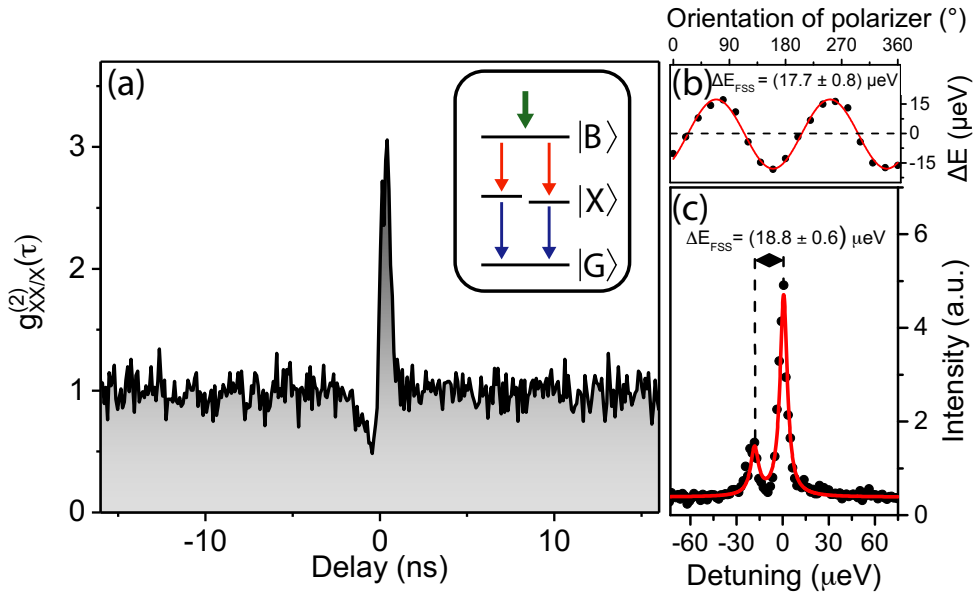

Figure 6.3: (a) Cross-correlation function of the exciton and biexciton emission lines under non-resonant excitation. Inset: level scheme of non-resonantly pumped biexciton cascade. (b) Extracted polarisation dependence of the emission energy difference $\Delta E = (E_{XX} - E_X) - (\overline{E_{XX}} - \overline{E_X})$. (c) Resonance scan of the exciton transition revealing two excitonic lines with a finestructure splitting of 18.8 μeV.

above the band gap. Of course, following the experiments on resonant excitation of excitons and seeing the benefits it brings with it researchers also showed a few years later that it is possible to excite this cascade resonantly via a two-photon excitation process in III-V QDs [16, 201, 202]. While typically pulsed excitation is used for two-photon experiments (because of the low scattering cross section of such a process) it should also be possible to excite such a system resonantly with a high intensity cw laser. In this case, as had been predicted theoretically [193], the observation of two-photon dressed states should become possible. This dressing was indeed experimentally observed independently by two groups in 2016 [194, 195]. The analogy to the Mollow triplet which is the dressing of a single two-level system is evident while of course the complexity of the system is a little increased.

6.2 The two-photon dressed cascade

In the remainder of the chapter, we present the experiments involving the resonant excitation of the biexciton cascade. As we have discussed previously, two-photons are successively emitted during the biexciton cascade. Consequently,the inverse process, the resonant excitation of the biexciton, requires the absorption of two photons due to the conservation of angular momentum. Furthermore, energy conservation obviously requires that $\omega = \omega_1 + \omega_2$, i.e. the sum of the frequencies of the two incident photons must equal the transition frequency. The experimentally most convenient choice is of course to use two photons of the same frequency $\omega_1 = \omega_2 = \frac{\omega}{2}$. For our specific experiments the resonance condition is fulfilled when $\omega_L = \omega_{XX} + \Delta E_B/2$. Thus the biexciton binding energy actually allows us to drive the two-photon resonance without simultaneously driving the exciton, i.e. the single-photon transition. The level and excitation scheme is depicted in the inset of Fig.6.4.

Our first experiments on two-photon excitation were performed using pulsed excitation[2]. A typical spectrum is shown in Fig. 6.4 (a). A spectrometer was used for pulse shaping giving a pulse of 13 ps length and a spectral width of about 150 μeV. The time-bandwidth product of our pulse is 0.47 which is above the Fourier-limit of 0.44 for Gaussian pulses and could hint at a certain degree of chirp of the laser frequency. Figure 6.4 (b) shows Rabi oscillations as a function of the pulse area illustrating that we indeed drive our system resonantly. The form of the observed oscillations is quite different to what would be expected. The detected intensity under application of a π-pulse does not lead to the highest occupation and thus fluorescence but the intensity continues to increase with power. The reason could be a slight spectral detuning of the laser, a moderate chirp and also intrinsic QD properties. It is noteworthy that oscillations are observed for both the biexciton and the exciton population. This can be explained by the fact that we prepare our system within the pulse duration of 13 ps which is substantially shorter than the lifetime of the biexciton (300 ps). Thus after a π-pulse the population of $|XX\rangle$ is maximal and stays there until a photon is emitted and the system collapses to the state $|X\rangle$ upon detection of the photon. The likelihood of the occurrence of the event, i.e. the emission of the photon, is proportional to the population of $|XX\rangle$ and decreases with time exponentially with the decay time as time constant.

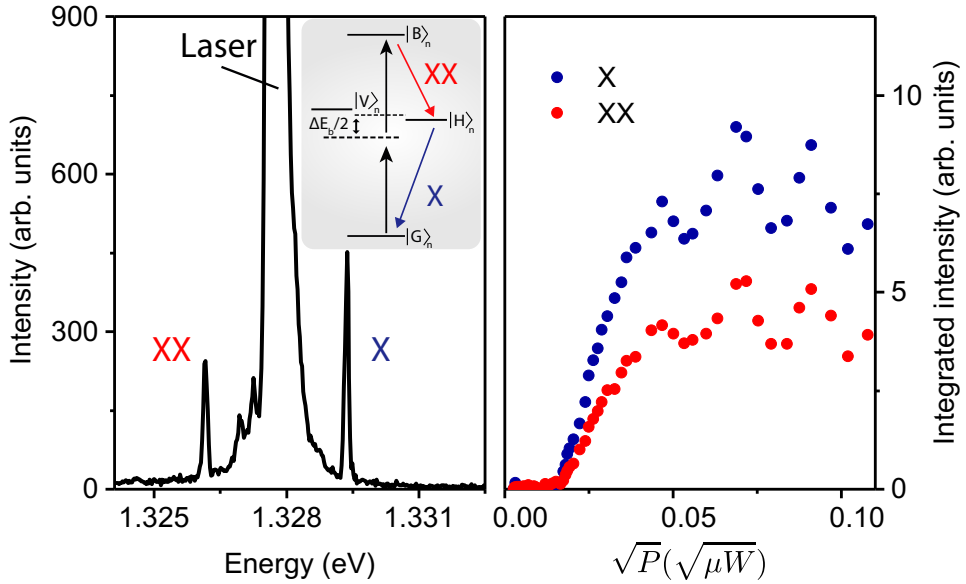

Figure 6.4: (a) Spectrum under π-pulse excitation. Emission from the exciton is considerably stronger than from the biexciton. Inset: Resonant two-photon excitation scheme of the biexciton cascade. (b) Integrated intensities as a function of the square root of the excitation power revealing Rabi oscillations.

In the absence of other decay channels all the population of $|XX\rangle$ is transferred to $|X\rangle$ in this manner, thus the fluorescence from $|X\rangle$ will also be maximal. After the application of a 2π-pulse the population of $|XX\rangle$ is of course minimal and accordingly also the fluorescence from both states $|XX\rangle$ and $|X\rangle$ is minimal. It is thus understandable that under pulsed excitation the fluorescence from $|XX\rangle$ and $|X\rangle$ both exhibit oscillations. As we will see later in the chapter however this is changed under cw excitation when we observe the Rabi oscillations as a function of time.

[2]It is interesting to note that the two-photon excitation worked without the additional background laser which was indispensable in the experiments on the single-photon transitions presented in chapter 4 and 5.

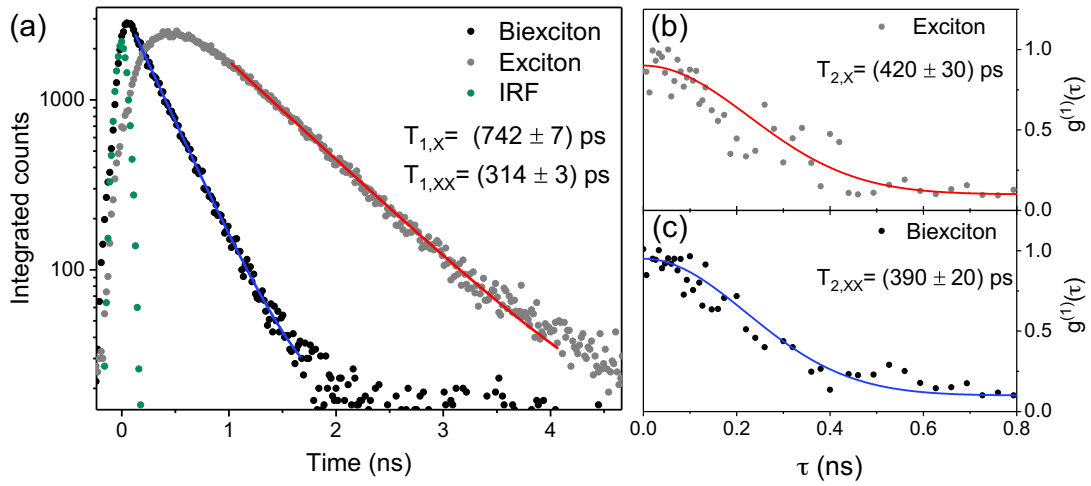

Figure 6.5: (a) Lifetime measurement via TCSPC under pulsed resonant excitation. The grey (black) data are the detection events of the exciton (biexciton) photons. The green data represents the instrument response function of the SSPDs. The lifetimes extracted from a mono-exponential fit are (742 ± 7) ps and (314 ± 3) ps, respectively. (b) [(c)] Measurement of the first order coherence of the exciton (biexciton) photons using a Michelson interferometer. By fitting a Gaussian to the data we extract docoherence times of (420 ± 30) ps and (390 ± 20) ps, respectively.

The aforementioned mechanism can also be used to determine the radiative lifetime of the exciton and biexciton state. Application of a π-pulse yields maximum signal and is used to excite the sample in the two photon resonance. The recorded and histogrammed fluorescence counts are displayed in Fig. 6.5 (a) along the IRF of the SSPDs used for detection. The extracted lifetimes of the biexciton and exciton are ($T_{1,XX}$ = 314 ± 3) ps and ($T_{1,X}$ = 742 ± 7) ps, respectively. The quotient of these two times, $T_{1,X}/T_{1,XX}$, is 2.36 ± 0.05 which is the same value within the accuracy that we observe for the gradient of the slopes in the saturation measurements (cf. Fig. 6.2). Equally interesting are of course the T_2 times of this system which determines how quickly the quantum mechanical phase information is lost. To this end we switch to cw excitation of our system and use a Michelson interferometer to probe the degree of first order coherence of the photons emitted by the cascade. The extracted visibilities as a function of temporal delay are shown in Fig. 6.5 (b). We obtain dephasing times for the exciton and biexciton of $T_{2,X}$= (420 ± 30) ps and $T_{2,XX}$= (390 ± 20) ps, respectively. Thus the dephasing times for both states are identical to within the errors. From these two measurements we thus determine the values of $\frac{T_2}{T_1}$ for the exciton and biexciton state which are 1.24 ± 0.07 and 0.56 ± 0.04, respectively. It should be noted that dephasing mechanisms in QDs exhibit a dependence on the excitation power which we will also discuss in the following section for this system. For the presented measurements we chose an intermediate excitation power for the sake of a decent signal to noise ratio. Thus it is possible that the maximum decoherence times in the system are larger than the ones stated above.

Dressing of the cascade

After having determined the T_1 and T_2 times of our system, we now turn to the investigation of the dressed-state system. Figure 6.6 shows spectra recorded with the spectrometer. At low excitation powers (shown in Fig. 6.6 (b)) we observe the two emission lines X and XX which are also observable

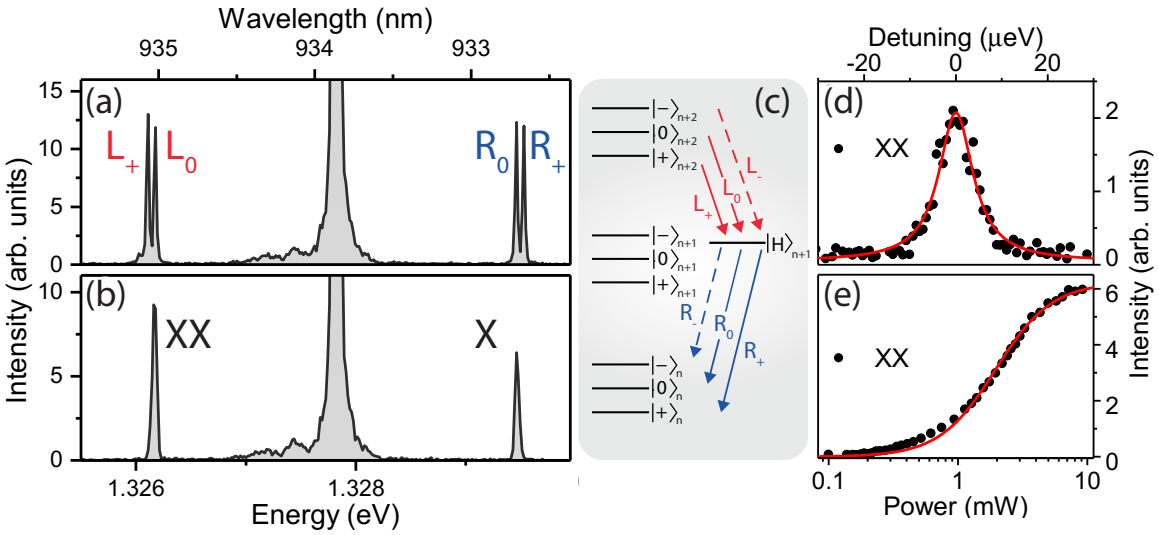

Figure 6.6: (a) Spectrum at an excitation power of 3.8 mW. Now the peaks are split evidencing the resonant interaction of the ladder system and the coherent light field. The peak in the middle is reflected laser light. (b) Spectrum on resonance under cw two-photon excitation at an excitation power of 100 μW. (c) Dressed states in the rotating frame. The arrows indicate possible transitions in the horizontal polarisation. (d) Integrated intensity of the biexciton emission as a function of detuning. The two-photon resonance has a linewidth of 9.8 μeV at this excitation power. (e) Dependence of the integrated intensity of the biexciton on the excitation power. Equation 6.1 is fit to the data yielding a saturation power of $P_{sat} = \Omega^2_{sat} = 1.9$ mW.

under non-resonant excitation. By increasing the power we observe a splitting of the exciton and biexciton emission line as is exemplary illustrated by the spectrum in Fig. 6.6 (a)). Interestingly, this splitting is so large that it is well resolvable with our spectrometer (resolution: 30 μeV). The emission lines in the spectrum which are labelled with L are photons that are emitted from the dressed states $|+\rangle$ and $|0\rangle$ respectively into the bare state $|H\rangle$ [3]. Likewise, the emission lines labelled with R correspond to transitions from the bare excitonic state $|H\rangle$ to the dressed states. For a more intuitive understanding, we sketched the underlying level scheme of the dressed basis in the rotating frame in Fig. 6.6 (c). Importantly, the polarisation of the excitation is in the vertical direction and aligned parallel to one of the excitonic transitions. As indicated in the sketch, we only detect photons emitted into and from the horizontally polarised exciton state, i.e. orthogonal to the excitation. In our experiments we only observe four emission lines although in our configuration we should be able to observe six lines (cf. section 2.5). The two missing emission lines correspond to emission from and to the state $|-\rangle$ and are located very close to the two-photon resonance. Theory predicts also that their emitted intensity is at least one order of magnitude lower compared to any of the other four emission lines (cf. Fig. 2.10). Hence in our experiments residual reflected laser prevents us from observing these lines. The additional use of narrow band interference filters could be used to remove the laser altogether and would possibly enable the observation of these two lines in the future.

Similar to the experiments on single-photon transitions in the previous chapter, we can also record an excitation spectrum of the two-photon transition as is shown in Fig. 6.6 (d). The measured transition

[3] The dressed states $|+\rangle$ and $|0\rangle$ are superpositions of the bare states $|G\rangle$,$|V\rangle$ and $|B\rangle$ which are given on resonance by the equations 2.57.

linewidth is 9.8 μeV. Plotting the integrated intensity of the biexciton as a function of excitation power we obtain the graph in Fig. 6.6 (e). On resonance the steady-state fluorescence from the biexciton is given by

$$I_{fl} \propto \rho_{BB}^{st}(\Omega) = \frac{1}{2}(1 - \frac{1}{1 + (\frac{\Omega}{\Omega_{\text{sat}}})^4}) \tag{6.1}$$

where Ω is the single-photon Rabi frequency. The data is well reproduced by fitting equation 6.1 to the data. In contrast to the single photon transition the denominator grows as a function of the square of the incident power. This is again a clear indicator that we excite the system via a two-photon absorption process.

By tuning the laser relative to the two-photon resonance we can observe the dispersive behaviour of the emission lines. The results are plotted in Fig. 6.7 (c). For both doublets we observe a clear anticrossing on resonance. In our experiments we observe the curious feature that the dispersion is not symmetric with respect to the two-photon resonance as is, however, expected by simulations of the system assuming radiatively limited dephasing (cf.Fig. 6.7 (d)) [4]. As is shown in Fig.6.7 (e) we can reproduce the experimental findings by including pure dephasing in our model where the experimentally determined values for T_1 and T_2 were used. This missing symmetry is also in agreement with the observations of Hargart *et al.* [195] who explicitly included the phonon-exciton interaction in their simulations. Hence, this asymmetry can be considered as a first indication of phonon influence in our system. This observation is also interesting with respect to the Mollow triplet where pure dephasing also leads to an asymmetric intensity ratio of the sidebands under detuning.

A power series of the emission spectrum is shown in Fig. 6.7 (a). The eigenvalues given in equations 2.56 predict that the splitting of each doublet grows as $\sqrt{\Delta E_B^2 + 8(\Omega\hbar)^2}$ [5]. The biexciton binding energy in our experiments is around 3.15 meV and the maximum power at the sample around 10 mW which leads to Rabi frequencies in the range of around 100 μeV. Consequently, the first term under the square root is in our experiments at least two orders of magnitude larger than the second term. Thus we only explore the low power regime of the splitting where the square root dependency in power can be linearly expanded in a Taylor series. This is in accordance with the linear energy shifts with power of the L_+ and R_+ states which we observe in our experiments. While the splitting is well resolvable with a standard spectrometer it is noteworthy that the linewidth stays below its resolution limit (which is roughly 30 μeV) regardless of the excitation power in this measurement. However, we would naively expect to observe a broadening of the linewidth as pulsed two-photon excitation schemes also display a damping of the Rabi oscillations due to phonons [16, 202].

Consequently, in order to determine the linewidths and their power dependence we switch in the following experiments to the FPI which affords a spectral resolution of 106.2 MHz (438.4 neV). Exemplary spectra which are part of a power series recorded with the FPI are shown in Fig. 6.8 (a) and (b). The L and R doublet exhibit the same spectral dependency already observed with the spectrometer. That is that the emission line $L_0(R_0)$ stays almost at the same energy while $L_+(R_+)$ shifts away from the two-photon resonance.

For higher excitation powers we only observe the L_0 and R_0 transition which is due to the cascaded

[4] The simulations are performed in the frame rotating at the laser frequency. Hence the simulations exhibit a linear frequency shift with a negative gradient with respect to the experiments.

[5] This is very reminiscent of the effective Rabi frequency in a TLS $\Omega = \sqrt{\Delta^2 + \Omega_R^2}$ with the obvious difference that even on resonance we are "far detuned".

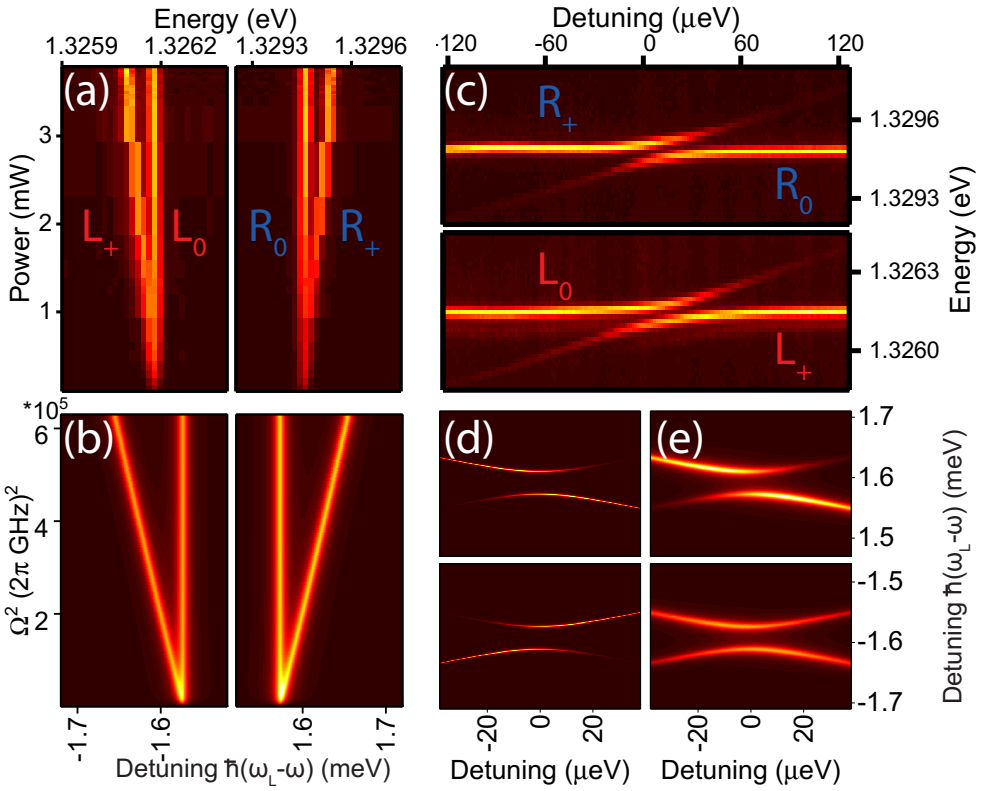

Figure 6.7: (a) Emission spectra of the two-photon excited QD as a function of excitation power for the L and R doublet. (b) Simulation using equation 2.54 and 2.55 of the power dependence shown in (a) including pure dephasing. The experimentally determined parameters were used for T_1 and T_2. (c) Emission spectra as a function of the detuning between laser and two-photon resonance. On resonance a clear anti-crossing is observed for both doublets. (d) Simulation of the dispersion behaviour plotted in (c) without pure dephasing. The spectra are symmetric with respect to the two-photon resonance irrespective of the detuning and in contrast to the experimental data. (e) Simulation of the dispersive behaviour with pure dephasing. The symmetry is lost reflecting the experiment. The simulations are performed in the frame rotating at the laser frequency which leads to the linear gradient of the spectral lines in the simulations.

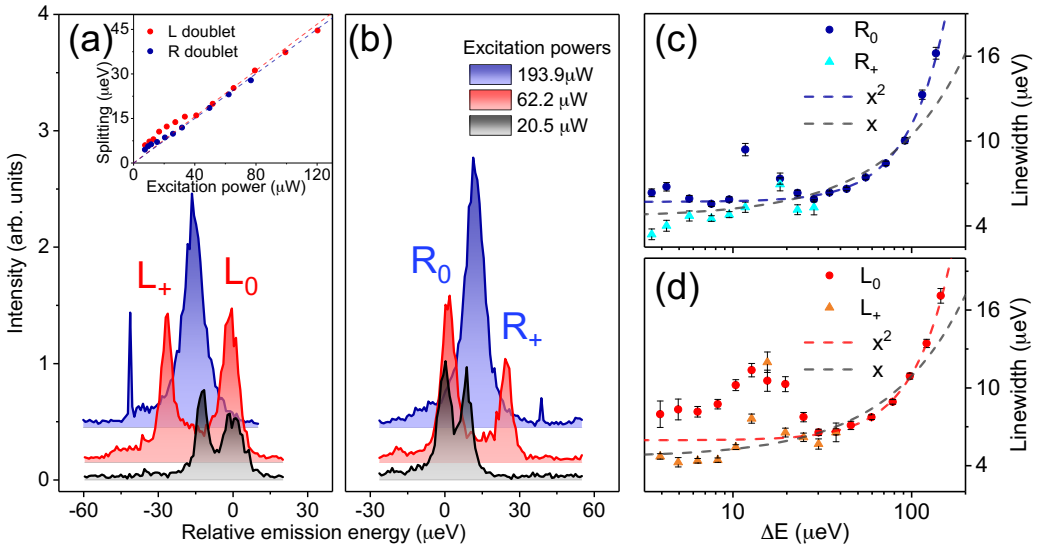

Figure 6.8: (a) Exemplary high resolution spectra of the L doublet for three different excitation powers (21 μW, 62 μW and 194 μW) . The inset shows the doublet splitting as a function of excitation power for both doublets. (b) Exemplary high resolution spectra of the R doublet for different excitation powers. (c) Extracted linewidth of the R doublet as a function of the doublet splitting. (d) Extracted linewidth of the L doublet as a function of the doublet splitting.The fits assume a linear and quadratic power dependency of the linewidth, respectively.

detection setup that we employ for this measurement: The FPI is placed behind the spectrometer which has a spectral resolution of about 30 μeV[6]. Thus a splitting approaching a value of 30 μeV will no longer be focused entirely on the fibre facet that leads to the APD. The extracted values of the splitting is plotted as a function of excitation power in the inset of Fig. 6.8 (a). Again, the splitting grows linearly as a function of the squared Rabi frequency in this power regime confirming the measurements with the spectrometer. From linear fits we obtain slopes of 0.38 $\frac{\mu eV}{\mu W}$ and 0.37 $\frac{\mu eV}{\mu W}$ for the L and R doublet, respectively. Furthermore, for large powers we also observe a shift of the L (R) doublet to lower (higher) energies. We attribute this to a DC Stark shift of the intermediate excitonic levels due to the strong laser field [194].

The linewidth dependence on the excitation power extracted from these measurements is plotted in Fig. 6.8 (c) and (d) and exhibits a more intricate dependency. The minimum emission linewidth is around 4 μeV for the L_0 and R_0 line at very small splittings. For the L_+ and R_+ line, this value is around 7 μeV. Interestingly, we observe a local maximum for a splitting of 15 μeV which is particularly pronounced for the L doublet[7]. For large splittings, we observe for both doublets a clear broadening of the peaks. Despite the lack of a theoretical model[8] and to gain a more qualitative insight into the dephasing mechanism we tentatively fit the data (excluding the local maximum) with a quadratic and linear dependency. The quadratic function reproduces the data remarkably well for large excitation powers. This is in contrast to the linear dependency typical for the broadening of the sidebands of the

[6]Resolution of the grating with 1200 grooves per mm.
[7]The maximum was observed in several independent measurement cycles and a systematic error can thus be be dismissed.
[8]We found no theory in the literature which has explored explicitly the dephasing mechanisms for this experiment.

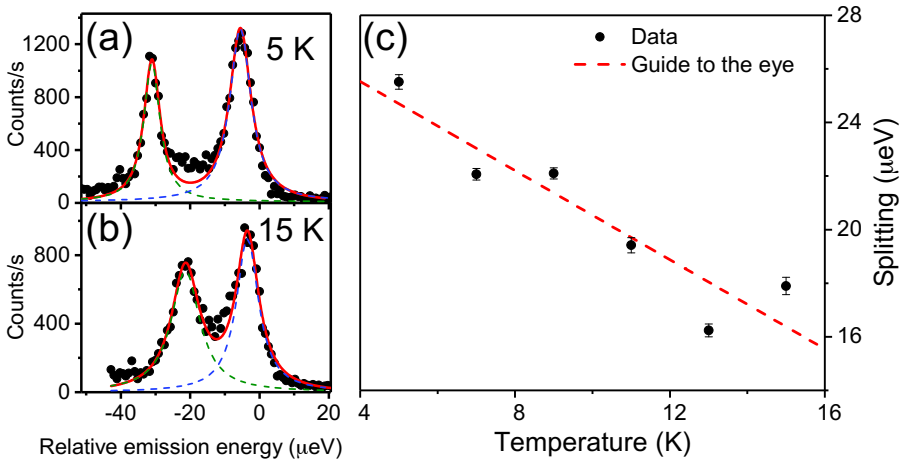

Figure 6.9: (a) High-resolution emission spectrum of the L_+ and L_0 transitions at 5 K.(b) High-resolution emission spectrum of the L_+ and L_0 transitions at 15 K. The red solid line in (a) and (b) is a fit of two independent Lorentzians to the experimental data. (c) Extracted splitting between L_+ and L_0 as a function of the sample temperature. The dashed line is a guide to the eye.

Mollow triplet (cf. section 4.1) [123, 138, 139]. Nevertheless, we would also suspect acoustic phonons to be the main origin of the observed excitation induced dephasing.

To underpin this suspicion and to explore the responsible dephasing mechanism in more detail we also studied the dependency of the splitting on temperature at a fixed excitation power. For neutral excitons in QDs it has been demonstrated that the coupling of the exciton to LA phonons leads to a temperature dependent renormalisation of the Rabi frequency [60]. To study this effect we kept the excitation power constant and recorded the emission spectrum for different temperatures. As is evident from Fig. 6.9 (c), phonons lead similarly as is the case for single-photon transitions in QDs to a renormalisation of the Rabi frequency [60]. Again, a theoretical investigation of this phenomenon still needs to be established and we simply plot the data along with a guide to the eye. The related conclusions are hence preliminary and require a more thorough study.

Two-photon Rabi oscillations in the temporal domain

In the case of the two-level system the emergence of the Mollow triplet in the spectral domain could be intuitively understood as the reflection of the temporal modulation of the population of the excited state. In the same way we can expect to observe coherent oscillations between the ground and biexciton state in our current system. To observe the oscillations of the population of the biexciton state in the temporal domain we use again an EOM which is driven by an electric pulse generator. The trigger signal of the pulse generator serves as a start for our counting electronics while the detection of a photon stops the measurement. In order to select the different spectral lines the light is first passed through a spectrometer and consecutively detected by a SPCM (temporal resolution 40 ps). For the fluorescence emitted in to the exciton state we can observe clear oscillations in the time trace of the fluorescence. Photons emitted into the ground state however show now clear oscillations. This again illustrates that the laser creates a coherent superposition between the ground and biexciton state while the H exciton is not involved. The exciton states are only populated via the radiative cascade from the biexciton leading to a hardly visible oscillation in the fluorescence. This behaviour is also well reproduced qualitatively

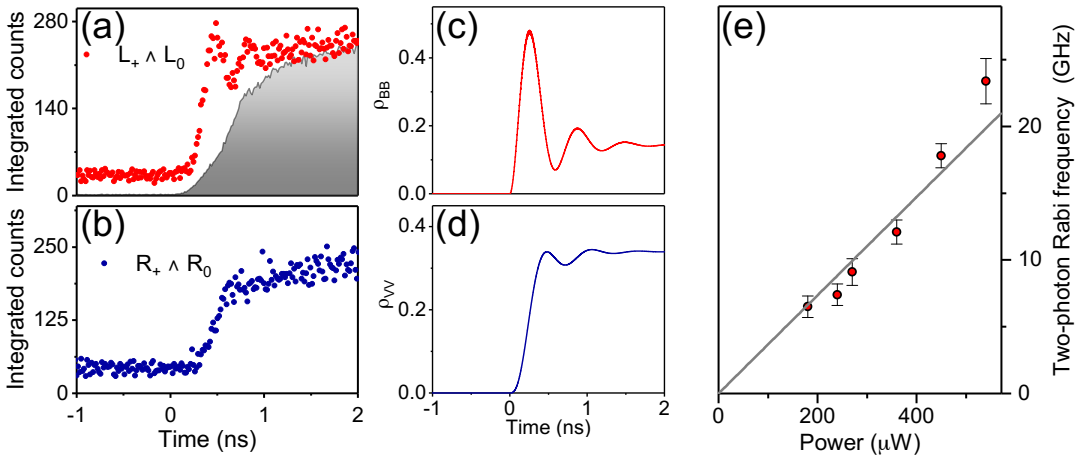

Figure 6.10: (a) Red dots: Time trace of the recorded fluorescence signal of the $L_+ \wedge L_0$ doublet under an excitation with the (rescaled) laser pulse (shaded curve). The excitation power was 550 μW. The signal reveals clear Rabi oscillations. (b) Blue dots: Time trace of the recorded fluorescence signal of the $R_+ \wedge R_0$. The excitation conditions are the same as in (a). The signal reveals no clear oscillations. (c)[(d)] Qualitative simulation of the response of the occupation of the biexciton (exciton) state to an external laser field which is switched on at t=0. (e) Dependence of the oscillation frequency on the applied laser power. A linear function is fit to the data yielding a slope of $(36 \pm 2)\frac{\mathrm{GHz}}{\mathrm{mW}}$. A linear dependence is expected due to the two-photon excitation process [203].

by theory as is shown in Fig. 6.10 (c) and (d). The obvious discrepancies between the experiment and theory are most probably caused by the imperfect pulse shape of the exciting laser. While the theory assumes a laser immediately switched on at time t=0 we only reach the maximum Rabi frequency in our experiments after more than 1 ns (cf. shaded curve in Fig. (a)). Also we have to bear in mind that we simulate the population of the biexciton which is a superposition of the dressed states $|+\rangle$, $|-\rangle$ and $|0\rangle$ [9] But we do not record the L_- photons which also reduces the visibility of the oscillation, an effect which has also been studied for the case of the standard two-level Mollow triplet [186].

It is important to stress that the frequency of the oscillations for these two-photon Rabi oscillations grows linearly with the intensity of the incident light field which we reproduced fairly well with our experiments as is depicted in Fig. 6.10 (e). The deviation is probably again due to the non-ideal pulse shape and also deadjustment of the sample during the measurement. This dependence is again in contrast to the single-photon transition where the Rabi frequency depends linearly on the electric field [203].

Photon-photon correlations

In the previous experiments we have seen that our system is well described by the theory presented in section 2.5. Most strikingly, the coherent interaction here gives rise to six possible transitions of which we could observe four in our experiments.

The remainder of the chapter will now explore the temporal photon-photon correlations of the light emitted by this dressed cascade. This is inspired by earlier work that had been done on the

[9] Interestingly, this superposition, i.e. the admixture of the different states is power dependent.

two-level system or more precisely on the Mollow triplet [204–206]. While the overall statistics of the photons emitted by a TLS is of course subpoissonian it was shown that by selecting different spectral components of the Mollow triplet photon statistics very different to the overall subpoissonian statistics can be distilled [204, 205, 207]. The first experiments conducted with atoms showed that the photons in the opposite sidebands are emitted in a cascade (i.e. time-ordered) which can be reversed by inverting the detuning between laser and the transition. Experiments using excitons in QDs as two-level systems successfully reproduced the results [206]. Additionally, they showed that the time ordering of the emitted photon pairs emitted from opposite sidebands which is present under detuning is removed on resonance. Thus a two-level system can act as a source of highly correlated photon pairs which was also recently exploited to demonstrate Franson interference [208] between photons emitted in this cascade [188].

In the case of the coherently driven cascade there are in principle nine cross correlations between L and R transitions for positive and nine correlations for negative time delays. Of these eighteen correlations, twelve show a bunching while six show an antibunching [10]. Adding all of them yields an exponential decay for the biexciton-exciton detection sequence and an antibunching, or more precisely Rabi oscillations, for the exciton-biexciton detection sequence (cf. Fig. 6.11). This means that the probability to detect an exciton photon right before a biexciton photon is zero while the likelihood to detect a biexciton photon before an exciton photon is increased.

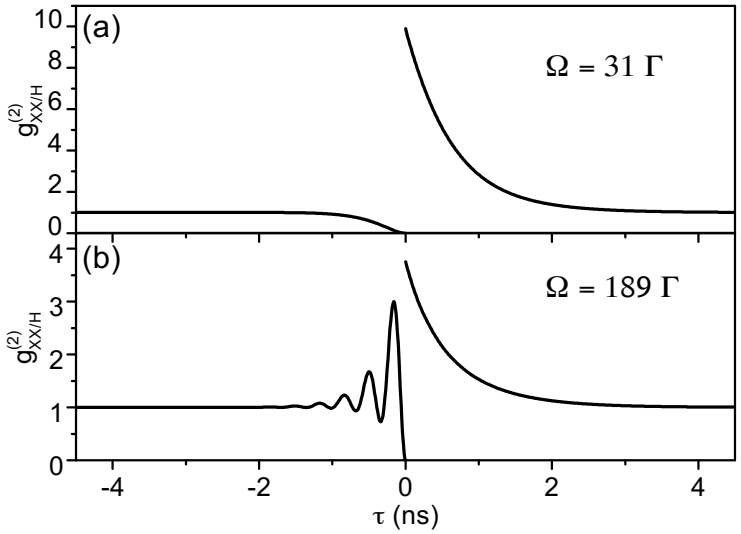

Figure 6.11: Correlation function of the bare $|XX\rangle$-$|H\rangle$ states. (a) For a driving strength of $\Omega = 31\Gamma$ we observe a bunching for positive and an antibunching for negative time delays. (b) Under strong excitation, $\Omega = 189\Gamma$, the bunching for positive time delays persists while for negative time delays Rabi oscillations become visible.

In our experiments we only observe four transitions and thus only eight correlations out of the possible eighteen are accessible to us. Out of these eight correlations two exhibit two bunching and two antibunching behaviour. By selecting different spectral windows in our experiments we will show that we can nevertheless establish or erase time-ordering in the emitted photon pairs.

As a first experiment on the photon statistics of the emitted light field we establish that an individual

[10] The numerically calculated correlations are shown in the appendix.

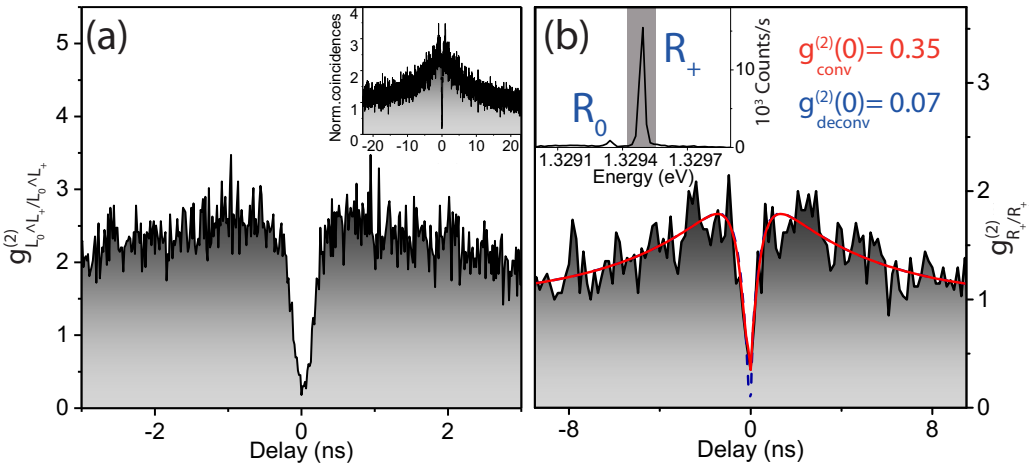

Figure 6.12: (a) Autocorrelation function of L_0 and L_+. The antibunching shows that the final state of both transitions is a single state. Inset: Bunching on a longer time scale can be attributed to blinking of the emitter. (b) Antibunching recorded by selecting only the (detuned) R_+ transition. Inset: Spectrum showing the R doublet detuned from resonance by -52 μeV.

peak of the spectrum consists of a stream of single photons. An intensity autocorrelation function of the photons emitted from the state R_+ (detuned from resonance by -52 μeV) is plotted in Fig. 6.12 (b). We observe clean antibunching for time scales short compared to the lifetime of the emitter and bunching for intermediate time scales. This bunching is again indicative of blinking as in the previous experiments on single-photon transitions. Thus, each spectral component consists of a stream of single photons. The different spectral components thus can act as single-photon sources which are easily tunable via laser detuning and power. Likewise correlating the photons emitted from the states L_0 and L_+ yields a clean, symmetric antibunching (cf. Fig. 6.12 (a)). (The deeper antibunching compared to the previous graph is a purely instrumental effect as the superconducting detectors with a higher temporal resolution were used for this measurement). This further confirms the level scheme and clearly shows that L_0 and L_+ both belong to the same single quantum emitter and decay into one single level.

The previous measurements established that photons emitted from L_0 and L_+ (and R_0 and R_+) are emitted one at a time just as expected from the level scheme depicted in Fig. 6.6 (c). The next experiments will now explore the different photon-photon correlations one is able to extract from the entire system by adjusting the power and frequency of the exciting laser as well as the spectral filter window. For the sake of consistency positive time delays ($\tau > 0$) will correspond to the case that a L photon ($L_0 \wedge L_+$) is detected before an R photon ($R_0 \wedge R_+$) and vice versa for negative time delays.

In Fig. 6.13 (a) we plot a cross-correlation between $L_0 \wedge L_+$ and $R_0 \wedge R_+$ at low excitation powers. For positive time delays we observe a high bunching while for negative time delays we observe an almost flat line at one. This shows while the detection of a L photon heralds the detection of a R photon the inverse is not true. Theory predicts for negative time delays even a slight antibunching for $T_1 > |\tau| > 0$ which we are unable to observe in the experiment which is most likely due to our limited temporal resolution of the Si SPCM (τ_{FWHM} = 550 ps) and pure dephasing which is not included in the model. By increasing the power but leaving the spectral windows in which we correlate the photons unchanged, we now correlate again photons from $L_0 \wedge L_+$ with photons from $R_0 \wedge R_+$.

The obtained data is displayed in Fig. 6.13 (c). Now the bunching is present for negative and positive

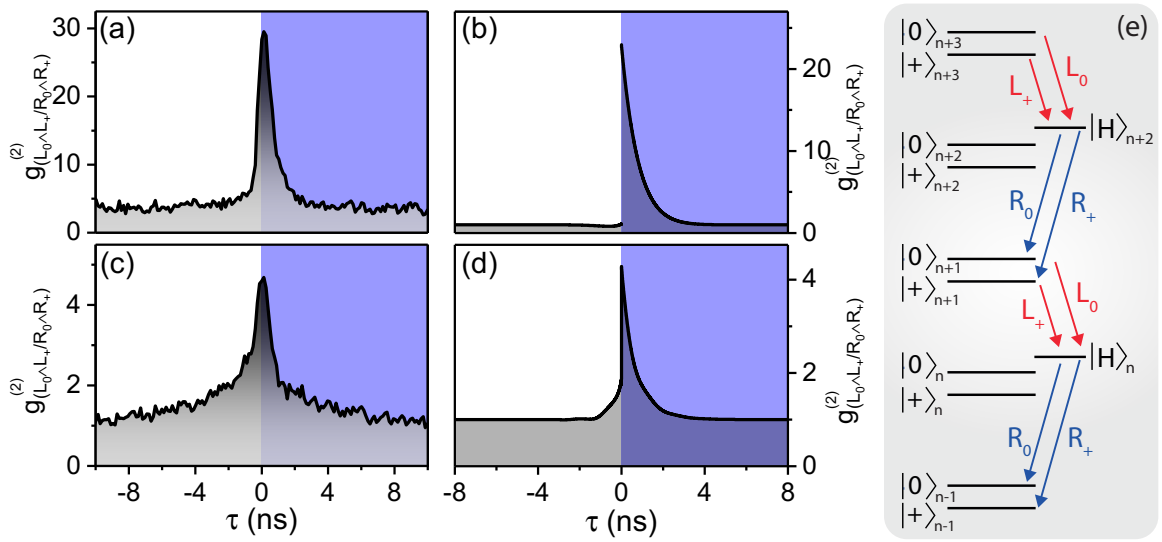

Figure 6.13: (a) Cross correlation function of $L_0 \wedge L_+$ and $R_0 \wedge R_+$ photons. (b) Theoretical correlation function of $L_0 \wedge L_+$ and $R_0 \wedge R_+$ convolved with IRF (τ_{FWHM} = 551 ps). (c) Cross correlation function of L_0 and R_+ photons. The shaded area of the graph indicates positive time delays (d) Theoretical correlation function of L_0 and R_+ convolved with IRF (τ_{FWHM} = 551 ps). (e) Successive photon emission sequence down the dressed states ladder.

delays which means that detection of a $L_0 \wedge L_+$ photon heralds the detection of a $R_0 \wedge R_+$ photon and vice versa. This is also confirmed by theory depicted in Fig. 6.13 (d). Thus, by increasing the power we can evidently manipulate the time-ordering of the emitted photon pairs. We will now underpin this statement by unravelling the theoretical and experimental data. First, we want to recall that we take the biexciton-exciton correlation only partially in the experiment and that we leave out the contribution from the $|-\rangle$ state. Consequently, the photon-photon correlation recorded in the experiment has eight terms and reads

$$g^{(2)}_{L_0\wedge L_+/R_0\wedge R_+} = \frac{1}{4}\left(g^{(2)}_{L_0/R_0} + g^{(2)}_{L_+/R_+} + g^{(2)}_{L_0/R_+} + g^{(2)}_{L_+/R_0}\right) \qquad (\tau > 0) \qquad (6.2a)$$

$$= \frac{1}{4}\left(g^{(2)}_{R_0/L_0} + g^{(2)}_{R_+/L_+} + g^{(2)}_{R_+/L_0} + g^{(2)}_{R_0/L_+}\right) \qquad (\tau < 0)\,. \qquad (6.2b)$$

Equation 6.2a calculates the conditional probability of detecting first a L photon and then a R photon while equation 6.2b describes all the possible detection events for the R-L direction.

Under a certain set of conditions ($\Delta \gg \Omega_V, \Delta \gg \Gamma_{HG}, \frac{\Omega_V^2}{\Delta} \ll \Gamma_{HG}$ [11]) analytical solutions for all eight terms can be derived [197]. These solutions were derived by Alexander Carmele and we state them here for a more thorough understanding of the experimental results. The analytical equation for the experimental cross correlation function on resonance is given by

$$g^{(2)}_{L_0\wedge L_+/R_0\wedge R_+}(\tau) = g^{(2)}_{L_0\wedge L_+/R_0\wedge R_+}(\tau \geq 0) + g^{(2)}_{R_0\wedge R_+/L_0\wedge L_+}(\tau \leq 0)\,, \qquad (6.3)$$

[11] The first two inequalities signify that the biexciton binding energy is large compared to the single-photon Rabi frequency and the radiative decay time. This is fulfilled for our experiments (Δ=3.15 meV, Γ_{HG} = 0.9 μeV, Γ_{BH} = 2.1 μeV), Ω_V = 100 μeV. The third inequality neglects dispersive shifts which limits the validity of the derived equations to medium driving strengths.

where

$$g^{(2)}_{L_0\wedge L_+/R_0\wedge R_+}(\tau \geq 0) = 3 + e^{-2\Gamma\tau} + 2\alpha e^{-\Gamma\tau}[1+\cos(\Omega\tau)]\,, \tag{6.4a}$$

$$g^{(2)}_{R_0\wedge R_+/L_0\wedge L_+}(\tau \leq 0) = 1 + e^{-2\Gamma\tau} - \frac{2\alpha\cos(\Omega\tau)}{1+2\alpha}e^{-\Gamma\tau}\,. \tag{6.4b}$$

Here we introduced the two-photon Rabi frequency $\Omega = \frac{2\Omega_V^2}{\Delta}$ and the dimensionless parameter $\alpha = \frac{\Gamma^2}{\Omega^2}$. Both detection sequences exhibit bunching for τ=0 which is, however, never completely symmetric. As we will show in the following this asymmetry is due to a fundamental difference between the cross-correlation terms $g^{(2)}_{R_+/L_+}$ and $g^{(2)}_{R_0/L_+}$ in equation 6.2b for negative time delays (i.e. the exciton-biexciton detection sequence). We want to generally remark that it is intuitively clear from the level scheme that a L photon always heralds a R photon as they share the H state as a final and initial state, respectively. Consequently, we can only expect to observe an antibunching in the R-L detection sequence.

Due to the large splitting of the doublets at high excitation powers the different contributions to the correlation function can be easily experimentally investigated by adjusting the position of the grating of the spectrometers. First we examine the symmetric correlation function $g^{(2)}_{R_+/L_+}(\tau)$. The analytic solution is

$$g^{(2)}_{R_+/L_+}(\tau) = 2e^{-\Gamma\tau}(1+\cosh(\Gamma\tau)+\alpha[1+\cos(\Omega\tau)]) \qquad (\tau > 0) \tag{6.5a}$$

$$= 1 + 2\frac{1+\alpha}{1+2\alpha}\left[e^{-2\Gamma\tau}\left(1-\frac{1}{2}\frac{1}{1+\alpha}\right) + e^{-\Gamma\tau}\left(1-\frac{\alpha\cos(\Omega\tau)}{1+\alpha}\right)\right] \qquad (\tau < 0)\,. \tag{6.5b}$$

Both detection sequences show a bunching however with a different dependence on the Rabi frequency. While the bunching for $\tau > 0$ can take arbitrarily large values for small Rabi frequencies the opposite detection sequence has a minimal value of 2 for vanishing driving strengths. For large Rabi frequencies both sequences display a bunching of 4 and one can in theory no longer distinguish both detection events. Hence the time-ordering is lifted. In the experiment whose results are shown in Fig. 6.14 (a) we also observe a bunching for both delay directions. In contrast to the theory it is however not symmetric since the correlation function decays faster for $\tau < 0$. This is due to the shorter lifetime of the biexciton compared to the exciton [12]. By adjusting the lifetimes of exciton and biexciton for the simulation we can nicely reproduce the observed effect as is shown in Fig. 6.14 (b). We also note that the correlation function $g^{(2)}_{R_0/L_0}(\tau)$ is identical to the one given in equation 6.5.

Next, we turn to the correlation functions involving two different dressed states, e.g. $g^{(2)}_{L_+/R_0}(\tau)$. The analytic solution is given by

$$g^{(2)}_{L_+/R_0}(\tau) = 2e^{-\Gamma\tau}(1+\cosh(\Gamma\tau)+\alpha[1+\cos(\Omega\tau)]) \qquad (\tau > 0) \tag{6.6a}$$

$$= 1 + \frac{1}{1+2\alpha}\left[e^{-2\Gamma\tau}(1+2\alpha) - 2e^{-\Gamma\tau}(1+\alpha+\alpha\cos(\Omega\tau))\right] \qquad (\tau < 0)\,. \tag{6.6b}$$

For positive time delays this function shows a bunching while for negative time delays this function always exhibits an antibunching. This can be understood as a consequence of the orthogonality of the two involved states $|+\rangle$ and $|0\rangle$ (cf. equations 2.57). Both statements remain true irrespective of the driving strength. We observe this signature of a strictly time-ordered cascade also in our experiments shown in Fig. 6.14 (c). By selecting the lines L_+ and R_0 we observe a bunching for positive time delays and

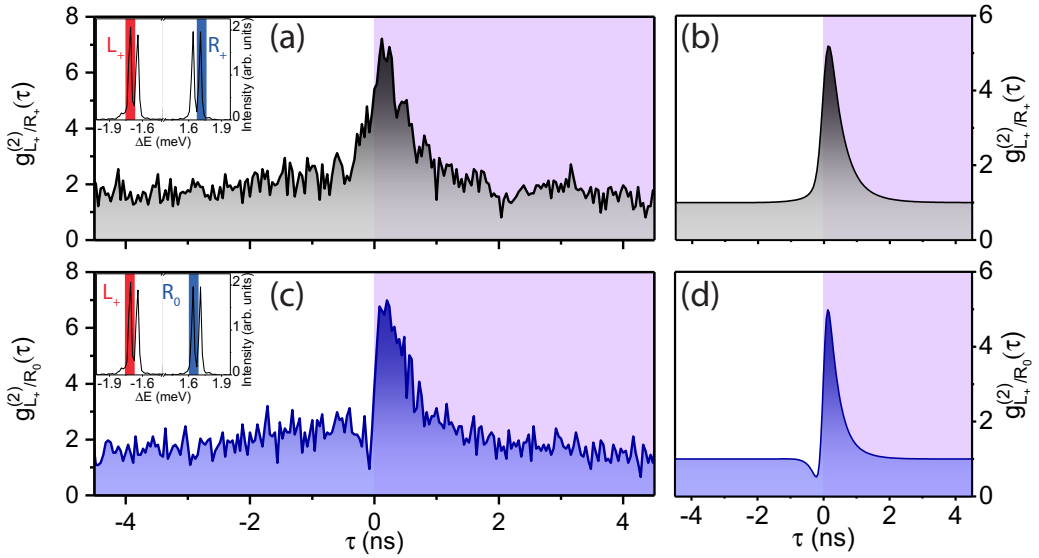

Figure 6.14: (a) Cross correlation function of L_+ and R_+ photons. (b) Theoretical correlation function of L_+ and R_+ according to equation 6.5 convolved with IRF (τ_{FWHM} = 121 ps). (c) Cross correlation function of L_+ and R_0 photons. The shaded area of the graph indicates positive time delays. Inset: Spectrum highlighting transitions which are investigated. (d) Theoretical correlation function of L_+ and R_0 according to equation 6.6 convolved with IRF (τ_{FWHM} = 121 ps).

an antibunching for negative time delays in qualitative agreement with the simulations in Fig. 6.14 (d).

Both experiments nicely confirm the theoretical predictions. The detection of a L photon always heralds the detection of a R photon as is also naively expected from the extended level scheme of the ladder in Fig. 6.13 (e). Conversely, the detection of a R photon only heralds the detection of a L photon if both transitions involve the same dressed state. If, however, they involve different dressed states one can be sure that the detection of a R photon won't directly be followed by the detection of a L photon.

So far the investigation was restricted to the case of the correlations in the case of a strict resonantly driven cascade ($\omega_L = \omega + \Delta E_B/2$). Drawing again upon the analogy to the Mollow triplet we now turn to correlations in a cascade driven slightly off resonance. As we discussed in section 2.5 there is no analytic solution for the eigensystem of the Hamiltonian under detuning. Consequently, it is also not possible to derive an analytic solution for the intensity cross-correlation function under detuning and we will only present the experimentally obtained data in the following [13]. We detuned the laser from the two-photon resonance by -62 μeV and recorded the cross-correlation function between L_0 and R_0. Figure 6.15 (a) shows the experimental data while the inset highlights the correlated transitions which have a significantly different oscillator strength under detuning. As in the resonant case we observe again a bunching for positive time delays. This means that once a L_+ is detected the probability to detect a R_+ photon is increased. For negative time delays neither a bunching nor an antibunching is visible (apart from the bunching on the intermediate time scale attributed to blinking). Here, the oscillator strength of the L_+ transition is so small compared to the one of the R_+ transition that the conditional detection of this sequence becomes uncorrelated, i.e. Poissonian. By correlating the two

[12] The photons from the R doublet decay from the bare $|H\rangle$ state.

[13] In recent years, Laussy and coworkers developed a numerical approach to calculate the intensity auto- and cross-correlation function for arbitrary spectral filters in the emission spectrum of a quantum system [209, 210] which would allow for the simulation of the data presented in Fig. 6.15.

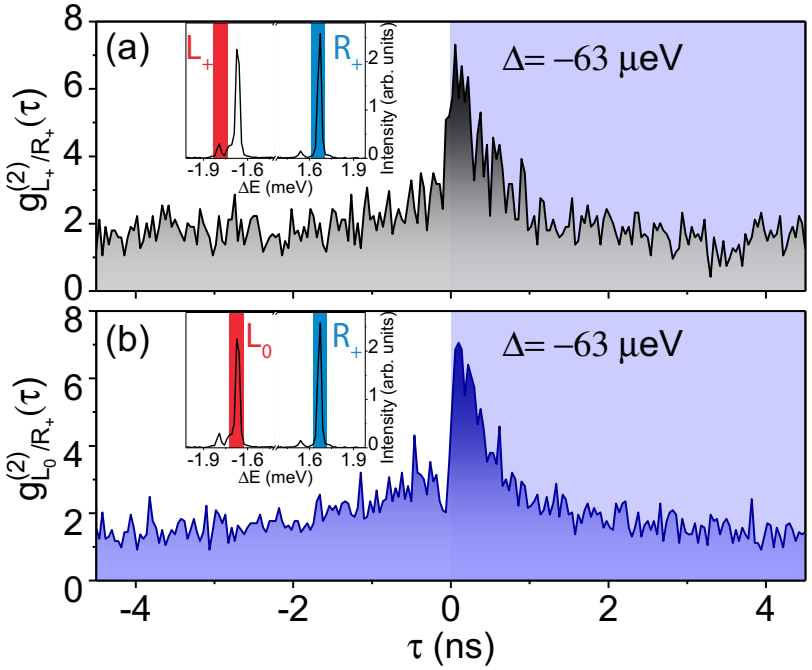

Figure 6.15: (a) Cross correlation function of L_+ and R_+ photons. (b) Cross correlation function of L_0 and R_+ photons. The shaded area of the graph indicates positive time delays. Inset: Spectrum highlighting transitions which are investigated.

strong lines L_+ and R_0 in the detuned emission spectrum, we obtained the plot in Fig. 6.15 (b). The bunching for positive time delays is necessarily observed again. Interestingly, the correlation function exhibits an antibunching for negative time delays which was also observed in the resonant case. This signifies that while the detuning changes the admixtures of the bare states the two states $|+\rangle$ and $|0\rangle$ remain orthogonal.

6.3 Summary of chapter 6

In this chapter we primarily investigated the coherent interaction between the biexciton cascade and a two-photon resonant light field. Just like in the case of a TLS the coherent excitation of the system gives rise to a wealth of phenomena which are inaccessible under non-resonant excitation. We observe the emergence of dressed states under strong excitation which is fully described by the theory presented in section 2.5. Going beyond the theory we then examine the dependence of the linewidth of the dressed states on the excitation power. Here, we find that for large powers the linewidth increases quadratically with the excitation power. This is in contrast to the standard TLS Mollow triplet where we observed a linear dependence of the linewidth of the sidebands on the excitation power. Subsequently, we evidenced the coherent two-photon interaction in the temporal domain by observing Rabi oscillations of the biexciton. We found in agreement with theory that in this two-photon process the Rabi frequency depends linearly on the excitation power. In the final experiments we showed that the time-ordering of the emitted photons can be steered by selecting different spectral windows of the emission spectrum. In particular, we can easily change between time-ordered and time-unordered photon pairs in our system which renders it an ideal testbed for any time-bin critical experiments.

The presented experiments only investigated photon-photon correlations. In a future experiment,

one could investigate pair-pair correlations. On resonance, we assume that our system emits photon pairs in a random succession. But, for example, under negative detuning the detection of a L_+/R_0 photon pair should herald the detection of a R_0/L_+ photon pair. In the experiment such a correlation would be possible to evidence via measurements of the conditional pair detection, i.e. $g^{(4)}(\tau)$.

7

Conclusion & outlook

We hope to have convinced the reader of this thesis that even after more than 40 years of research the TLS remains an intriguing subject to study in the laboratory. As we have seen in the chapters 5 and 4 the basic signatures of the interaction between a coherent, resonant light field and a TLS such as the Mollow triplet are nowadays routinely observable using a semiconductor QD as TLS. Of course, on a closer look the experiments using QDs often reveal that a simple TLS does not suffice to describe the experimental data. For a more accurate description the interaction with the solid-state environment needs to be accounted for.

In chapter 4 we discussed such an effect by observing the power-dependent broadening of the Mollow sidebands due to photons in a SCQD. While the experiments showed that it is possible to obtain single photons from these SCQDs further improvement of the QD devices is needed for indistinguishable photons. The interaction between TLS and solid-state environment was even more pronounced in the experiments on photocurrent spectroscopy. The un/charging of a hole gas lead here to a pronounced hysteresis. In future experiments side-excitation could be used to circumvent the limitations imposed by the cavity in the top-excitation scheme. Despite these marked effects of the environment we could nevertheless observe Rabi oscillations under pulsed excitation.

We started chapter 5 by discussing the Wigner time delay. Again, the presence of pure dephasing in our TLS lead to stark deviations from the results expected for an isolated TLS. We observed that due to incoherent scattering the total fluorescence signal is stronger delayed than the coherent response of the system. Subsequently, we investigated the influence of thermal photon statistics on the response of a TLS. We contrasted and compared the results to the usual coherent excitation. The experimental findings were largely in agreement with theoretical predictions which had predicted for example the vanishing of the Mollow sidebands under thermal excitation. Experiments such as these where the photon statistics of the exciting light field is used a degree of freedom can also be extended to non-classical photon statistics. However, such quantum cascaded setups where two or more TLSs interact sequentially via photons currently still suffer from low photon extraction (and accordingly in-coupling) efficiencies.

In chapter 6 we studied the coherent light-matter interaction in a four-level system. Evidently, the experiments drew a lot of inspiration from experiments which had been performed on TLSs. At the same time, we had to be careful not to see analogies between the two systems where there were none. In our experiments we saw in particular that the time-ordering of the emitted photons could be established or erased by selecting different spectral windows. Side-excitation schemes would allow in principle to access the entire spectrum in both polarisations which could be used to realise an entanglement across generation scheme [211].

The presented results illustrate that many different quantum optical phenomena exploiting the coherence induced by a resonant, coherent light field can be readily studied using semiconductor QDs as two- or multi-level system. In particular, the resonant excitation of the ladder system offers a lot of physics which has been hitherto unexplored experimentally.

Bibliography

[1] A. Acín et al. 'The European Quantum Technologies Roadmap'. In: (Dec. 2017), pp. 1–30. arXiv: 1712.03773.

[2] L. Goldstein et al. 'Growth by molecular beam epitaxy and characterization of InAs/GaAs strained-layer superlattices'. In: *Appl. Phys. Lett.* 47.10 (Nov. 1985), pp. 1099–1101. DOI: 10.1063/1.96342. arXiv: arXiv:1011.1669v3.

[3] P. Michler et al. 'Quantum correlation among photons from a single quantum dot at room temperature'. In: *Nature* 406.6799 (Aug. 2000), pp. 968–970. DOI: 10.1038/35023100.

[4] P. Michler et al. 'A Quantum Dot Single-Photon Turnstile Device'. In: *Science (80-.).* 290.5500 (Dec. 2000), pp. 2282–2285. DOI: 10.1126/science.290.5500.2282.

[5] F. Seilmeier et al. 'Optical Thermometry of an Electron Reservoir Coupled to a Single Quantum Dot in the Millikelvin Range'. In: *Phys. Rev. Appl.* 2.2 (Aug. 2014), p. 024002. DOI: 10.1103/PhysRevApplied.2.024002.

[6] K. De Greve et al. 'Quantum-dot spin–photon entanglement via frequency downconversion to telecom wavelength'. In: *Nature* 491.7424 (2012), pp. 421–425. DOI: 10.1038/nature11577.

[7] E. Schlottmann et al. 'Injection Locking of Quantum-Dot Microlasers Operating in the Few-Photon Regime'. In: *Phys. Rev. Appl.* 6.4 (Oct. 2016), p. 044023. DOI: 10.1103/PhysRevApplied.6.044023. arXiv: 1604.02817.

[8] Y. He et al. 'Time-Bin-Encoded Boson Sampling with a Single-Photon Device'. In: *Phys. Rev. Lett.* 118.19 (May 2017), p. 190501. DOI: 10.1103/PhysRevLett.118.190501. arXiv: 1603.04127.

[9] H. Wang et al. 'High-efficiency multiphoton boson sampling'. In: *Nat. Photonics* 11.6 (May 2017), pp. 361–365. DOI: 10.1038/nphoton.2017.63.

[10] J. C. Loredo et al. 'Boson Sampling with Single-Photon Fock States from a Bright Solid-State Source'. In: *Phys. Rev. Lett.* 118.13 (Mar. 2017), p. 130503. DOI: 10.1103/PhysRevLett.118.130503. arXiv: 1603.00054.

[11] X. Ding et al. 'On-Demand Single Photons with High Extraction Efficiency and Near-Unity Indistinguishability from a Resonantly Driven Quantum Dot in a Micropillar'. In: *Phys. Rev. Lett.* 116.2 (Jan. 2016), p. 020401. DOI: 10.1103/PhysRevLett.116.020401. arXiv: 1601.00284.

[12] J. C. Loredo et al. 'Scalable performance in solid-state single-photon sources'. In: *Optica* 3.4 (Apr. 2016), p. 433. DOI: 10.1364/OPTICA.3.000433. arXiv: 1601.00654.

[13] N. Somaschi et al. 'Near optimal single photon sources in the solid state'. In: *Nat. Photonics* 10.2 (2015), pp. 1–6. DOI: 10.1038/nphoton.2016.23. arXiv: 1510.06499.

[14] P. Senellart et al. 'High-performance semiconductor quantum-dot single-photon sources'. In: *Nat. Nanotechnol.* 12.11 (Nov. 2017), pp. 1026–1039. DOI: 10.1038/nnano.2017.218.

[15] O. Benson et al. 'Regulated and Entangled Photons from a Single Quantum Dot'. In: *Phys. Rev. Lett.* 84.11 (Mar. 2000), pp. 2513–2516. DOI: 10.1103/PhysRevLett.84.2513.

[16] M. Müller et al. 'On-demand generation of indistinguishable polarization-entangled photon pairs'. In: *Nat. Photonics* 8.3 (Feb. 2014), pp. 224–228. DOI: 10.1038/nphoton.2013.377.

[17] R. Winik et al. 'On-demand source of maximally entangled photon pairs using the biexciton-exciton radiative cascade'. In: *Phys. Rev. B* 95.23 (June 2017), p. 235435. DOI: 10.1103/PhysRevB.95.235435. arXiv: 1703.04380.

[18] S. Bounouar et al. 'Generation of maximally entangled states and coherent control in quantum dot microlenses'. In: *Appl. Phys. Lett.* 112.15 (Apr. 2018), p. 153107. DOI: 10.1063/1.5020242.

[19] T. Huber et al. 'Polarization entangled photons from quantum dots embedded in nanowires'. In: *Nano Lett.* 14.12 (2014), pp. 7107–7114. DOI: 10.1021/nl503581d. arXiv: 1405.3765.

[20] M. A. M. Versteegh et al. 'Observation of strongly entangled photon pairs from a nanowire quantum dot'. In: *Nat. Commun.* 5 (Oct. 2014), p. 5298. DOI: 10.1038/ncomms6298.

[21] R. Trotta et al. 'Highly Entangled Photons from Hybrid Piezoelectric-Semiconductor Quantum Dot Devices'. In: *Nano Lett.* 14.6 (June 2014), pp. 3439–3444. DOI: 10.1021/nl500968k.

[22] H. M. Meyer et al. 'Direct Photonic Coupling of a Semiconductor Quantum Dot and a Trapped Ion'. In: *Phys. Rev. Lett.* 114.12 (Mar. 2015), p. 123001. DOI: 10.1103/PhysRevLett.114.123001.

[23] J. Wolters et al. 'Simple Atomic Quantum Memory Suitable for Semiconductor Quantum Dot Single Photons'. In: *Phys. Rev. Lett.* 119.6 (Aug. 2017), p. 060502. DOI: 10.1103/PhysRevLett.119.060502. arXiv: 1703.00489.

[24] L. Béguin et al. 'On-demand semiconductor source of 780-nm single photons with controlled temporal wave packets'. In: *Phys. Rev. B* 97.20 (May 2018), p. 205304. DOI: 10.1103/PhysRevB.97.205304. arXiv: 1710.02490.

[25] K. W. Murch et al. 'Reduction of the radiative decay of atomic coherence in squeezed vacuum'. In: *Nature* 499.7456 (July 2013), pp. 62–65. DOI: 10.1038/nature12264.

[26] D. M. Toyli et al. 'Resonance fluorescence from an artificial atom in squeezed vacuum'. In: *Phys. Rev. X* 6.3 (2016), pp. 1–13. DOI: 10.1103/PhysRevX.6.031004. arXiv: 1602.03240.

[27] J. P. Reithmaier et al. 'Strong coupling in a single quantum dot-semiconductor microcavity system.' In: *Nature* 432.7014 (Nov. 2004), pp. 197–200. DOI: 10.1038/nature02969.

[28] C. H. H. Schulte et al. 'Quadrature squeezed photons from a two-level system'. In: *Nature* 525.7568 (Aug. 2015), pp. 222–225. DOI: 10.1038/nature14868. arXiv: 1506.06827.

[29] A. Garg. *Classical electromagnetism in a nushell*. Princeton University Press, 2012.

[30] G. Grynberg et al. *Introduction to Quantum Optics*. Cambridge University Press, 2010.

[31] A. Einstein. 'Über einen die Erzeugung und Verwandlung des Lichtes betreffenden heuristischen Gesichtspunkt'. In: *Ann. Phys.* 322.6 (1905), pp. 132–148. DOI: 10.1002/andp.19053220607. arXiv: arXiv:1011.1669v3.

[32] H. J. Kimble et al. 'Photon Antibunching in Resonance Fluorescence'. In: *Phys. Rev. Lett.* 39.11 (Sept. 1977), pp. 691–695. DOI: 10.1103/PhysRevLett.39.691. arXiv: arXiv:1011.1669v3.

[33] R. H. BROWN et al. 'Correlation between Photons in two Coherent Beams of Light'. In: *Nature* 177.4497 (Jan. 1956), pp. 27–29. DOI: 10.1038/177027a0.

[34] B. Stiller et al. 'Temporal and spectral properties of quantum light'. In: (Nov. 2014), pp. 1–20. arXiv: 1411.3765.

[35] J.-W. Pan et al. 'Multiphoton entanglement and interferometry'. In: *Rev. Mod. Phys.* 84.2 (May 2012), pp. 777–838. DOI: 10.1103/RevModPhys.84.777.

[36] R. Loudon. *The Quantum Theory Of Light*. Third. Oxford University Press: Oxford University Press, Sept. 2001.

[37] S. Haroche et al. *Exploring the Quantum*. Oxford University Press, Aug. 2006. DOI: 10.1093/acprof:oso/9780198509141.001.0001.

[38] R. Horodecki et al. 'Quantum entanglement'. In: *Rev. Mod. Phys.* 81.2 (June 2009), pp. 865–942. DOI: 10.1103/RevModPhys.81.865. arXiv: 0702225 [quant-ph].

[39] A. I. Lvovsky et al. 'Quantum State Reconstruction of the Single-Photon Fock State'. In: *Phys. Rev. Lett.* 87.5 (2001), p. 050402. DOI: 10.1103/PhysRevLett.87.050402. arXiv: 0101051 [quant-ph].

[40] A. Ourjoumtsev et al. 'Quantum homodyne tomography of a two-photon fock state'. In: *Phys. Rev. Lett.* 96.21 (2006), pp. 1–4. DOI: 10.1103/PhysRevLett.96.213601. arXiv: 0603284 [quant-ph].

[41] T. Heindel et al. 'A bright triggered twin-photon source in the solid state'. In: *Nat. Commun.* 8 (2016), pp. 1–7. DOI: 10.1038/ncomms14870. arXiv: 1608.02768.

[42] A. Migdall et al. *Single-photon generation and detection*. Vol. 36. Academic Press, 2013. DOI: 10.1016/S1079-4042(09)04212-X.

[43] I. I. Rabi. 'Space Quantization in a Gyrating Magnetic Field'. In: *Phys. Rev.* 51.8 (Apr. 1937), pp. 652–654. DOI: 10.1103/PhysRev.51.652.

[44] I. I. Rabi et al. 'A New Method of Measuring Nuclear Magnetic Moment'. In: *Phys. Rev.* 53.4 (Feb. 1938), pp. 318–318. DOI: 10.1103/PhysRev.53.318.

[45] F. Bloch et al. 'Nuclear Induction'. In: *Phys. Rev.* 69.3-4 (Feb. 1946), pp. 127–127. DOI: 10.1103/PhysRev.69.127.

[46] E. M. Purcell et al. 'Resonance Absorption by Nuclear Magnetic Moments in a Solid'. In: *Phys. Rev.* 69.1-2 (Jan. 1946), pp. 37–38. DOI: 10.1103/PhysRev.69.37.

[47] H. Walther. 'Resonance Fluorescence of Two-Level Atoms'. In: *Adv. At. Mol. Opt. Phys.* Vol. 51. 05. Elsevier Masson SAS, 2005, pp. 239–272. DOI: 10.1016/S1049-250X(05)51016-4.

[48] S. Aaronson. *Quantum Computing Since Democritus*. Cambridge University Press, 2013.

[49] M. Nielsen et al. *Quantum Computation and Quantum Information*. Camebridge: Cambridge University Press, 2010.

[50] H. Carmichael. *An open systems approach to quantum optics*. Springer Berlin Heidelberg, 1993.

[51] L. Allen et al. *Optical resonance and two-level atoms*. Dover, 1975.

[52] J. Wolters. *Integrated Quantum Hybrid Systems*. Pan Stanford, 2015, p. 292.

[53] S. A. Aljunid et al. 'Phase shift of a weak coherent beam induced by a single atom'. In: *Phys. Rev. Lett.* 103.15 (2009), pp. 1–4. DOI: 10.1103/PhysRevLett.103.153601. arXiv: 0905.3734.

[54] M. Sondermann et al. 'The phase shift induced by a single atom in free space'. In: *J. Eur. Opt. Soc. Rapid Publ.* 8 (2013), p. 13052. DOI: 10.2971/jeos.2013.13052. arXiv: arXiv:1306.2804v1.

[55] D. A. Steck. 'Quantum and Atom Optics'. In: (2008).

[56] C. Gerry et al. *Introductory Quantum Optics*. 2004.

[57] C. Cohen-Tannoudji et al. *Atom-Photon Interactions: Basic Processes and Applications*. WILEY-VCH Verlag, 2004.

[58] H. S. Nguyen et al. 'Ultra-coherent single photon source'. In: *Appl. Phys. Lett.* 99.26 (2011). DOI: 10.1063/1.3672034. arXiv: arXiv:1111.1621v1.

[59] S. Kreinberg et al. 'Quantum-optical spectroscopy of a two-level system using an electrically driven micropillar laser as a resonant excitation source'. In: *Light Sci. Appl.* 7.1 (Dec. 2018), p. 41. DOI: 10.1038/s41377-018-0045-6. arXiv: 1711.09705.

[60] Y.-J. Wei et al. 'Temperature-Dependent Mollow Triplet Spectra from a Single Quantum Dot: Rabi Frequency Renormalization and Sideband Linewidth Insensitivity'. In: *Phys. Rev. Lett.* 113.9 (Aug. 2014), p. 097401. DOI: 10.1103/PhysRevLett.113.097401.

[61] C. Cohen-Tannoudji et al. 'Dressed-atom description of resonance fluorescence and absorption spectra of a multi-level atom in an intense laser beam'. In: *J. Phys. B At. Mol. Phys.* 10.3 (Feb. 1977), pp. 345–363. DOI: 10.1088/0022-3700/10/3/005.

[62] P. Meystre et al. *Elements of Quantum Optics*. 4th ed. Vol. 1. Springer Berlin Heidelberg New York, 2007.

[63] J. P. Marangos. 'Electromagnetically induced transparency'. In: *J. Mod. Opt.* 45.3 (Mar. 1998), pp. 471–503. DOI: 10.1080/09500349808231909.

[64] M. Fleischhauer et al. 'Electromagnetically induced transparency: Optics in coherent media'. In: *Rev. Mod. Phys.* 77.2 (July 2005), pp. 633–673. DOI: 10.1103/RevModPhys.77.633.

[65] A. Aspect et al. 'Experimental Realization of Einstein-Podolsky-Rosen-Bohm Gedankenexperiment : A New Violation of Bell's Inequalities'. In: *Phys. Rev. Lett.* 49.2 (July 1982), pp. 91–94. DOI: 10.1103/PhysRevLett.49.91.

[66] M. Göppert-Mayer. 'Über Elementarakte mit zwei Quantensprüngen'. In: *Ann. Phys.* 401.3 (1931), pp. 273–294. DOI: 10.1002/andp.19314010303. arXiv: 0402594v3[arXiv:cond-mat].

[67] I. Aharonovich et al. 'Solid-state single-photon emitters'. In: *Nat. Photonics* 10.10 (Sept. 2016), pp. 631–641. DOI: 10.1038/nphoton.2016.186.

[68] F. Jelezko et al. 'Single defect centres in diamond: A review'. In: *Phys. status solidi* 203.13 (Oct. 2006), pp. 3207–3225. DOI: 10.1002/pssa.200671403.

[69] J. Wolters et al. 'Quantum Zeno phenomenon on a single solid-state spin'. In: *Phys. Rev. A* 88.2 (Aug. 2013), p. 020101. DOI: 10.1103/PhysRevA.88.020101.

[70] P. Michler. *Single semiconductor quantum dots*. Springer Berlin Heidelberg, 2009.

[71] A. J. Shields. 'Semiconductor quantum light sources'. In: *Nat. Photonics* 1.4 (Apr. 2007), pp. 215–223. DOI: 10.1038/nphoton.2007.46. arXiv: 0704.0403.

[72] M. N. Makhonin et al. 'Waveguide Coupled Resonance Fluorescence from On-Chip Quantum Emitter'. In: *Nano Lett.* 14.12 (Dec. 2014), pp. 6997–7002. DOI: 10.1021/nl5032937.

[73] U. W. Pohl. *Epitaxy of Semiconductors*. Graduate Texts in Physics. Berlin, Heidelberg: Springer Berlin Heidelberg, 2013, p. 213. DOI: 10.1007/978-3-642-32970-8.

[74] E. Poem et al. 'Accessing the dark exciton with light'. In: *Nat. Phys.* 6.12 (Dec. 2010), pp. 993–997. DOI: 10.1038/nphys1812.

[75] I. Schwartz et al. 'Deterministic generation of a cluster state of entangled photons'. In: *Science (80-.).* 354.6311 (Oct. 2016), pp. 434–437. DOI: 10.1126/science.aah4758. arXiv: 1606.07492.

[76] T. Heindel et al. 'Accessing the dark exciton spin in deterministic quantum-dot microlenses'. In: *APL Photonics* 2.12 (Dec. 2017), p. 121303. DOI: 10.1063/1.5004147. arXiv: 1706.05164.

[77] W. Hartig et al. 'Study of the frequency distribution of the fluorescent light induced by monochromatic radiation'. In: *Zeitschrift für Phys. A Atoms Nucl.* 278.3 (Sept. 1976), pp. 205–210. DOI: 10.1007/BF01409169.

[78] R. E. Grove et al. 'Measurement of the spectrum of resonance fluorescence from a two-level atom in an intense monochromatic field'. In: *Phys. Rev. A* 15.1 (Jan. 1977), pp. 227–233. DOI: 10.1103/PhysRevA.15.227.

[79] A. Muller et al. 'Resonance Fluorescence from a Coherently Driven Semiconductor Quantum Dot in a Cavity'. In: *Phys. Rev. Lett.* 99.18 (Nov. 2007), p. 187402. DOI: 10.1103/PhysRevLett.99.187402.

[80] E. B. Flagg et al. 'Resonantly driven coherent oscillations in a solid-state quantum emitter'. In: *Nat. Phys.* 5.3 (Mar. 2009), pp. 203–207. DOI: 10.1038/nphys1184.

[81] N. Vamivakas et al. 'Spin-resolved quantum-dot resonance fluorescence'. In: *Nat. Phys.* 5.3 (Mar. 2009), pp. 198–202. DOI: 10.1038/nphys1182.

[82] R. Melet et al. 'Resonant excitonic emission of a single quantum dot in the Rabi regime'. In: *Phys. Rev. B* 78.7 (Aug. 2008), p. 073301. DOI: 10.1103/PhysRevB.78.073301.

[83] L. Novotny et al. *Principles of nano-optics*. Cambridge University Press, 2006.

[84] A. Zrenner et al. 'Coherent properties of a two-level system based on a quantum-dot photodiode'. In: *Nature* 418.6898 (Aug. 2002), pp. 612–614. DOI: 10.1038/nature00912.

[85] A. J. Ramsay et al. 'Damping of Exciton Rabi Rotations by Acoustic Phonons in Optically Excited <math display="inline"> <mi>InGaAs</mi> <mo>/</mo> <mi>GaAs</mi> </math> Quantum Dots'. In: *Phys. Rev. Lett.* 104.1 (Jan. 2010), p. 017402. DOI: 10.1103/PhysRevLett.104.017402.

[86] A. J. Ramsay et al. 'Phonon-Induced Rabi-Frequency Renormalization of Optically Driven Single InGaAs/GaAs Quantum Dots'. In: *Phys. Rev. Lett.* 105.17 (Oct. 2010), p. 177402. DOI: 10.1103/PhysRevLett.105.177402.

[87] P. Gold et al. 'Single quantum dot photocurrent spectroscopy in the cavity quantum electrodynamics regime'. In: *Phys. Rev. B* 86.16 (Oct. 2012), p. 161301. DOI: 10.1103/PhysRevB.86.161301.

[88] A. J. Ramsay. 'A review of the coherent optical control of the exciton and spin states of semiconductor quantum dots'. In: *Semicond. Sci. Technol.* 25.10 (Oct. 2010), p. 103001. DOI: 10.1088/0268-1242/25/10/103001.

[89] D. Drung et al. 'Ultrastable low-noise current amplifier : A novel device for measuring small electric currents with high accuracy Ultrastable low-noise current amplifier : A novel device for measuring small electric currents with high accuracy'. In: 024703.2015 (2016), pp. 1–11. DOI: 10.1063/1.4907358.

[90] C. Krause et al. 'Measurement of sub-picoampere direct currents with uncertainties below ten attoamperes'. In: *Rev. Sci. Instrum.* 88.2 (Feb. 2017), p. 024711. DOI: 10.1063/1.4975826.

[91] T. Heindel et al. 'Electrically driven quantum dot-micropillar single photon source with 34 percent overall efficiency'. In: *Appl. Phys. Lett.* 96.1 (Jan. 2010), p. 011107. DOI: 10.1063/1.3284514.

[92] P. W. Fry et al. 'Electric-field-dependent carrier capture and escape in self-assembled InAs/GaAs quantum dots'. In: *Appl. Phys. Lett.* 77.26 (2000), pp. 4344–4346. DOI: 10.1063/1.1334363.

[93] P. Gold. 'Quantenpunkt-Mikroresonatoren als Bausteine für die Quantenkommunikation'. PhD thesis. Universität Würzburg, 2014, p. 143.

[94] S. L. Campbell et al. 'A Fermi-degenerate three-dimensional optical lattice clock'. In: *Science (80-.).* 358.6359 (Oct. 2017), pp. 90–94. DOI: 10.1126/science.aam5538. arXiv: arXiv:1702.01210v1.

[95] F. Riehle. 'Optical clock networks'. In: *Nat. Photonics* 11.1 (Jan. 2017), pp. 25–31. DOI: 10.1038/nphoton.2016.235.

[96] A. D. Ludlow et al. 'Optical atomic clocks'. In: *Rev. Mod. Phys.* 87.2 (June 2015), pp. 637–701. DOI: 10.1103/RevModPhys.87.637. arXiv: 1407.3493.

[97] N. Poli et al. 'Optical atomic clocks'. In: *Riv. del Nuovo Cim.* 36 (2013), pp. 555–624. DOI: 10.1393/ncr/i2013-10095-x. arXiv: 1407.3493.

[98] H. M. Wiseman. 'How many principles does it take to change a light bulb…into a laser?' In: *Phys. Scr.* 91.3 (Mar. 2016), p. 033001. DOI: 10.1088/0031-8949/91/3/033001. arXiv: 1607.03647.

[99] H. S. Nguyen et al. 'Optically Gated Resonant Emission of Single Quantum Dots'. In: *Phys. Rev. Lett.* 108.5 (Jan. 2012), p. 057401. DOI: 10.1103/PhysRevLett.108.057401.

[100] D. Chen et al. 'Characterization of the local charge environment of a single quantum dot via resonance fluorescence'. In: *Phys. Rev. B* 93.11 (Mar. 2016), p. 115307. DOI: 10.1103/PhysRevB.93.115307.

[101] H. Nguyen et al. 'Photoneutralization and slow capture of carriers in quantum dots probed by resonant excitation spectroscopy'. In: *Phys. Rev. B* 87.11 (Mar. 2013), p. 115305. DOI: 10.1103/PhysRevB.87.115305.

[102] W. Martienssen et al. 'Coherence and Fluctuations in Light Beams'. In: *Am. J. Phys.* 32.12 (Dec. 1964), pp. 919–926. DOI: 10.1119/1.1970023.

[103] W. Martienssen et al. 'Intensity Fluctuations in Light Beams with Several Degrees of Freedom'. In: *Phys. Rev. Lett.* 16.12 (Mar. 1966), pp. 531–533. DOI: 10.1103/PhysRevLett.16.531.

[104] F. T. Arecchi. 'Measurement of the Statistical Distribution of Gaussian and Laser Sources'. In: *Phys. Rev. Lett.* 15.24 (Dec. 1965), pp. 912–916. DOI: 10.1103/PhysRevLett.15.912.

[105] D. Meschede. *Optik, Licht und Laser*. Vieweg + Teubner, 2008.

[106] L. E. Estes et al. 'Scattering of Light from a Rotating Ground Glass'. In: *J. Opt. Soc. Am.* 61.10 (1971), p. 1301. DOI: 10.1364/JOSA.61.001301.

[107] G. A. Steudle et al. 'Measuring the quantum nature of light with a single source and a single detector'. In: *Phys. Rev. A* 86.5 (Nov. 2012), p. 053814. DOI: 10.1103/PhysRevA.86.053814.

[108] B. P. Abbott et al. 'Observation of Gravitational Waves from a Binary Black Hole Merger'. In: *Phys. Rev. Lett.* 116.6 (Feb. 2016), p. 061102. DOI: 10.1103/PhysRevLett.116.061102. arXiv: 1602.03837.

[109] A. Beveratos et al. 'Nonclassical radiation from diamond nanocrystals'. In: *Phys. Rev. A* 64.6 (Nov. 2001), p. 061802. DOI: 10.1103/PhysRevA.64.061802. arXiv: 0104028 [quant-ph].

[110] S. Fischbach et al. 'Efficient single-photon source based on a deterministically fabricated single quantum dot - Microstructure with backside gold mirror'. In: *Appl. Phys. Lett.* 111.1 (2017). DOI: 10.1063/1.4991389.

[111] P. Michler. *Single quantum dots*. Springer Berlin Heidelberg, 2003.

[112] S. Buckley et al. 'Engineered quantum dot single-photon sources.' In: *Rep. Prog. Phys.* 75.12 (Dec. 2012), p. 126503. DOI: 10.1088/0034-4885/75/12/126503.

[113] C. Hopfmann et al. 'Compensation of phonon-induced renormalization of vacuum Rabi splitting in large quantum dots: Towards temperature-stable strong coupling in the solid state with quantum dot-micropillars'. In: *Phys. Rev. B* 92.24 (Dec. 2015), p. 245403. DOI: 10.1103/PhysRevB.92.245403.

[114] K. A. Serrels et al. 'Solid immersion lens applications for nanophotonic devices'. In: *J. Nanophotonics* 2.1 (2008), pp. 21829–21854. DOI: 10.1117/1.3068652.

[115] A. Schlehahn et al. 'Single-photon emission at a rate of 14MHz from a deterministic quantum-dot microlens triggered by a mode-locked vertical-external-cavity surface-emitting laser'. In: *Appl. Phys. Lett.* 107.4 (2015). DOI: 10.1063/1.4927429.

[116] M. Strauß et al. 'Resonance fluorescence of a site-controlled quantum dot realized by the buried-stressor growth technique'. In: *Appl. Phys. Lett.* 110.11 (Mar. 2017), p. 111101. DOI: 10.1063/1.4978428.

[117] C. Schneider et al. 'Lithographic alignment to site-controlled quantum dots for device integration'. In: *Appl. Phys. Lett.* 92.18 (May 2008), p. 183101. DOI: 10.1063/1.2920189.

[118] C. Schneider et al. 'Single photon emission from a site-controlled quantum dot-micropillar cavity system'. In: *Appl. Phys. Lett.* 94.11 (Mar. 2009), p. 111111. DOI: 10.1063/1.3097016.

[119] T. J. Pfau et al. 'Site-controlled InAs quantum dots grown on a 55 nm thick GaAs buffer layer'. In: *Appl. Phys. Lett.* 95.24 (Dec. 2009), p. 243106. DOI: 10.1063/1.3265918.

[120] K. D. Jöns et al. 'Triggered indistinguishable single photons with narrow line widths from site-controlled quantum dots'. In: *Nano Lett.* 13.1 (2013), pp. 126–130. DOI: 10.1021/nl303668z.

[121] A. Surrente et al. 'Dense arrays of ordered pyramidal quantum dots with narrow linewidth photoluminescence spectra'. In: *Nanotechnology* 20.41 (Oct. 2009), p. 415205. DOI: 10.1088/0957-4484/20/41/415205.

[122] T. H. Chung et al. 'Selective carrier injection into patterned arrays of pyramidal quantum dots for entangled photon light-emitting diodes'. In: *Nat. Photonics* 10.12 (2016), pp. 782–787. DOI: 10.1038/nphoton.2016.203.

[123] S. Unsleber et al. 'Observation of resonance fluorescence and the Mollow triplet from a coherently driven site-controlled quantum dot'. In: *Optica* 2.12 (2015), p. 1072. DOI: 10.1364/OPTICA.2.001072.

[124] S. Hertenberger et al. 'High compositional homogeneity in In-rich InGaAs nanowire arrays on nanoimprinted SiO 2 /Si (111)'. In: *Appl. Phys. Lett.* 101.4 (July 2012), p. 043116. DOI: 10.1063/1.4738769.

[125] J. Claudon et al. 'A highly efficient single-photon source based on a quantum dot in a photonic nanowire'. In: *Nat. Photonics* 4.March (Jan. 2010), pp. 174–177. DOI: 10.1038/nphoton.2009.287.

[126] M. E. Reimer et al. 'Bright single-photon sources in bottom-up tailored nanowires'. In: *Nat. Commun.* 3 (Mar. 2012), p. 737. DOI: 10.1038/ncomms1746. arXiv: arXiv:1203.5676v1.

[127] A. Strittmatter et al. 'Lateral positioning of InGaAs quantum dots using a buried stressor'. In: *Appl. Phys. Lett.* 100.9 (Feb. 2012), p. 093111. DOI: 10.1063/1.3691251.

[128] A. Strittmatter et al. 'Site-controlled quantum dot growth on buried oxide stressor layers'. In: *Phys. status solidi* 209.12 (Dec. 2012), pp. 2411–2420. DOI: 10.1002/pssa.201228407.

[129] W. Unrau et al. 'Electrically driven single photon source based on a site-controlled quantum dot with self-aligned current injection'. In: *Appl. Phys. Lett.* 101.21 (Nov. 2012), p. 211119. DOI: 10.1063/1.4767525.

[130] A. Kaganskiy et al. 'Enhancing the photon-extraction efficiency of site-controlled quantum dots by deterministically fabricated microlenses'. In: *Opt. Commun.* 413.December 2017 (Apr. 2018), pp. 162–166. DOI: 10.1016/j.optcom.2017.12.032. arXiv: 1708.03512.

[131] A. Berthelot et al. 'Unconventional motional narrowing in the optical spectrum of a semiconductor quantum dot'. In: *Nat. Phys.* 2.11 (2006), pp. 759–764. DOI: 10.1038/nphys433. arXiv: 0610346 [cond-mat].

[132] A. Huggenberger et al. 'Narrow spectral linewidth from single site-controlled In(Ga)As quantum dots with high uniformity'. In: *Appl. Phys. Lett.* 98.13 (2011), pp. 2009–2012. DOI: 10.1063/1.3568890.

[133] A. Thoma et al. 'Exploring Dephasing of a Solid-State Quantum Emitter via Time- and Temperature-Dependent Hong-Ou-Mandel Experiments'. In: *Phys. Rev. Lett.* 116.3 (Jan. 2016), p. 033601. DOI: 10.1103/PhysRevLett.116.033601. arXiv: 1507.05900.

[134] H. Wang et al. 'Near-Transform-Limited Single Photons from an Efficient Solid-State Quantum Emitter'. In: *Phys. Rev. Lett.* 116.21 (May 2016), p. 213601. DOI: 10.1103/PhysRevLett.116.213601. arXiv: 1602.07386.

[135] L. Yang et al. 'Optical spectroscopy of site-controlled quantum dots in a Schottky diode'. In: *Appl. Phys. Lett.* 108.23 (2016), pp. 1–6. DOI: 10.1063/1.4952767.

[136] A. V. Kuhlmann et al. 'Transform-limited single photons from a single quantum dot'. In: *Nat. Commun.* 6.23 (Sept. 2015), p. 8204. DOI: 10.1038/ncomms9204.

[137] M. O. Scully et al. *Quantum optics*. Cambridge University Press, 1997.

[138] S. M. Ulrich et al. 'Dephasing of triplet-sideband optical emission of a resonantly driven InAs/GaAs quantum dot inside a microcavity'. In: *Phys. Rev. Lett.* 106.24 (June 2011), p. 247402. DOI: 10.1103/PhysRevLett.106.247402. arXiv: 1103.1594.

[139] A. Nazir et al. 'Modelling exciton–phonon interactions in optically driven quantum dots'. In: *J. Phys. Condens. Matter* 28.10 (Mar. 2016), p. 103002. DOI: 10.1088/0953-8984/28/10/103002. arXiv: 1511.01405.

[140] T. Takagahara. 'Theory of exciton dephasing in semiconductor quantum dots'. In: *Phys. Rev. B* 60.4 (July 1999), pp. 2638–2652. DOI: 10.1103/PhysRevB.60.2638.

[141] D. E. Reiter et al. 'The role of phonons for exciton and biexciton generation in an optically driven quantum dot'. In: *J. Phys. Condens. Matter* 26.42 (Oct. 2014), p. 423203. DOI: 10.1088/0953-8984/26/42/423203. arXiv: 1409.2265.

[142] T. Kaldewey et al. 'Demonstrating the decoupling regime of the electron-phonon interaction in a quantum dot using chirped optical excitation'. In: *Phys. Rev. B* 95.24 (June 2017), p. 241306. DOI: 10.1103/PhysRevB.95.241306. arXiv: 1701.01304.

[143] P. Grünwald. 'What $g^{(2)}(0) < 1/2$ tells you - and what it does not'. In: 2 (Nov. 2017), pp. 1–6. arXiv: 1711.05897.

[144] M. Gschrey et al. 'Highly indistinguishable photons from deterministic quantum-dot microlenses utilizing three-dimensional in situ electron-beam lithography'. In: *Nat. Commun.* 6.May (July 2015), p. 7662. DOI: 10.1038/ncomms8662.

[145] Y.-M. He et al. 'On-demand semiconductor single-photon source with near-unity indistinguishability'. In: *Nat. Nanotechnol.* 8.3 (Feb. 2013), pp. 213–217. DOI: 10.1038/nnano.2012.262.

[146] S. Reitzenstein et al. 'Quantum dot micropillars'. In: *J. Phys. D. Appl. Phys.* 43.3 (Jan. 2010), p. 033001. DOI: 10.1088/0022-3727/43/3/033001.

[147] C. Böckler et al. 'Electrically driven high- Q quantum dot-micropillar cavities'. In: *Appl. Phys. Lett.* 92.9 (2008), pp. 2006–2009. DOI: 10.1063/1.2890166.

[148] A. Musiał et al. 'Correlations between axial and lateral emission of coupled quantum dot–micropillar cavities'. In: *Phys. Rev. B* 91.20 (May 2015), p. 205310. DOI: 10.1103/PhysRevB.91.205310.

[149] M. P. Bakker et al. 'Quantum dot nonlinearity through cavity-enhanced feedback with a charge memory'. In: *Phys. Rev. B* 91.24 (June 2015), p. 241305. DOI: 10.1103/PhysRevB.91.241305. arXiv: 1503.08142.

[150] B. Merkel et al. 'Charge-driven feedback loop in the resonance fluorescence of a single quantum dot'. In: *Phys. Rev. B* 95.11 (Mar. 2017), p. 115305. DOI: 10.1103/PhysRevB.95.115305. arXiv: 1606.03215.

[151] C. Kistner et al. 'Resonantly probing micropillar cavity modes by photocurrent spectroscopy'. In: *Appl. Phys. Lett.* 94.22 (2009), p. 221103. DOI: 10.1063/1.3147162.

[152] S. Ates et al. 'Non-resonant dot–cavity coupling and its potential for resonant single-quantum-dot spectroscopy'. In: *Nat. Photonics* 3.12 (Dec. 2009), pp. 724–728. DOI: 10.1038/nphoton.2009.215.

[153] F. Jahnke. *Quantum optics with semiconductor nanostructures*. Woodhead Publishing, 2012.

[154] F. Hargart et al. 'Probing different regimes of strong field light–matter interaction with semiconductor quantum dots and few cavity photons'. In: *New J. Phys.* 18.12 (Dec. 2016), p. 123031. DOI: 10.1088/1367-2630/aa5198.

[155] M. Strauß et al. 'Wigner time delay induced by a single quantum dot'. In: *arXiv* 1 (2018), pp. 1–4. arXiv: 1805.06357.

[156] M. Strauß et al. 'Photon-statistics excitation spectroscopy of a single two-level system'. In: *Phys. Rev. B* 93.24 (June 2016), p. 241306. DOI: 10.1103/PhysRevB.93.241306. arXiv: 1601.05234.

[157] W. Heitler. *The Quantum Theory of Radiation*. Third. Oxford University Press, 1954. DOI: 10.1038/138483a0. arXiv: arXiv:1406.4422v2.

[158] M. Metcalfe et al. 'Heterodyne measurement of resonant elastic scattering from epitaxial quantum dots'. In: *Appl. Phys. Lett.* 102.23 (June 2013), p. 231114. DOI: 10.1063/1.4809594.

[159] C. Matthiesen et al. 'Subnatural Linewidth Single Photons from a Quantum Dot'. In: *Phys. Rev. Lett.* 108.9 (Feb. 2012), p. 093602. DOI: 10.1103/PhysRevLett.108.093602. arXiv: 1109.3412.

[160] R. Proux et al. 'Measuring the Photon Coalescence Time Window in the Continuous-Wave Regime for Resonantly Driven Semiconductor Quantum Dots'. In: *Phys. Rev. Lett.* 114.6 (Feb. 2015), p. 067401. DOI: 10.1103/PhysRevLett.114.067401.

[161] A. J. Bennett et al. 'Cavity-enhanced coherent light scattering from a quantum dot'. In: *Sci. Adv.* 2.4 (Apr. 2016), e1501256–e1501256. DOI: 10.1126/sciadv.1501256. arXiv: 1508.01637.

[162] C. Matthiesen et al. 'Phase-locked indistinguishable photons with synthesized waveforms from a solid-state source'. In: *Nat. Commun.* 4 (Mar. 2013), p. 1600. DOI: 10.1038/ncomms2601. arXiv: 1208.1689.

[163] R. Bourgain et al. 'Direct measurement of the Wigner time delay for the scattering of light by a single atom'. In: *Opt. Lett.* 38.11 (June 2013), p. 1963. DOI: 10.1364/OL.38.001963. arXiv: 1210.0389.

[164] S. Maier et al. 'Bright single photon source based on self-aligned quantum dot-cavity systems.' In: *Opt. Express* 22.7 (2014), pp. 8136–42. DOI: 10.1364/OE.22.008136.

[165] C. Cohen-Tannoudji et al. *Advances in Atomic Physics*. Singapore: World Scientific Publishing, 2011.

[166] P. Avan et al. 'Two-level atom saturated by a fluctuating resonant laser beam. Calculation of the fluorescence spectrum'. In: *J. Phys. B At. Mol. Phys.* 10.2 (Feb. 1977), pp. 155–170. DOI: 10.1088/0022-3700/10/2/006.

[167] P. Knight et al. 'Quantum revivals of a two-level system driven by chaotic radiation'. In: *Phys. Lett. A* 90.7 (July 1982), pp. 342–346. DOI: 10.1016/0375-9601(82)90625-9.

[168] A. T. Georges et al. 'Saturation and Stark Splitting of Resonant Transitions in Strong Chaotic Fields of Arbitrary Bandwidth'. In: *Phys. Rev. Lett.* 42.24 (June 1979), pp. 1609–1613. DOI: 10.1103/PhysRevLett.42.1609.

[169] M. Schubert et al. 'Influence of chaotic pump radiation with finite bandwidth on the intensity correlation of resonance fluorescence radiation'. In: *Opt. Commun.* 30.3 (Sept. 1979), pp. 275–278. DOI: 10.1016/0030-4018(79)90352-3.

[170] M. Brune et al. 'Quantum Rabi nutation in vacuum and coherent fields: a direct test of field quantization in a cavity'. In: *Summ. Pap. Present. Quantum Electron. Laser Sci. Conf.* (1996), pp. 2–5. DOI: 10.1109/QELS.1996.865696.

[171] G. Rempe et al. 'Observation of quantum collapse and revival in a one-atom maser'. In: *Phys. Rev. Lett.* 58.4 (1987), pp. 353–356. DOI: 10.1103/PhysRevLett.58.353.

[172] N. Sim et al. 'Measurement of photon statistics with live photoreceptor cells'. In: *Phys. Rev. Lett.* 109.11 (2012), pp. 1–5. DOI: 10.1103/PhysRevLett.109.113601. arXiv: 1201.2792.

[173] A. Carmele et al. 'Photon statistics as a probe for exciton correlations in coupled nanostructures'. In: *Phys. Rev. B* 79.3 (Jan. 2009), p. 035316. DOI: 10.1103/PhysRevB.79.035316.

[174] R. Loudon. *The Quantum Theory of Light*. Second. Oxford University Press, 1983.

[175] A. E. Lita et al. 'Counting near-infrared single-photons with 95% efficiency'. In: *Opt. Express* 16.5 (2008), p. 3032. DOI: 10.1364/OE.16.003032.

[176] C. Santori et al. 'Submicrosecond correlations in photoluminescence from InAs quantum dots'. In: *Phys. Rev. B* 69.20 (May 2004), p. 205324. DOI: 10.1103/PhysRevB.69.205324. arXiv: 0308323 [cond-mat].

[177] M. Davanço et al. 'Multiple time scale blinking in InAs quantum dot single-photon sources'. In: *Phys. Rev. B* 89.16 (Apr. 2014), p. 161303. DOI: 10.1103/PhysRevB.89.161303. arXiv: 1306.0614.

[178] F. Boitier et al. 'Measuring photon bunching at ultrashort timescale by two-photon absorption in semiconductors'. In: *Nat. Phys.* 5.4 (Apr. 2009), pp. 267–270. DOI: 10.1038/nphys1218.

[179] A. Jechow et al. 'Enhanced two-photon excited fluorescence from imaging agents using true thermal light'. In: *Nat. Photonics* 7.12 (2013), pp. 973–976. DOI: 10.1038/nphoton.2013.271.

[180] H. J. Carmichael. 'Quantum trajectory theory for cascaded open systems'. In: *Phys. Rev. Lett.* 70.15 (Apr. 1993), pp. 2273–2276. DOI: 10.1103/PhysRevLett.70.2273.

[181] C. W. Gardiner. 'Driving a quantum system with the output field from another driven quantum system'. In: *Phys. Rev. Lett.* 70.15 (Apr. 1993), pp. 2269–2272. DOI: 10.1103/PhysRevLett.70.2269.

[182] J. C. López Carreño et al. 'Exciting Polaritons with Quantum Light'. In: *Phys. Rev. Lett.* 115.19 (Nov. 2015), p. 196402. DOI: 10.1103/PhysRevLett.115.196402. arXiv: arXiv:1505.07823v1.

[183] J. C. López Carreño et al. 'Excitation with quantum light. I. Exciting a harmonic oscillator'. In: *Phys. Rev. A* 94.6 (2016), pp. 1–14. DOI: 10.1103/PhysRevA.94.063825. arXiv: 1601.06187.

[184] S. C. Azizabadi et al. 'Quantum cascade driving: Dissipatively mediated coherences'. In: *Phys. Rev. A* 96.2 (Aug. 2017), p. 023816. DOI: 10.1103/PhysRevA.96.023816. arXiv: 1706.05273.

[185] A. Delteil et al. 'Realization of a Cascaded Quantum System: Heralded Absorption of a Single Photon Qubit by a Single-Electron Charged Quantum Dot'. In: *Phys. Rev. Lett.* 118.17 (Apr. 2017), p. 177401. DOI: 10.1103/PhysRevLett.118.177401. arXiv: 1701.06957.

[186] M. Peiris et al. 'Two-color photon correlations of the light scattered by a quantum dot'. In: *Phys. Rev. B* 91.19 (2015), pp. 1–5. DOI: 10.1103/PhysRevB.91.195125.

[187] K. A. Fischer et al. 'Signatures of two-photon pulses from a quantum two-level system'. In: *Nat. Phys.* February (Feb. 2017). DOI: 10.1038/nphys4052.

[188] M. Peiris et al. 'Franson Interference Generated by a Two-Level System'. In: *Phys. Rev. Lett.* 118.3 (Jan. 2017), p. 030501. DOI: 10.1103/PhysRevLett.118.030501.

[189] E. Moreau et al. 'Quantum Cascade of Photons in Semiconductor Quantum Dots'. In: *Phys. Rev. Lett.* 87.18 (2001), p. 183601. DOI: 10.1103/PhysRevLett.87.183601.

[190] N. Akopian et al. 'Entangled Photon Pairs from Semiconductor Quantum Dots'. In: *Phys. Rev. Lett.* 96.13 (Apr. 2006), p. 130501. DOI: 10.1103/PhysRevLett.96.130501. arXiv: 0512048v2 [arXiv:quant-ph].

[191] H. Jayakumar et al. 'Time-bin entangled photons from a quantum dot'. In: *Nat. Commun.* 5.May (June 2014). DOI: 10.1038/ncomms5251.

[192] M. Prilmüller et al. 'Hyper-entanglement of photons emitted by a quantum dot'. In: *Arxiv* (Jan. 2017), pp. 1–5. DOI: 10.1364/CLEO_QELS.2017.FW1F.3. arXiv: 1701.08986.

[193] C. Sánchez Muñoz et al. 'Enhanced two-photon emission from a dressed biexciton'. In: *New J. Phys.* 17.12 (Dec. 2015), p. 123021. DOI: 10.1088/1367-2630/17/12/123021. arXiv: 1506.05050.

[194] P.-L. Ardelt et al. 'Optical control of nonlinearly dressed states in an individual quantum dot'. In: *Phys. Rev. B* 93.16 (Apr. 2016), p. 165305. DOI: 10.1103/PhysRevB.93.165305.

[195] F. Hargart et al. 'Cavity-enhanced simultaneous dressing of quantum dot exciton and biexciton states'. In: *Phys. Rev. B* 93.11 (Mar. 2016), p. 115308. DOI: 10.1103/PhysRevB.93.115308. arXiv: 1509.03861.

[196] S. Bounouar et al. 'Path-Controlled Time Reordering of Paired Photons in a Dressed Three-Level Cascade'. In: *Phys. Rev. Lett.* 118.23 (June 2017), p. 233601. DOI: 10.1103/PhysRevLett.118.233601. arXiv: 1610.08268.

[197] A. Carmele et al. 'Correlations of cascaded photons: An analytical study in the two-photon Mollow regime'. In: (Oct. 2017), pp. 1–23. arXiv: 1710.03031.

[198] M. Gschrey et al. 'In situ electron-beam lithography of deterministic single-quantum-dot mesa-structures using low-temperature cathodoluminescence spectroscopy'. In: *Appl. Phys. Lett.* 102.25 (2013). DOI: 10.1063/1.4812343.

[199] G. Sek et al. 'On the applicability of a few level rate equation model to the determination of exciton versus biexciton kinetics in quasi-zero-dimensional structures'. In: *J. Appl. Phys.* 108.3 (Aug. 2010), p. 033507. DOI: 10.1063/1.3467002.

[200] A. Kiraz et al. 'Photon correlation spectroscopy of a single quantum dot'. In: *Phys. Rev. B* 65.16 (Mar. 2002), p. 161303. DOI: 10.1103/PhysRevB.65.161303. arXiv: 0108450 [cond-mat].

[201] H. Jayakumar et al. 'Deterministic Photon Pairs and Coherent Optical Control of a Single Quantum Dot'. In: *Phys. Rev. Lett.* 110.13 (Mar. 2013), p. 135505. DOI: 10.1103/PhysRevLett.110.135505.

[202] S. Bounouar et al. 'Phonon-assisted robust and deterministic two-photon biexciton preparation in a quantum dot'. In: *Phys. Rev. B* 91.16 (Apr. 2015), p. 161302. DOI: 10.1103/PhysRevB.91.161302.

[203] T. R. Gentile et al. 'Experimental study of one- and two-photon Rabi oscillations'. In: *Phys. Rev. A* 40.9 (Nov. 1989), pp. 5103–5115. DOI: 10.1103/PhysRevA.40.5103.

[204] A. Aspect et al. 'Time Correlations between the Two Sidebands of the Resonance Fluorescence Triplet'. In: *Phys. Rev. Lett.* 45.8 (Aug. 1980), pp. 617–620. DOI: 10.1103/PhysRevLett.45.617.

[205] C. A. Schrama et al. 'Intensity correlations between the components of the resonance fluorescence triplet'. In: *Phys. Rev. A* 45.11 (June 1992), pp. 8045–8055. DOI: 10.1103/PhysRevA.45.8045.

[206] A. Ulhaq et al. 'Cascaded single-photon emission from the Mollow triplet sidebands of a quantum dot'. In: *Nat. Photonics* 6.4 (Feb. 2012), pp. 238–242. DOI: 10.1038/nphoton.2012.23.

[207] C. A. Schrama et al. 'Destructive interference between opposite time orders of photon emission'. In: *Phys. Rev. Lett.* 67.18 (Oct. 1991), pp. 2443–2445. DOI: 10.1103/PhysRevLett.67.2443.

[208] J. D. Franson. 'Bell inequality for position and time'. In: *Phys. Rev. Lett.* 62.19 (May 1989), pp. 2205–2208. DOI: 10.1103/PhysRevLett.62.2205.

[209] E. del Valle et al. 'Theory of Frequency-Filtered and Time-Resolved <math display="inline"> <mi>N</mi> </math> -Photon Correlations'. In: *Phys. Rev. Lett.* 109.18 (Oct. 2012), p. 183601. DOI: 10.1103/PhysRevLett.109.183601.

[210] A. Gonzalez-Tudela et al. 'Two-photon spectra of quantum emitters'. In: *New J. Phys.* 15.3 (Mar. 2013), p. 033036. DOI: 10.1088/1367-2630/15/3/033036. arXiv: arXiv:1211.5592v1.

[211] J. E. Avron et al. 'Entanglement on Demand through Time Reordering'. In: *Phys. Rev. Lett.* 100.12 (Mar. 2008), p. 120501. DOI: 10.1103/PhysRevLett.100.120501. arXiv: 0710.2308.

[212] J. Johansson et al. 'QuTiP: An open-source Python framework for the dynamics of open quantum systems'. In: *Comput. Phys. Commun.* 183.8 (Aug. 2012), pp. 1760–1772. DOI: 10.1016/j.cpc.2012.02.021. arXiv: 1110.0573.

[213] J. Johansson et al. 'QuTiP 2: A Python framework for the dynamics of open quantum systems'. In: *Comput. Phys. Commun.* 184.4 (Apr. 2013), pp. 1234–1240. DOI: 10.1016/j.cpc.2012.11.019. arXiv: 1211.6518.

Appendix

1 Numerical simulations of the correlation functions in the dressed cascade

In this appendix we present some theoretical results which were used to study the effects discussed in chapter 6. In particular, we made some assertions in the main text concerning the photon-photon correlation without further evidence. The simulations of the correlation functions presented here as well as the spectra in the main text were numerically calculated using the Quantum Toolbox in Python [212, 213].

The correlation function of the bare states can be calculated using

$$g^{(2)}(\tau) = \frac{\langle \hat{\sigma}^{\dagger}{}_{HB}(0)\hat{\sigma}^{\dagger}_{GH}(\tau)\hat{\sigma}_{GH}(\tau)\hat{\sigma}_{HB}(0)\rangle}{\langle \hat{\sigma}_{HH}\rangle} \qquad (\tau > 0). \tag{1}$$

A simulation of equation 1 is plotted in Fig. 1 for two different excitation strengths. It is also displayed in the main text and shown here again for completeness. In principle, these correlations are also accessible in the experiment by correlating all L lines with all R lines.

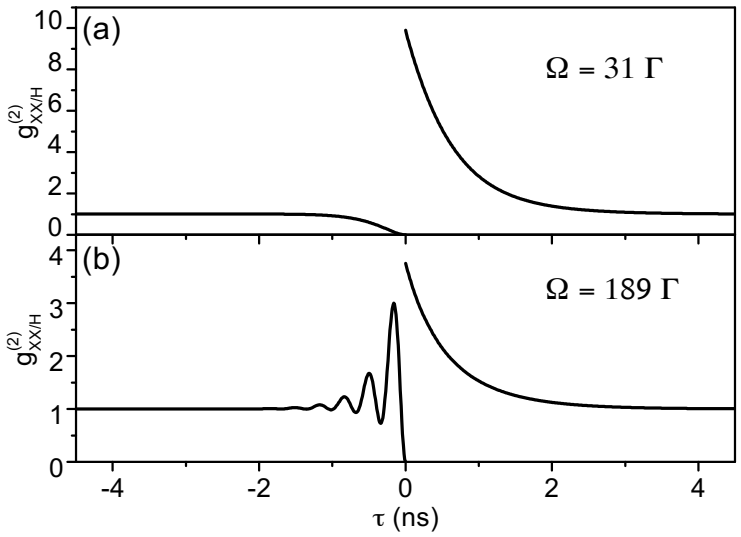

Figure 1: Correlation function of the bare states XX-H. (a) For a driving strength of $\Omega = 63\Gamma$ we observe a bunching for positive and a antibunching for negative time delays. (b) Under strong excitation, $\Omega = 169\Gamma$, the bunching for positive time delays persists while for negative time delays Rabi oscillations become visible.

As mentioned in the main text, we only observe the transitions involving the $|+\rangle$ and $|0\rangle$ state. Hence to simulate the experimental correlation function more accurately we compute the correlation functions in the dressed state basis. We plot the correlation functions for the eight possible detection sequences in Fig. 2 for low excitation power and Fig. 3 for high excitation powers. As expected, the positive time delays always exhibit a bunching. For negative time delays, the correlation involving different dressed

states also always exhibit an antibunching. The correlation functions involving the same dressed states always display a bunching behaviour for negative time delays. The notable difference is however that for weak excitation this bunching has a value of 2 while for strong excitation it tends towards 4. It is thus the power dependence of this bunching that leads to the different correlation for negative time delays in the subfigure (a) of Fig. 2 and Fig. 3.

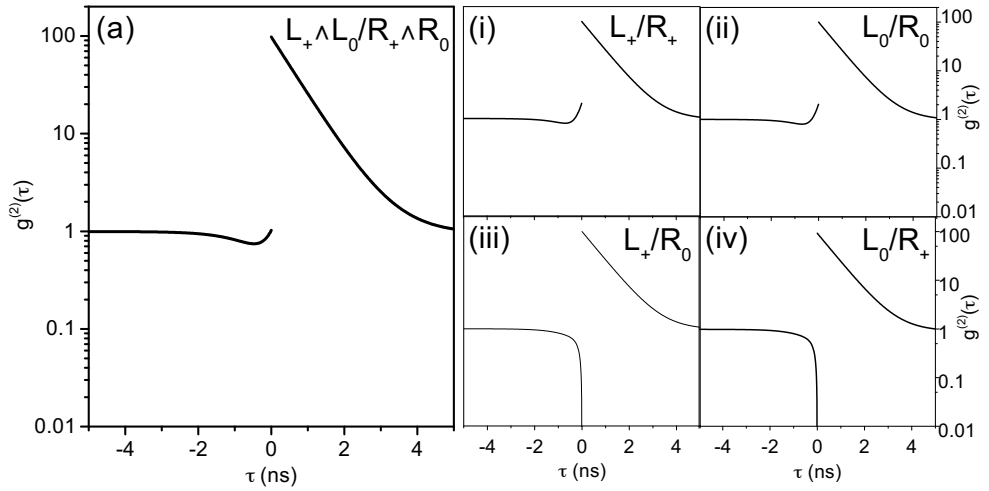

Figure 2: Correlation functions of the dressed states $L_+ \wedge L_0/R_+ \wedge R_0$ under weak excitation. Note the logarithmic scaling of the y axis. (a) For a driving strength of $\Omega = 34\Gamma$ we observe a bunching for positive time delays and a slight antibunching for negative time delays for $\Gamma < \tau < 0$. (i)-(iv) Photon-photon correlations between single transitions that make up the correlation in (a)

For convenience we also express the bare states in the basis of the dressed states. They are given by:

$$|V\rangle = a_- \frac{2E_-}{\Omega} |-\rangle + a_+ \frac{2E_+}{\Omega} |+\rangle \tag{2}$$

$$|B\rangle = \frac{1}{\sqrt{2}} |0\rangle + a_+ |+\rangle + a_- |-\rangle \tag{3}$$

$$|G\rangle = -\frac{1}{\sqrt{2}} |0\rangle + a_+ |+\rangle + a_- |-\rangle \tag{4}$$

$$|H\rangle = |H\rangle\,. \tag{5}$$

The normalisation coefficients are given by

$$a_0 = \frac{1}{\sqrt{2}} \tag{6}$$

$$a_+ = \frac{\Omega}{\sqrt{2\Omega^2 + 4E_+^2}} \tag{7}$$

$$a_- = \frac{\Omega}{\sqrt{2\Omega^2 + 4E_-^2}} \tag{8}$$

where $E_{+/-}$ are the eigenvalues given by equation 2.56d and 2.56c.

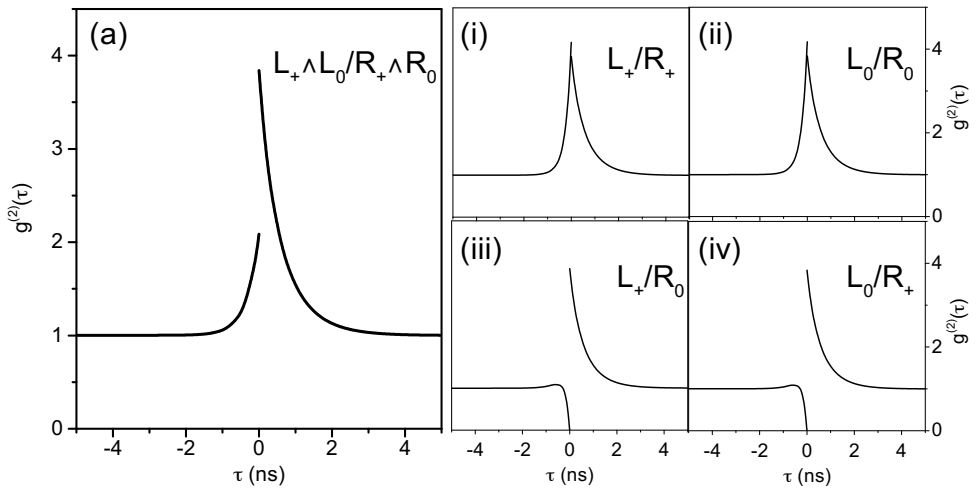

Figure 3: Correlation functions of the dressed states $L_+ \wedge L_0/R_+ \wedge R_0$ under strong excitation. (a) For a driving strength of $\Omega = 170\Gamma$ we observe a bunching for both detection sequences. (i)-(iv) Photon-photon correlations between single transitions that make up the correlation in (a)

2 Sample structures

NP6303				
section	number	thickness (nm)	material	doping
capping layer	1 x	30	GaAs	intrinsic
anti-diffusion barrier	1 x	20	AlGaAs	
spacer layer	1 x	80	GaAs	
active layer	1 x		In(Ga)As	
buffer layer	1 x	50	GaAs	
capping layer	1 x	80	GaAs	
cladding	1 x	40	AlGaAs	
oxidised layer	1 x	30	AlAs	
cladding	1 x	40	AlGaAs	
lower DBR	23 x	62	GaAs	
		78	$Al_{0.91}Ga_{0.09}As$	
buffer layer	1 x	300	GaAs	

Table 1: Sample structure of the SCQD sample NP6303 used for the experiments presented in chapter 4.

M2833

section	number	thickness (nm)	material	doping concentration (cm^{-3})
upper DBR	2 x	61	C:GaAs	2×10^{19}
		69	C:AlAs	
	9 x	61	C:GaAs	3×10^{18}
		69	C:AlAs	
	5 x	61	C:GaAs	2×10^{18}
		69	C:AlAs	
	7 x	61	C:GaAs	1×10^{18}
		69	C:AlAs	
cavity	1 x	134	GaAs	intrinsic
active layer	1 x	1.4	$In_{0.6}Ga_{0.4}As$	
cavity	1 x	134	GaAs	
lower DBR	1 x	69	AlAs	
	4 x	61	Si:GaAs	1×10^{18}
		69	Si:AlAs	
	5 x	61	Si:GaAs	2×10^{18}
		69	Si:AlAs	
	17 x	61	Si:GaAs	3×10^{18}
		69	Si:AlAs	
buffer layer	1 x	400	Si:GaAs	3×10^{18}

Table 2: Sample structure of electrically contacted micropillar sample M2833-16.10 used for the experiments on photocurrent spectroscopy presented in chapter 4. An additional δ-doping is present at every interface between GaAs and AlAs with an area doping corresponding to 1×10^{12} cm^{-2}.

M3569

section	number	thickness (nm)	material	doping
upper DBR	5 x	69	GaAs	intrinsic
		75	$Al_{0.9}Ga_{0.1}As$	
cavity	1 x	147	GaAs	
active layer	1 x	1.5 (cap)	InAs PCA	
cavity	10 x	10	GaAs	
	1 x		Si	δ-doped
	1 x	137	GaAs	intrinsic
lower DBR	1 x	75	$Al_{0.9}Ga_{0.1}As$	
	17 x	69	GaAs	
		75	$Al_{0.9}Ga_{0.1}As$	
buffer layer	1 x	400	$Al_{0.9}Ga_{0.1}As$	

Table 3: Sample structure of the planar QD sample M3569 used for the experiments presented in chapter 5.

NP 5647				
section	number	thickness (nm)	material	doping
capping layer	1 x	400	GaAs	intrinsic
active layer	1 x		$In_{0.63}Ga_{0.37}As$	
spacer layer	1 x	72	GaAs	
lower DBR	23 x	66	GaAs	
		78	$Al_{0.91}Ga_{0.09}As$	
buffer layer	1 x	305	GaAs	
substrate	1 x	5000	$Al_{0.9}$GaAs:Si	n

Table 4: Sample structure of microlense sample NP5647-2 CLL002 used for the experiments on the biexciton presented in chapter 6.

Danksagung/Acknowledgements

At this point I would like to thank a number of people who contributed to this work and supported me throughout the years. In particular I would like to thank:

- Prof. Dr. Stephan Reitzenstein for his support and never tiring enthusiasm throughout the years. He allowed me stray far from my original research project and was very supportive of my research. Especially, he accepted my proposal to build my own setup which made my life a lot easier.
- Prof. Dr. Mete Atatüre who accepted to be part of the committee.
- Prof. Dr. Kathy Lüdge for agreeing to chair the committee.
- Dr. Janik Wolters for his ingenuity and teaching me a lot over the years.
- Dr. Samir Bounouar for the fruitful collaboration on the two-photon project and many interesting discussions on physics and *Gott und die Welt*.
- Dr. Alexander Carmele for sharing some of his insights with me and his genuine fascination with physics.
- Dr. Tobias Heindel and Dr. Anna Musial for helping me at various stages of my work and always being open to questions.
- Elisabeth Schlottmann, Alexander Thoma, Peter Schnauber, Tobias Heindel and the raucous gang from EW 251 for joint lunches. I also concede loss to Ferdinand and Anna Katharina in our edition of "Das perfekte Mittagessen". You are clearly the more accomplished cooks.
- Arsenty Kaganskiy for the interesting project on the SCQDs and in particular for the growth and fabrication of the sample.
- Marlon Placke, Robert Voigt and Marcel Hohn for their work and and joint time in the lab during their respective thesis.
- My office roomies over the years Marlon, Steffen, Felix and Kaisa.
- The proof readers of this work: Prof. Dr. Stephan Reitzenstein, Dr. Kaisa Laiho, Dr. Samir Bounouar, Marlon Placke.
- Finally, I would like to thank all other past and present members of the AG Reitzenstein for the always enjoyable atmosphere in the group. In particular, I will keep several good and unforgettable memories of our group seminars in Wernigerode and Bad Lindow.

Erklärung/Declaration

Gemäß §5 Abs. 1 Ziff. 1, 5 und 7 sowie §2 Abs. 4 der Promotionsordnung der Technischen Universität Berlin

Hiermit erkläre ich, dass mir die geltende Promotionsordnung der TU Berlin in der Fassung vom 05.02.2014 bekannt ist.

Peer-reviewed publications

The following publications containing parts of my thesis have already appeared:

'Wigner time delay induced by a single quantum dot',
M. Strauß, M. Hohn, C. Schneider, M. Kamp, S. Höfling, J. Wolters, S. Reitzenstein, arXiv:1805.06357

Personal contribution: experimental measurements, data analysis, simulation, writing of manuscript

'Correlations of cascaded photons: An analytical study in the two-photon Mollow regime',
A. Carmele, S. Bounouar, M. Strauß, S. Reitzenstein, A. Knorr, arXiv:1710.03031

Personal contribution: experimental measurements

'Path-controlled time reordering of paired photons in a dressed three level system',
S. Bounouar*, M. Strauß*, A. Carmele, P. Schnauber, A. Thoma, M. Gschrey, J.-H. Schulze, A. Strittmatter, S. Rodt, A.Knorr, S. Reitzenstein, *Phys. Rev. Lett.* 118, 233601 (2017)
* equal contribution
Personal contribution: experimental measurements, data analysis, writing of manuscript

'Resonance fluorescence of a site-controlled quantum dot realized by the buried-stressor growth technique',
M. Strauß, A. Karganskiy, R. Voigt, P. Schnauber, J.-H. Schulze, S. Rodt, A. Strittmatter S. Reitzenstein, *Appl. Phys. Lett.* 110, 111101 (2017)

Personal contribution: experimental measurements, data analysis, writing of manuscript

'Photon-statistics excitation spectroscopy of a single two-level system',
M. Strauß, M. Placke, S. Kreinberg, C. Schneider, M. Kamp, S. Höfling, J. Wolters, S. Reitzenstein, *Phys. Rev. B* 93, 241306(R) (2016)

Personal contribution: experimental measurements, theoretical modelling, data analysis, writing of manuscript

Conference contributions

'Wigner time delay induced by a single quantum dot'
Talk, DPG spring meeting 2017, Dresden

'Time-reordering of paired photons in a dressed three level system'
Talk, DPG spring meeting 2017, Mainz

'Exciting a quantum dot resonantly with thermal light'
Poster, NOEKS13 2016, Dortmund

'Photon-statistics excitation spectroscopy of a single two-level system'
Poster, QD2016 2016, Jejudo, Korea

'Photon-statistics excitation spectroscopy of a single two-level system'
Talk, DPG spring meeting 2016, Regensburg

'Influence of acoustic phonons on strong coupling phenomena in quantum dot-micropillars'
Poster, SUSSP71: 'Frontiers in Quantum Dynamics & Quantum Optics' 2015, Glasgow

'Influence of acoustic phonons on strong coupling phenomena in quantum dot-micropillars'
Talk, DPG spring meeting 2015, Berlin

'Influence of acoustic phonons on strong coupling phenomena in quantum dot-micropillars'
Poster, NOEKS12 2014, Bremen

Publications not related to this work:

'Generation of maximally entangled states and coherent control in quantum dot microlenses',
S. Bounouar, C. de la Haye, M. Strauß, P. Schnauber, A. Thoma, M. Gschrey, J.-H. Schulze, A. Strittmatter, S. Rodt, S. Reitzenstein (2017), *Appl. Phys. Lett.* 112, 153107 (2018)

Personal contribution: minor parts of experimental measurements

'Quantum-optical spectroscopy of a two-level system using an electrically driven micropillar laser as a resonant excitation source',
S. Kreinberg, T. Grbesic, M. Strauß, A. Carmele, M. Kamp, C. Schneider, S. Höfling, X. Porte, S. Reitzenstein (2017), Light Sci. Appl. 7, 41 (2018)

Personal contribution: building the resonance fluorescence setup

'Accessing the dark exciton in deterministic quantum-dot microlenses',
T. Heindel, A. Thoma, I. Schwartz, E. R. Schmidgall, L. Gantz, D. Cogan, M. Strauß, P. Schnauber, M. Gschrey, J.-H. Schulze, A. Strittmatter, S. Rodt, D. Gershoni, S. Reitzenstein (2017), *APL Photonics* 2, 121303 (2017)

Personal contribution: minor parts of experimental measurements

'Compensation of phonon-induced renormalization of vacuum Rabi splitting in large quantum dots: Towards temperature-stable strong coupling in the solid state with quantum dot-micropillars',
C. Hopfmann, A. Musial, M. Strauß, A.M. Barth, M. Glässl, A. Vagov, M. Strauß, C. Schneider, S. Höfling, M. Kamp, V.M. Axt, S. Reitzenstein, *Phys. Rev. B* 92,245403 (2015)

Personal contribution: parts of experimental measurements

'Quantum Zeno phenomenon on a single solid-state spin'
J. Wolters, M. Strauß, R. S. Schoenfeld, and O. Benson, *Phys. Rev. A* 88, 020101 (2013)

Personal contribution: parts of experimental measurements

Versicherung an Eides statt

Gemäß §5 Abs. 2 Ziff. 2 der Promotionsordnung der Technischen Universität Berlin

Hiermit erkläre ich an Eides statt, dass ich die Dissertation selbständig und nur unter Verwendung der angegebenen Literatur und Hilfsmittel angefertigt babe.

Die Angaben zu meinem Eigenanteil an den Veröffentlichungen in meiner Erklärung sind zutreffend.

Zudem versichere ich, dass ich bei keiner anderen Hochschule oder Fakultät eine Promotionsabsicht eingereicht oder ein Promotionsverfahren beantragt habe.

Berlin, den 12. September 2018

Stefan Maximilian Strauß